LONG-RANGE SURFACE POLARITONS IN THIN LAYERS OF ABSORBING MATERIALS

Yichen Zhang

Cover image: a surface wave induced by a water drop. This wave is propagating at the interface between water and air.

ISBN: 978-90-77209-52-3

A catalogue record is available from the Technical University of Eindhoven Library.
A digital version of this thesis can be downloaded from http://www.amolf.nl

Long-range surface polaritons in thin layers of absorbing materials

PROEFSCHRIFT

ter verkrijging van de graad van doctor aan de
Technische Universiteit Eindhoven, op gezag van
de rector magnificus, prof.dr.ir. C.J. van Duijn,
voor een commissie aangewezen door het
College voor Promoties in het openbaar te
verdedigen op maandag 12 september 2011 om
14.00 uur

door

Yichen Zhang

geboren te Beijing, China

Dit proefschrift is goedgekeurd door de promotor:

prof.dr. J. Gómez Rivas

This work is part of the research program of the "Stichting voor Fundamenteel Onderzoek der Materie (FOM)", which is financially supported by the "Nederlandse organisatie voor Wetenschappelijk Onderzoek (NWO)" and is part of an industrial partnership program between Philips and FOM.

To my parents

Contents

1 Introduction 11

1.1 Long-range surface polaritons (LRSPs) 14

1.2 Outline of the thesis 16

2 Electromagnetic surface modes in absorbing thin layers 17

2.1 Surface polaritons at a single interface 18

2.2 Surface polaritons on multilayers slab structures 22

2.2.1 Electromagnetic guided modes in thin slabs 22

2.2.2 LRSPs in silver and amorphous silicon thin films 32

2.3 Optical excitation method: attenuated total reflection 35

3 LRSPs supported by thin films of amorphous and crystalline chalcogenide glass 39

3.1 Introduction 40

3.2 Experimental 40

3.3 Mode calculation 45

3.4 Conclusion 48

4 LRSPs supported by silicon at visible and ultraviolet frequencies 49

4.1 Introduction 50

4.2 Experimental 50

4.2.1 Sample fabrication 50

4.2.2 ATR configuration and reflectance measurement 51

4.2.3 Near-field calculation 56

4.3 Discussion 57

4.4 Conclusion 60

5 Controlling the dispersion of guided modes in thin layers of amorphous silicon 61

5.1 Introduction 62

5.2 Experimental 62
5.3 Surface modes characteristics 65
5.4 Discussion 69
5.5 Conclusion 72

6 LRSPs sensors based on nanometric layers of strongly absorbing materials 73
6.1 Introduction 74
6.2 Experimental 75
6.3 Mode calculation 80
6.4 Conclusion 87

7 Coupled LRSPs in a multilayer of amorphous silicon 89
7.1 Introduction 90
7.2 Experimental 91
7.2.1 Setup 91
7.2.2 Measurements 91
7.3 Calculations and discussion 92
7.4 Conclusions 94

References 95

Summary 105

Samenvatting 109

Notation 113

Acknowledgments 115

Curriculum Vitae 117

List of Publications 119

CHAPTER 1

INTRODUCTION

When Albert Einstein won the Nobel prize in 1921 for his explanation of the photoelectric effect, he said "was das Licht sei, das weiβ ich nicht", which means "what the light might be, I do not know" [1, 2]. A tremendous amount of progress has been made during the last 90 years in our understanding of light. However, there is still much to discover.

In this thesis we investigate the light-matter interaction at a nano-scale. This investigation constitutes a part of the field of *nanophotonics*, which describes the interaction of light with objects of similar and smaller size than the wavelength of light at visible frequencies. Nanophotonics has flourished in the past few years, thanks to the advent of nano-fabrication techniques that allows us to structure matter with a precision that was only dream not so long ago. In particular, we investigate the interaction of light with ultra-thin layers of strongly absorbing materials, i.e., layers with a thickness of only a few nanometers of semiconductors and chalcogenide glass. In spite of the small thickness of the layers investigated in this thesis, light-matter interaction is considered macroscopically. Under this assumption, the thin layers are considered as homogeneous media, which are characterized by an electrical permittivity and a magnetic permeability, i.e., two intrinsic material properties that describe the response of charges and currents to an applied electromagnetic field. We demonstrate in this thesis that, although optical absorption is very strong in the materials forming the thin layers, these layers can support surface waves. These surface waves are guided over many wavelengths while being tightly bounded to the surface. Contrary to what can be naively expected, absorption improves the propagation of the surface wave. These surprising results have helped us to generalize the concept of guided modes in thin layers of arbitrary materials.

An interface separating two non-absorbing dielectrics cannot support surface waves propagating along the interface and decaying from that interface into the surrounding media. The concept of surface waves was first proposed by Zenneck [3] and extended by Sommerfeld [4] at the beginning of the last century. The term of "Zenneck wave" describes an electromagnetic wave that is guided at an interface separating a dielectric from a conductor. The important feature of this mode is that it is concentrated near the interface decaying evanescently from this interface in the surrounding media. Zenneck considered the existence of these waves on a conductor with an essentially imaginary permittivity, i.e., a strongly absorbing conducting medium. With the description of these modes, Zenneck was seeking for an explanation to the long propagation distances of radio waves along the earth surface. Zenneck was wrong with the explanation in terms of surface waves as the propagation distance of radio waves is caused by their reflection in the ionosphere. However, his work can be considered as seminal in the field of electromagnetism. In 1941, Fano investigated surface electromagnetic waves propagating at the interface between a non-absorbing dielectric and a lossless metal characterized by a real permittivity [5]. These modes extend into the more general concept of surface plasmon polaritons at the interface between a dielectric and a noble metal with a complex permittivity and low losses [6–9].

When an electromagnetic wave travels through a polarizable medium, it is modified by the polarization that it induces, i.e., the wave is coupled to the medium. This coupled mode is called a polariton. Surface polaritons are specific cases in which the fields are bounded to the surface separating a dielectric from a different medium. Surface plasmon polaritons are electromagnetic waves coupled to coherent oscillation of the free charges at the interface between a metal and a dielectric. The electric field of the electromagnetic wave induces the oscillation of the free charges, which in turn radiate electromagnetic radiation. In the case of bounded charges it is possible to excite surface phonon polaritons [10–13].

Without losing generality, surface modes can be described by considering the dispersive behavior of their wave number. Restricting the problem to two dimensions, as it is represented in Fig. 1.1(a), the components of the wave vector (k_x, k_y) are given by

$$k_x^2 + k_y^2 = \frac{\omega^2}{c^2} \, , \tag{1.1}$$

where ω is the angular frequency and c the speed of light in the dielectric. A characteristic of surface waves is that they are evanescent in the y-direction, i.e., in the direction normal to the surface. The evanescent character is described by a purely imaginary value of the y-component of the wave number. This imaginary value is obtained when $k_x > \omega/c$. Since ω/c corresponds to the wave number of free propagating (unbounded) radiation, we can state that the wave number of surface polaritons along the propagation direction is larger than that wave number of unbounded radiation. Figure 1.1(a) displays the field (magnetic component along the z-direction) of a surface polariton at single interface. This field component has its maximum at the interface and decays exponentially away from the interface. Modes with $k_x \leq \omega/c$ at an interface are known as leaky modes as the energy radiate into the surrounding dielectric.

In previous studies of surface polaritons on noble metals, it has been demonstrated the possibility of confining electromagnetic fields at a nanoscale and the tunability of the dispersion relation of these modes with structured surfaces [14–18]. The development of nanoscale fabrication techniques has stimulated applications based on plasmonic structures [19–25].

In this thesis, we focus on surface polaritons supported by strongly absorbing materials. As we will see in the next section and in chapter 2, these modes arise from the coupling of leaky modes on the opposite sides of the thin film. As a result of this coupling, an evanescent mode is formed. This mode, known as long-range surface polariton, can propagate along the thin film while decaying evanescently away from the film. Long-range surface polaritons may provide new opportunities for the development of devices compatible with well developed silicon technology. These devices can lead to an improvement of the performance of integrated optical system component [26–30], optical sensors [31–34], or an optimization of the optical absorption in thin film solar cells [35, 36] and the emission properties of

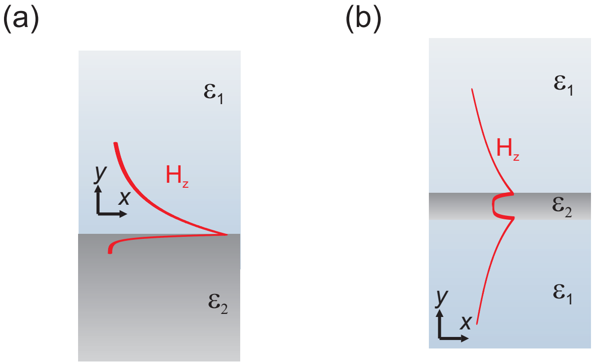

Figure 1.1: (a) H_z field of surface polaritons on a single interface, (b) H_z field of long-range surface polaritons in a thin film.

emitters [37–40].

1.1 Long-range surface polaritons (LRSPs)

When a thin film of a metal with a permittivity $\epsilon_2 = \epsilon_{2r} + i\epsilon_{2i}$, where $\epsilon_{2r} < -1$ and $|\epsilon_{2r}| \gg \epsilon_{2i}$, is embedded between two similar dielectrics with permittivity $\epsilon_1 \geq 1$, the surface plasmon polaritons excited on both interfaces of the film can couple. This coupling is schematically represented in Fig. 1.1(b), where the magnetic field amplitude along the z-direction is plotted. The electromagnetic field is largely excluded from the thin layer, as a consequence of the coupling, extending more into the surrounding non-absorbing dielectric. These surface waves are known as long-range surface plasmon polaritons (LRSPPs) due to the long propagation length that they exhibit as a consequence of the reduction of field amplitude in the absorbing layer. LRSPPs have been intensively investigated in thin films of gold and silver [6, 14, 41–43], and several applications have been proposed; e.g., the lower losses of these modes lead to sharper resonances in attenuated total reflection measurements, which can improve the figure of merit of surface plasmon resonance sensors [31, 43–45]. Due to the long propagation length of long-range surface plasmon polaritons, these modes have been proposed for on-chip optical data communication [26, 28, 46, 47]. However, their large decay length into the surrounding medium limits the integration of optical circuits [48–50]. Extending the range of materials used to support long-range surface waves could lead to a broaden spectrum of applications, such as novel sensors and waveguides [51, 52].

Figure 1.2 shows the dispersion curve of a guided mode in a thin layer of a strongly absorbing material with a permittivity $\epsilon_2 = 1 + 20i$ (red solid line) in vacuum, i.e., the dependence of the frequency with the real component of the wave number parallel to the layer. For the calculation we have considered $d = 20\,\mathrm{nm}$, where d is the thickness of the layer. The dashed line of Fig. 1.2 corresponds to $\mathbf{k}_0 = \omega/c$, i.e., the dispersion relation of light in vacuum or the edge of the light cone in the dielectric surrounding the thin layer. The wave numbers of the guided mode along the propagation direction are larger than those of the light cone for each frequency. In other words, $k_x > \omega/c$, which is the necessary condition for evanescent surface modes. As it is described in detail in chapter 2, guided modes supported by thin layers of strongly absorbing dielectrics have very similar characteristics in terms of propagation length and field distribution to long-range surface plasmon polaritons. Therefore, they have been named as long-range surface exciton polaritons or long-range surface polariton (LRSPs) [53–56]. In spite of these similarities, there are only a few works about LRSPs, most probably because of the uncommon conditions for their existence, i.e., $|\epsilon_{2r}| \lesssim \epsilon_{2i}$ and $\epsilon_{2i} \gg 1$, being ϵ_r and ϵ_i the real and imaginary components of the permittivity of the thin film. Kovacs demonstrated that LRSPs can be excited onto an iron thin film by the attenuated total reflection method [57]. Yang *et al.* [58] showed that a thin film of vanadium can support surface waves at infrared wavelengths in which this material behaves as an strongly absorbing dielectric. In subsequent works, the same group demonstrated the excitation of these modes in other materials such as palladium, organic films and islandised metallic films [56, 59–61]. Takabayashi *et al.* [62] measured the propagation of guided modes in thin slabs of silicon at 633 nm. However, at this wavelength the absorption of Si is weak and the modes investigated by Takabayashi and co-workers were at the transition between TM_0 modes and LRSPs. The excitation of surface polaritons in Au nanoparticles has been also demonstrated in the extreme UV by means of electron energy-loss spectroscopy [63]. At these frequencies Au behaves as a strongly absorbing dielectric. More recently, we have demonstrated the excitation of LRSPs on thin films of amorphous silicon at UV-frequencies and in thin films of chalcogenide glass in the visible range [30, 64].

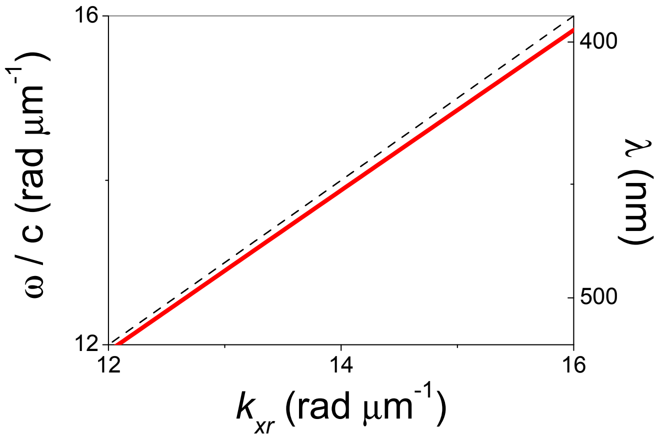

Figure 1.2: Dispersion curve, i.e., frequency versus the real component of the wave number along the propagation direction of a long-range surface polariton in a thin film ($d = 20\,\text{nm}$) of a material with permittivity $\epsilon_2 = 1 + 20i$ surrounded by vacuum. The dashed line indicates the edge of the light cone.

1.2 Outline of the thesis

This thesis focuses on the fundamental understanding of the optical properties of long-range surface polaritons (LRSPs) supported by thin layers of strongly absorbing materials. The outline of the thesis is as follows:

We provide a theoretical formulation of guided modes in different kinds of slab waveguides in *Chapter 2*. The influence of the permittivity of the thin layers on the LRSPs are described in *Chapter 3*, where measurements of the coupling of incident radiation to a thin film of a phase change chalcogenide glass are presented. We demonstrate that this coupling is almost independent of the value of the real component of the permittivity as long as the imaginary component has a larger value. LRSPs supported by thin layers of amorphous silicon are investigated in *Chapter 4*, a figure of merit (FOM) of surface modes in slab waveguide is given for comparison reason. In *Chapter 5*, we present a systematic experimental study of dispersion of long-range guided modes in Si layers. We show that the dispersion can be tuned by changing the thickness of the layer, a mode evolution between TM_0 and LRSPs has been verified. We propose a refractive index sensor based on LRSPs in amorphous chalcogenide glass in *Chapter 6*. A general comparison of the intrinsic sensitivity (IS) for guided modes on different materials is presented in this chapter. Coupled LRSPs on multilayers are investigated in *Chapter 7*, where we demonstrate the excitation of these surface modes in two closely spaced layers of amorphous Si.

CHAPTER 2

ELECTROMAGNETIC SURFACE MODES IN ABSORBING THIN LAYERS

We give a theoretical description of guided modes in slab waveguides. A comparison between conventional waveguide modes and long-range guided modes in thin layers of materials with an arbitrary permittivity is provided. The focus of this thesis is on the guided modes supported by strongly absorbing materials.

2.1 Surface polaritons at a single interface

Let's consider an interface between two semi-infinite, isotropic and homogeneous media that are characterised by a frequency dependent and complex dielectric permittivity $\epsilon(\omega) = \epsilon_r(\omega) + i\epsilon_i(\omega)$, where the subscripts r and i refer to the real and imaginary components of the permittivity respectively. For simplicity we will not express the ω dependence in the following. When an electromagnetic wave travels through a polarizable medium, it is modified by the polarization that it induces. This interaction gives rise to polaritons that couple electromagnetic waves to the polarizable medium. Surface polaritons is a specific case of this interaction, which yields to electromagnetic fields bounded to a surface and decaying exponentially in the normal direction.

Figure 2.1 shows a TM-electromagnetic wave, i.e., **E**-field in the plane of incidence, incident at the interface between two semi-infinite media. The medium at the left side is a dielectric with permittivity ϵ_1 and the medium at the right side is a material with permittivty ϵ_2. The incident wave impinges onto the interface separating both media with a wave vector $\mathbf{k} = (k_x, k_y, 0)$, and it is partly reflected and partly transmitted. We would like to explore the field associated to surface

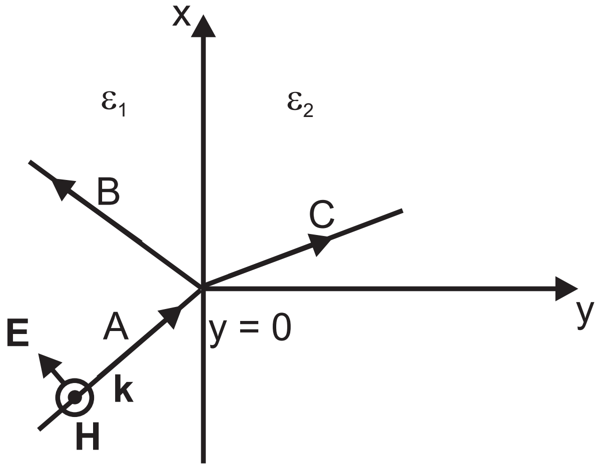

Figure 2.1: A schematic diagram of the incident, transmitted and reflected fields associated with a TM polarized electromagnetic wave incident on an interface bounded by two media characterized by complex dielectric permittivities ϵ_1 and ϵ_2.

polaritons. The field associated to a TM-polarized wave can be written as

$$\mathbf{E} = [\mathrm{E_x}, \mathrm{E_y}, 0] e^{i(k_x x + k_y y)}, \tag{2.1}$$

$$\mathbf{H} = [0, 0, \mathrm{H_z}] e^{i(k_x x + k_y y)}, \tag{2.2}$$

where for simplicity we do not express the temporal dependence. We can define the electric field components with Ampère-Maxwell law

$$\mathrm{E_x}(y) = \frac{k_y}{\omega \varepsilon_0 \varepsilon} \mathrm{H_z}(y), \tag{2.3}$$

$$\mathrm{E_y}(y) = \frac{-k_x}{\omega \varepsilon_0 \varepsilon} \mathrm{H_z}(y). \tag{2.4}$$

For the case of a wave in medium 1 propagating on the interface, the magnetic and electric fields are

$$\mathrm{H_{z1}} = \mathrm{A} e^{-i(k_{x1} x + k_{y1} y)} + \mathrm{B} e^{i(k_{y1} y - k_{x1} x)}, \tag{2.5}$$

$$\mathrm{E_{x1}} = \frac{k_{y1}}{\omega \epsilon_0 \epsilon_1} [\mathrm{A} e^{-i(k_{x1} x + k_{y1} y)} - \mathrm{B} e^{i(k_{y1} y - k_{x1} x)}], \tag{2.6}$$

$$\mathrm{E_{y1}} = \frac{-k_{x1}}{\omega \epsilon_0 \epsilon_1} [\mathrm{A} e^{-i(k_{x1} x + k_{y1} y)} + \mathrm{B} e^{i(k_{y1} y - k_{x1} x)}], \tag{2.7}$$

where A and B are the amplitude of the incident and reflected fields respectively. The fields in medium 2 are given by

$$\mathrm{H_{z2}} = \mathrm{C} e^{-i(k_{x2} x + k_{y2} y)}, \tag{2.8}$$

$$\mathrm{E_{x2}} = \frac{k_{y2}}{\omega \epsilon_0 \epsilon_2} \mathrm{C} e^{-i(k_{x2} x + k_{y2} y)}, \tag{2.9}$$

$$\mathrm{E_{y2}} = \frac{-k_{x2}}{\omega \epsilon_0 \epsilon_2} \mathrm{C} e^{-i(k_{x2} x + k_{y2} y)}, \tag{2.10}$$

where C is the amplitude of the transmitted field. To determine the eigenmodes associated to the surface, we set A = 0 and B an exponentially decaying function in the y-direction. To satisfy the boundary conditions at y = 0, the tangential components of the field $\mathrm{H_z}$ and $\mathrm{E_x}$ need to be continuous across the interface, so that we have

$$\mathrm{B} = \mathrm{C}, \ -\frac{k_{y1}}{\epsilon_1} = \frac{k_{y2}}{\epsilon_2}. \tag{2.11}$$

Equation (2.11) represents the dispersion relation of surface polaritons and it can be satisfied only when ϵ_1 and ϵ_2 have an opposite sign, i.e., when one medium is a metal and the other a dielectric. This is the condition for the existence of surface plasmon polaritons between two semi-infinite media. The wavenumber of the surface wave is related to the surrounding media by

$$k_x^2 + k_{y1}^2 = \epsilon_1 \mathbf{k}_0^2, \tag{2.12}$$

$$k_x^2 + k_{y2}^2 = \epsilon_2 \mathbf{k}_0^2. \tag{2.13}$$

By introducing Eq. (2.12) and (2.13) into Eq. (2.11), the dispersion relation of the surface plasmon polaritons can be written as

$$k_x = \frac{\omega}{c_0}\left(\frac{\epsilon_1\epsilon_2}{\epsilon_1+\epsilon_2}\right)^{1/2}. \tag{2.14}$$

Assuming that medium 2 is characterized by a complex permittivity $\epsilon_2 = \epsilon_{2r} + i\epsilon_{2i}$, in which losses are low, $\epsilon_{2i} << |\epsilon_{2r}|$, while medium 1 is a lossless dielectric with a real and positive permittivity ϵ_1, the in plane wave vector k_x of the surface plasmon polariton can be approximated to

$$k_x = k_{xr} + ik_{xi} \simeq \frac{\omega}{c_0}\left(\frac{\epsilon_1\epsilon_{2r}}{\epsilon_1+\epsilon_{2r}}\right)^{1/2} + i\frac{\omega}{c_0}\left(\frac{\epsilon_1\epsilon_{2r}}{\epsilon_1+\epsilon_{2r}}\right)^{3/2}\left(\frac{\epsilon_{2i}}{2\epsilon_{2r}^2}\right). \tag{2.15}$$

The permittivity of silver is shown in Fig. 2.2(a) [65]. The metal has a negative real component of the permittivity in the visible and infrared wavelengths but at shorter wavelengths ϵ_{2r} becomes positive. This transition between a metallic and a dielectric behavior in silver takes place at the bulk plasma frequency. Figure 2.3(a) shows a calculation using Eq. (2.14) for surface plasmon polaritons at the interface between a silver and air. Surface waves are characterized by a dispersion curve outside the light cone, i.e., $k_{xr} > \mathbf{k}_0\sqrt{\epsilon_1}$. This bounded surface plasmon polariton is observed for wavelengths longer than 330 nm which corresponds to the condition of $\epsilon_{2r} < -1$. For wavelengths shorter than 330 nm, the dispersion is inside the light cone and thus the mode is not a bounded surface wave, i.e., it radiates into the surrounding dielectric.

If we consider an absorbing dielectric, i.e., amorphous silicon, in the visible with a permittivity shown in Fig. 2.2(b), The dispersion of the corresponding surface polaritons are inside the light cone (see Fig. 2.3(b)). Only at high frequencies (short wavelengths) the wave number of surface modes in a-Si is larger than that of free space radiation in air. Note that at these frequencies, a-Si has a metallic character, $\epsilon_{2r} < -1$, and these surface modes are surface plasmon polaritons (SPPs).

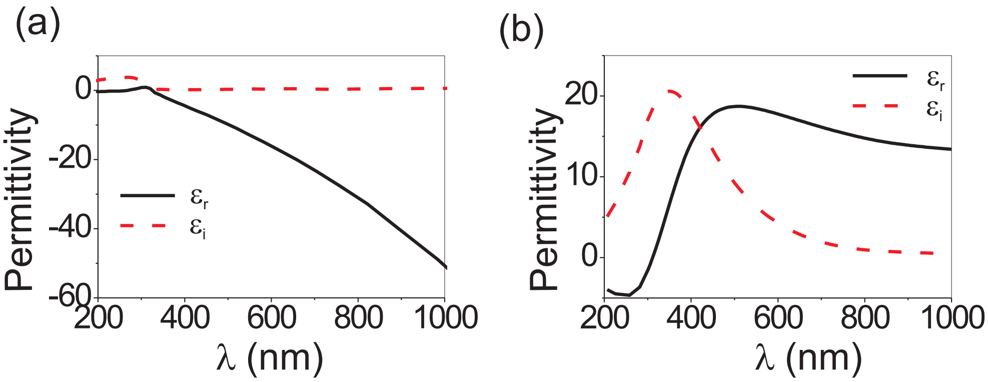

Figure 2.2: (a) The real and imaginary components of the permittivity of Ag are taken from Ref. [65]. (b) Real and imaginary components of the permittivitity of amorphous silicon obtained from ellipsometry measurements.

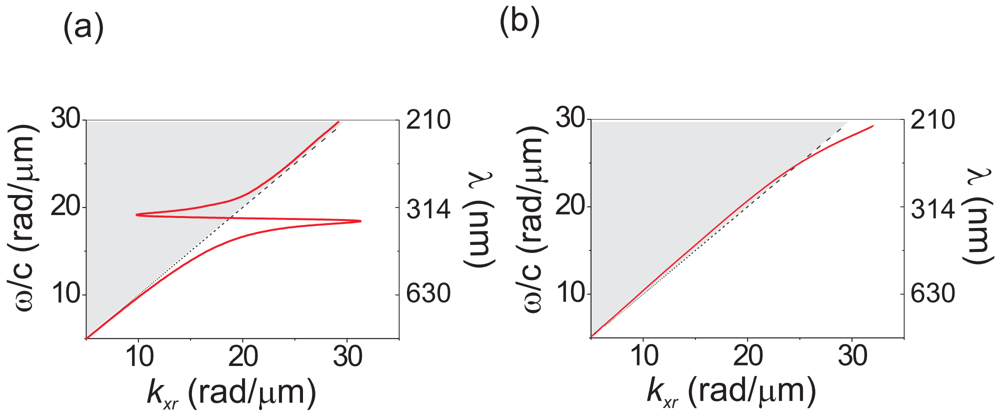

Figure 2.3: (a) Dispersion relation of surface polaritons at the interface between Ag and air. (b) Dispersion relation of surface polaritons at the interface between amorphous silicon and air.The gray area represents the light cone.

The losses of surface waves, due to the absorption in the material, strongly affect their propagation length. This propagation length is given by

$$\mathrm{L_x} = \frac{1}{2k_{xi}}. \tag{2.16}$$

The mode confinement to the surface, or the decay length of the SPPs into the surrounding dielectric is given by $\mathrm{L_y} = 1/2k_{yi}$ where k_{yi} is the imaginary component of the wave vector component in the y-direction. By using Eq. (2.12), we can write L_y as

$$L_y = \frac{1}{2Re\sqrt{k_x^2 - \mathbf{k}_0^2 n_1}}. \tag{2.17}$$

Figure 2.4(a) illustrates the propagation length of SPPs for the Ag/air geometry. The dramatic reduction of the propagation length occurs close to the wavelength corresponding to the plasma frequency of silver. At shorter wavelengths SPPs becomes radiative and the definition of L_x becomes meaningless due to the radiative losses. Figure 2.4(b) shows the decay length of the field intensity of SPPs in air for the Ag/air geometry.

2.2 Surface polaritons on multilayers slab structures

2.2.1 Electromagnetic guided modes in thin slabs

In the previous Section we have calculated the dispersion of surface waves propagating on a single interface separating two semi-infinite media. We consider here a slab of a medium with permittivity ϵ_2 and thickness d in the y-direction, surrounded by two lossless dielectrics characterized by the permittivities ϵ_1 and ϵ_3 (see Fig. 2.5). The electromagnetic field of a TM mode in medium 1, i.e., when

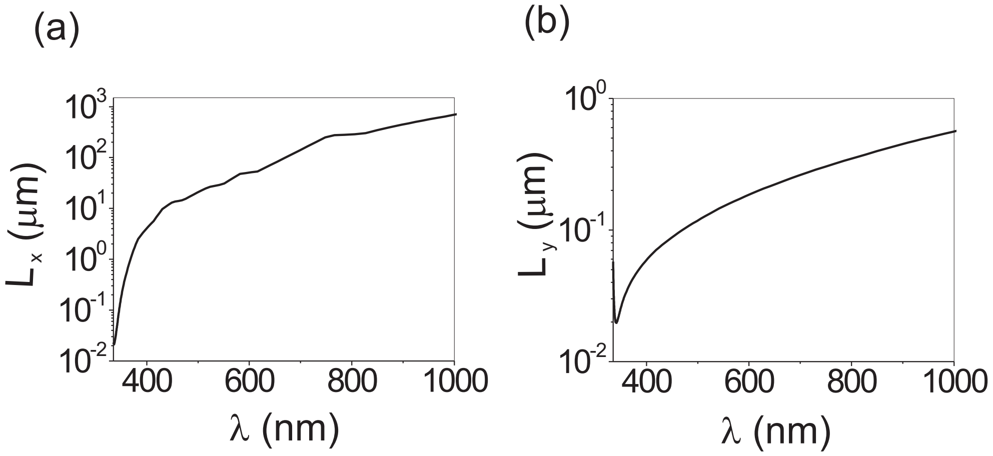

Figure 2.4: (a) Propagation length of surface plasmon polaritons at the interface between Ag with air. (b) Decay length of a surface plasmon polaritons at the interface between Ag and air.

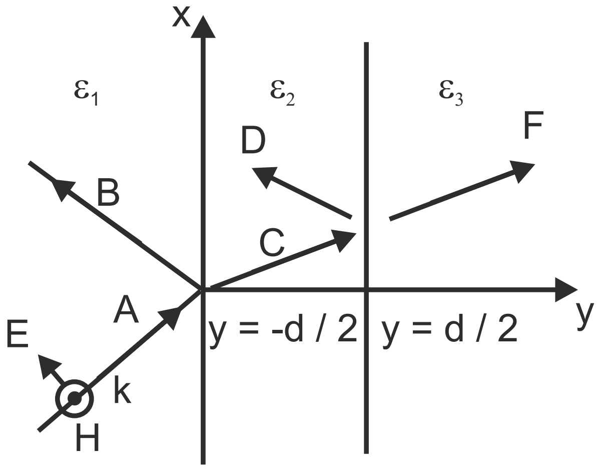

Figure 2.5: Schematic representation of s slab of material ϵ_2, surrounded by media ϵ_1 and ϵ_3.

$y < -d/2$, is given by

$$H_{z1} = Ae^{-i(k_{x1}x+k_{y1}y)} + Be^{i(k_{y1}y-k_{x1}x)}, \tag{2.18}$$

$$E_{x1} = \frac{k_{y1}}{\omega\epsilon_0\epsilon_1}[Ae^{-i(k_{x1}x+k_{y1}y)} - Be^{i(k_{y1}y-k_{x1}x)}], \tag{2.19}$$

$$E_{y1} = \frac{-k_{x1}}{\omega\epsilon_0\epsilon_1}[Ae^{-i(k_{x1}x+k_{y1}y)} - Be^{i(k_{y1}y-k_{x1}x)}], \tag{2.20}$$

while in the slab, i.e., when $-d/2 < y < d/2$, is given by

$$H_{z2} = Ce^{-i(k_{x2}x+k_{y2}y)} + De^{i(k_{y2}y-k_{x2}x)}, \tag{2.21}$$

$$E_{x2} = \frac{k_{y2}}{\omega\epsilon_0\epsilon_2}[Ce^{-i(k_{x2}x+k_{y2}y)} - De^{i(k_{y2}y-k_{x2}x)}], \tag{2.22}$$

$$E_{y2} = \frac{-k_{x2}}{\omega\epsilon_0\epsilon_2}[Ce^{-i(k_{x2}x+k_{y2}y)} - De^{i(k_{y2}y-k_{x2}x)}], \tag{2.23}$$

and in medium 3, i.e., when $y > d/2$, is given by

$$H_{z3} = Fe^{-i(k_{x3}x+k_{y3}y)}, \tag{2.24}$$

$$E_{x3} = \frac{k_{y3}}{\omega\epsilon_0\epsilon_3}Fe^{-i(k_{x3}x+k_{y3}y)}, \tag{2.25}$$

$$\mathrm{E_{y3}} = \frac{-k_{x3}}{\omega\epsilon_0\epsilon_3}\mathrm{F}e^{-i(k_{x3}x+k_{y3}y)}, \tag{2.26}$$

where A,B,C,D and F represent the incident, reflected and transmitted amplitudes at the two interfaces. To find the eigenmodes of the slab, we set the amplitude of the incident wave A to 0. The requirement of continuity of the tangential component for the fields at the interfaces leads to

$$\mathrm{B}e^{-ik_{y1}d/2} = \mathrm{C}e^{ik_{y2}d/2} + \mathrm{D}e^{-ik_{y2}d/2}, \tag{2.27}$$

$$-\frac{\mathrm{B}}{\epsilon_1}k_{y1}e^{-ik_{y1}d/2} = \frac{\mathrm{C}}{\epsilon_2}k_{y2}e^{ik_{y2}d/2} - \frac{\mathrm{D}}{\epsilon_2}k_{y2}e^{-ik_{y2}d/2}, \tag{2.28}$$

at $y = -d/2$, and

$$\mathrm{F}e^{-ik_{y3}d/2} = \mathrm{C}e^{-ik_{y2}d/2} + \mathrm{D}e^{ik_{y2}d/2}, \tag{2.29}$$

$$\frac{\mathrm{F}}{\epsilon_3}k_{y3}e^{-ik_{y3}d/2} = \frac{\mathrm{C}}{\epsilon_2}k_{y2}e^{-ik_{y2}d/2} - \frac{\mathrm{D}}{\epsilon_2}k_{y2}e^{ik_{y2}d/2}, \tag{2.30}$$

at $y = d/2$. The solution to Eqs. (2.27)-(2.30) leads to the dispersion relation of TM guided modes by the thin layer

$$e^{-2ik_{y2}d} = \left(\frac{\frac{k_{y2}}{\epsilon_2}+\frac{k_{y1}}{\epsilon_1}}{\frac{k_{y2}}{\epsilon_2}-\frac{k_{y1}}{\epsilon_1}}\right)\left(\frac{\frac{k_{y2}}{\epsilon_2}+\frac{k_{y3}}{\epsilon_3}}{\frac{k_{y2}}{\epsilon_2}-\frac{k_{y3}}{\epsilon_3}}\right). \tag{2.31}$$

If we assume that the thin layer is symmetrically surrounded by the same dielectric, i.e., $\epsilon_1 = \epsilon_3$ and $k_{y1} = k_{y3}$, Eq.(2.31) can be splitted into two equations

$$\tanh\left(ik_{y2}d/2\right) = -\frac{\epsilon_2 k_{y1}}{\epsilon_1 k_{y2}}, \tag{2.32}$$

and

$$\tanh\left(ik_{y2}d/2\right) = -\frac{\epsilon_1 k_{y2}}{\epsilon_2 k_{y1}}. \tag{2.33}$$

These two equations correspond to symmetric and antisymmetric TM modes in slab waveguides, where the symmetry refers to the $\mathrm{H_z}$ field component with respect to the middle plane of the slab.

Similarly, the dispersion relations of TE guided modes are given by [*]

$$\tanh\left(ik_{y2}d/2\right) = -\frac{k_{y1}}{k_{y2}}, \tag{2.34}$$

---

[*] a detailed derivation can be found in Ref. [66].

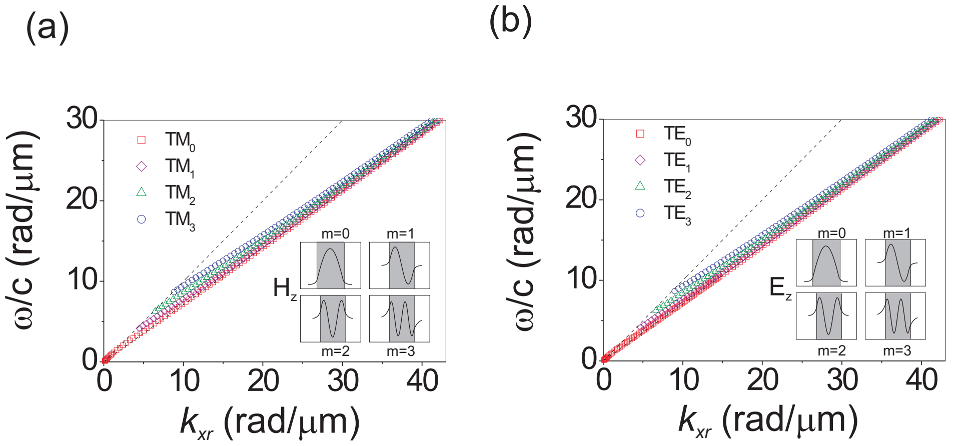

Figure 2.6: (a) Dispersion relations of TM waveguide modes. (b) Dispersion relation of TE waveguide modes. The represented multilayers structures are a 1.2μm slab $\epsilon_2 = 2 + 0.01i$ surrounded by air $\epsilon_{1,3} = 1$. The dashed lines represents the light line in air and slab. The insets in Fig. 2.6(a) are magnetic field distributions of $m = 0, 1, 2, 3$ modes for TM waveguides.

and

$$\tanh\left(ik_{y2}d/2\right) = -\frac{k_{y2}}{k_{y1}}\,. \tag{2.35}$$

Where Eq. (2.34) corresponds to modes with a symmetric E$_z$ field component with respect to middle plane of the layer and Eq. (2.35) refers to modes with an antisymmetric E$_z$ field component.

In the case of having a non- or weakly absorbing dielectric forming the thin layer, i.e., $\epsilon_{2r} \gg \epsilon_{2i} \simeq 0$ and by using the relation $\tanh(ix) = i\tan(x)$, we can retrieve from Eqs. (2.32)-(2.35) the equations defining the TM and TE modes most commonly used in literature [67–69]. Note that these equations have multiple solutions defining the TM$_m$ and TE$_m$ modes, where $m = 1, 2, 3....$ Calculated dispersion relations using a 1.2μm slab with a permittivity of $2 + 0.01i$ surrounded by air are presented in Fig. 2.6(a) for TM modes and in Fig. 2.6(b) for TE modes. The inset of Fig. 2.6(a) diplays the field distributions for the corresponding H$_z$ components of the odd ($m = 0, 2$) and even ($m = 1, 3$) guided modes. The TE modes have similar field distributions for the E$_z$ components as shown in Fig. 2.6(b) as insets. The number of guided modes supported by the slab is determined by the ratio between its dimension and the wavelength [70]. If the thickness of the slab is smaller than $\lambda/2$, only the two symmetric fundamental, TM$_0$ and TE$_0$, modes can be guided by the dielectric slab. These are the only two modes without a cutoff frequency [71]. Figure 2.7 shows the calculated dispersion relation of the guided modes supported by a 30 nm slab with a permittivity of $2+0.01i$ surrounded by air. We can conclude from Fig. 2.7 that the two fundamental modes do not have a cutoff frequency [72, 73].

If we consider the slab formed by a non- or weakly absorbing metal, i.e., $|\epsilon_{2r}| \gg \epsilon_{2i} \simeq 0$), and $|\epsilon_{2r}| > \epsilon_1$, only TM modes are guided by the slab. In this situation Eq. (2.32) describes the so-called long range surface plasmon polaritons (LRSPPs) and Eq.(2.33) defines the short range surface plasmon polaritons (SRSPPs) [20]. LRSPPs have a symmetric distribution ($m = 0$) of the normal component of the magnetic field $\mathrm{H_z}$ with respect to the middle plane of the slab, while short-range SRSPPs have an antisymmetric distribution ($m = 1$) of this normal magnetic field component [74–76]. These surface modes arise from the coupling between surface polaritons supported by the individual interfaces separating the thin layer and the surrounding dielectric. The different field symmetry between LRSPPs and SRSPPs can be understood as the result of two surface waves at both interfaces coupling either in phase or out of phase. The mode with the smallest fraction of the field inside the thin layer is the long-range mode, whereas the mode with the largest fraction of the field in the thin layer is the short-range mode due to a larger dissipation of energy [20, 74].

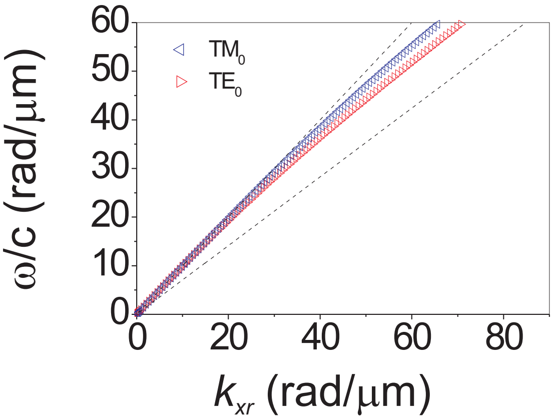

Figure 2.7: Dispersion relation of the two fundamental ($m = 0$) TM$_0$ and TE$_0$ waveguide modes. The represented multilayers structures are a 30 nm slab $\epsilon_2 = 2+0.01i$ surrounded by air $\epsilon_{1,3} = 1$. The dashed lines represents the light line in air and slab.

For strongly absorbing thin films in which $\epsilon_{2i} \gg |\epsilon_{2r}| \simeq 0$, followed by the anology of coupled surface polaritons, there are also long-range guided modes, which have been named long-range surface exciton polaritons after Ref. [55], although no excitonic resonances are necessary to excite this type of surface modes [43]. The dispersion of long-range surface exciton polaritons is given by Eq. (2.32). More generally, we can define long-range surface polaritons (LRSPs) as guided modes described by Eq. (2.32) in a thin layer ($d \ll \lambda$) with $|\epsilon_{2r}| \lesssim \epsilon_{2i}$ (independent of the sign of ϵ_{2r}) and $\epsilon_{2i} \gg 1$. As we show next, short-range surface polaritons (SRSPs) in thin absorbing layers, arising from Eq. (2.33), are leaky waves with a wavenumber smaller than the wave number of free space radiation in the surrounding dielectric.

We have calculated the real (k_{xr}) and imaginary (k_{xi}) components of the complex wave number of guided modes in thin slabs of materials with permittivities $\epsilon_2 = 20+1i$, $-20+1i$ and $1+20i$ surrounded by air and at λ =600 nm. We choose these values based on the classification of materials, i.e., weakly absorbing dielectrics $(20+1i)$, weakly absorbing metal $(-20+1i)$ and strongly absorbing materials $(1+20i)$. These values are displayed in Figs. 2.8 and 2.9 as a function of the thickness of the layer normalized by λ, i.e., as a function of d/λ. The values of k_{xr} and k_{xi} in these figures are normalized by the wave number in the surrounding dielectric $k_0 n_1$, where we set $n_1 = \sqrt{\varepsilon_1} = 1$ as the refractive index of air. For $\epsilon_2 = 20+1i$, these ratios correspond to the conventional TM_0 and TE_0 modes (solid curve and circles in Fig. 2.8(a), respectively). The LRSPPs and SRPPs in the slab with $\epsilon_2 = -20+1i$ are represented by the solid and dashed curves in Fig. 2.8(b). Figure 2.8(c) displays the calculation of LRSPs (solid curve), SRSPs (dashed curve) in an absorbing layer with $\epsilon_2 = 1+20i$. The dashed lines correspond to the light line in air. Although we have derived the guided modes by thin slabs of arbitrary permittivity with the same set of equations (Eqs. (2.32)-(2.35)), we note that there are important differences between a generic TM_0 or TE_0 guided mode in a dielectric slab and a LRSPP or LRSP in a metal or absorbing layer. A conventional TM_0 mode is a bulk mode resulting from the interaction of the fields at the two surfaces of the thin film by means of total internal reflection; while LRSPPs and LRSPs are guided modes due to the coupling between two surface modes at opposite interfaces penetrating the layer. This difference can be appreciated in Figs 2.8(a), (b) and (c), where the wavenumber of the TM_0 and TE_0 modes in non-absorbing dielectric layers converges for large thicknesses to the value of free space radiation in the layer, while this wavenumber converges to the value of surface polaritons on single interfaces for the case of metals and strongly absorbing materials. We also note that the wavenumber of SRSPPs (Fig. 2.8(b)) increases for small thickness, while the wavenumber of LRSPPs converges to the value for free space radiation in the surrounding dielectric. This behavior indicates that LRSPPs are less confined to the thin layer and extend more into the surrounding dielectric as the thickness decreases, while the opposite behavior happens for SRSPPs. For the case of LRSPs and SRSPs in the thin absorbing layer (Fig. 2.8(b)), we see that in the thick film limit the wavenumber converges to the value of surface polaritons in single interfaces. This value is below the light line of the surrounding dielectric because the real component of permittivity of the thin layer is positive (see previous section). SRSPs remain below the light line for any thickness indicating that this is not a surface mode as it leaks into the surrounding dielectric. On the other hand, LRSPs become surface modes for thicknesses below $d/\lambda = 0.14$, only in this specific case. We note that as the thickness is further reduced, the wavenumber of LRSPs converges to the light line as it was the case for LRSPPs.

In Fig. 2.9(a) the imaginary components of k_{xi}, i.e., the propagation losses of (LRSPs) and (LRSPPs) at the particular wavelength of λ =600 nm, are plotted. For LRSPs, k_{xi} is plotted only for values of d/λ at which this mode is evanescent, i.e., $k_{xr} > \mathbf{k}_0 n_1$. Note that k_{xi} vanishes for small values of d/λ. This reduction of the losses and the concomitant long propagation length of long-range surface modes is a consequence to the electromagnetic field symmetry with respect to the middle plane of the thin layer, as it is shown as inset in Fig. 2.9(a) and (b). Fig. 2.9(b) displays the imaginary components of the wave number of short-range surface plasmon polaritons (SRSPPs) in a thin film of a material with $\epsilon_2 = -20 + 1i$. In contrast with LRSPs, we have that SRSPs are leaky waves, i.e., $k_{xr} < \mathbf{k}_0 n_1$ for any value of d/λ. Therefore, no values of k_{xi} are given for LRSPs. For small values of d/λ the values of k_{xi} for SRSPPs increase, and so do the losses in the thin film. This is the reason of the short propagation of these modes. In this thesis, we focus on long-range surface modes on absorbing thin films, therefore we will not discuss further the properties of SRSPPs and SPSPs.

The ratio between the imaginary and real components of the wave vector (k_y) in the layer for (LRSPPs), (LRSPs) and TM$_0$ modes, i.e., k_{y2i}/k_{y2r} in thin films with $\epsilon_2 = -20 + 1i$, $\epsilon_2 = 1 + 20i$ and $\epsilon_2 = 20 + 1i$ surrounded by air are given in Fig. 2.10. This ratio determines whether the guided modes are evanescent surface waves guided at the interfaces of the slab or conventional waveguide modes guided due to total internal reflection at the inner surfaces of the slab. LRSPPs in metals are evanescent surface waves as the ratio of k_{y2i}/k_{y2r} is larger than 1 for both thin and thick metallic films. The conventional TM$_0$ mode are guided via waves radiated away from the surfaces since the ratio is smaller than 1. For the case of LRSPs, we see that $k_{y2i} > k_{y2r}$ only in the range of thicknesses at which the real component of the wavenumber is larger than that of free space radiation in the surrounding dielectric (see Fig. 2.8). The large value of k_{y2i} originates from the strong absorption

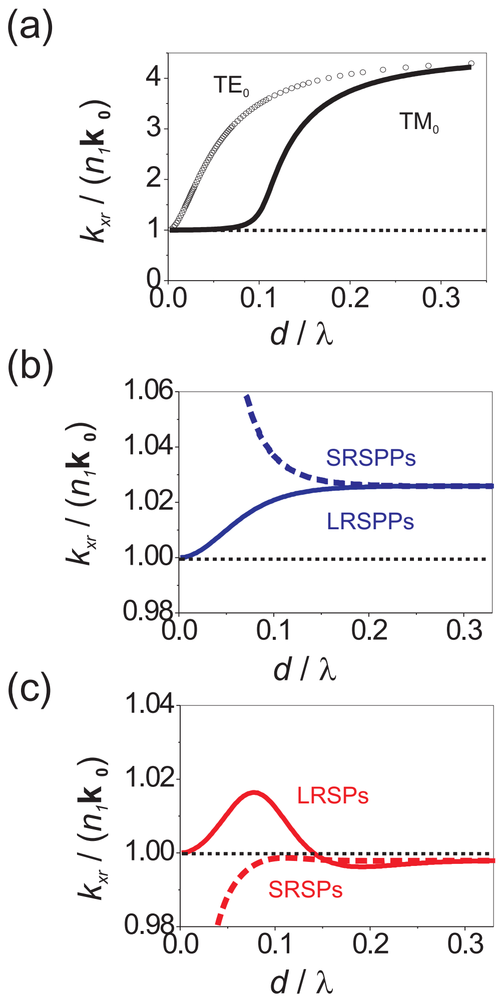

Figure 2.8: Real component of the complex wave number $k_x = k_{xr} + ik_{xi}$, normalized to $n_1\mathbf{k}_0$, of guided modes in a thin slabs with (a) $\epsilon_2 = 20 + 1i$, (b) $\epsilon_2 = -20 + 1i$ and (c) $\epsilon_2 = 1 + 20i$ and surrounded by air as a function of the thickness of the layer normalized by the wavelength at $\lambda = 600$ nm. The dashed line in (b) and (c) indicates the light line in air, $n_1 = 1$.

in the thin layer.

Using Eqs. (2.18)-(2.26), we can calculate the field profiles of the different modes. In Fig. 2.11, we show the field amplitude of H$_z$, E$_x$ and E$_y$ for surface modes in layers with a thickness of 20 nm of a material with (a) $\epsilon_2 = -20 + 1i$

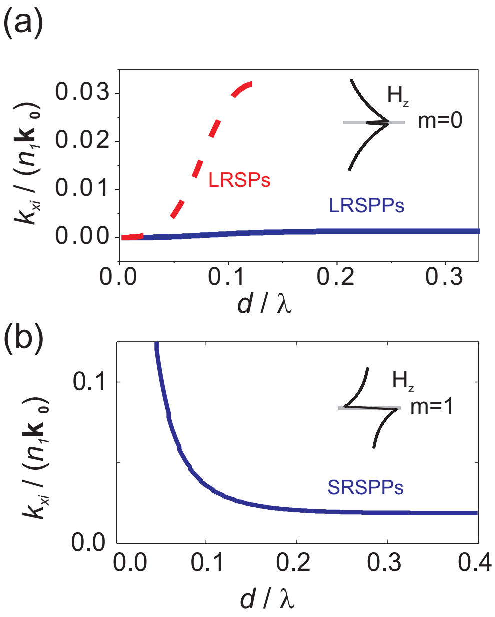

Figure 2.9: (a) Imaginary components of the complex wave number, $k_x = k_{xr} + ik_{xi}$, of long-range and (b) short-range surface modes in thin films of materials with $\epsilon_2 = -20+1i$ and $\epsilon_2 = 1+20i$ surrounded by air. k_{xi} are normalized to $n_1\mathbf{k}_0$ and are displayed as a function of the thickness of the layer normalized by the wavelength at $\lambda = 600$ nm. The inset of (a) and (b) are the field distribution for the symmetric (long-range) and antisymmetric (short-range) modes.

(LRSPPs), (b) $\epsilon_2 = 1+20i$ (LRSPs) and (c) $\epsilon_2 = 20+1i$ (TM$_0$) surrounded by air. The wavelength in these calculations is fixed to 600 nm. We can notice that for the three modes the E$_x$ components are antisymmetric with respect to the middle plane of the thin layer, while the H$_z$ and E$_y$ components are symmetric. The most pronounced difference between the long-range surface polaritons and the TM$_0$ mode is the maximum of magnetic field amplitude inside the layer for the latest, while the first present a relative minimum of this field component inside the thin layer.

From Eq. (2.32), we can derive an analytical expression of the dispersion relation of LRSPs in the thin film limit, i.e., when $\kappa_{y2}d/2 \ll 1$ and $ik_y = \kappa$,

$$\kappa_{y2}d/2 \approx -\frac{\epsilon_2\kappa_{y1}}{\epsilon_1\kappa_{y2}}, \tag{2.36}$$

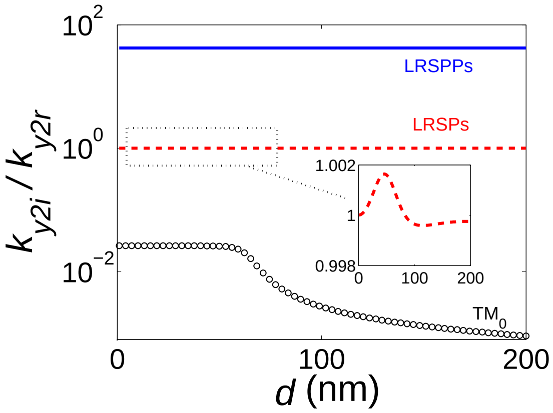

Figure 2.10: Ratio between the imaginary and real (k_y) components of the complex wave number, $k_y = k_{yr} + ik_{yi}$, k_{yi}/k_{yr} of TM surface modes in thin films of materials with $\epsilon_2 = -20 + 1i$ (solid curves), $\epsilon_2 = 1 + 20i$ (dashed curves) and $\epsilon_2 = 20 + 1i$ (circles) surrounded by air at $\lambda = 600\,\text{nm}$. These ratios are plotted as a function of the thickness of the layer d.

where

$$\kappa_{yj} = \sqrt{k_{xr}^2 - \mathbf{k}_0^2\epsilon_j}, j = 1,2\,. \tag{2.37}$$

Combining Eqs. (2.36) and (2.37) we obtain

$$\epsilon_1\kappa_{y1}^2 d/2 + \epsilon_2\kappa_{y1} + \mathbf{k}_0^2\epsilon_1 d/2(\epsilon_1 - \epsilon_2) \approx 0. \tag{2.38}$$

Since d is very small, and assuming that $\epsilon_1 \ll \epsilon_2$,

$$\kappa_{y1} \approx -\frac{\mathbf{k}_0^2\epsilon_1 d(\epsilon_1 - \epsilon_2)}{2\epsilon_2} \tag{2.39}$$

with Eq. (2.37) and $\epsilon_2 = \epsilon_{2r} + i\epsilon_{2i}$, we obtain the real and imaginary components of the wave number of LRSPs,

$$k_{xr} \simeq \mathbf{k}_0\sqrt{\epsilon_1}\left[1 + \frac{\epsilon_1(\epsilon_{2r}^2 + \epsilon_{2i}^2 - \epsilon_1\epsilon_{2r})^2 - \epsilon_1^3\epsilon_{2i}^2}{2(\epsilon_{2r}^2 + \epsilon_{2i}^2)^2}\left(\frac{\pi d}{\lambda}\right)^2\right], \tag{2.40}$$

$$k_{xi} \simeq \mathbf{k}_0\epsilon_1^{3/2}\frac{\epsilon_{2i}(\epsilon_{2r}^2 + \epsilon_{2i}^2 - \epsilon_1\epsilon_{2r})}{(\epsilon_{2r}^2 + \epsilon_{2i}^2)^2}\left(\frac{\pi d}{\lambda}\right)^2. \tag{2.41}$$

Later, in chapter 3 and chapter 6 we will use the analytical expressions of the wave number of LRSPs in the thin film limit to study the dispersion relation of LRSPs in absorbing materials.

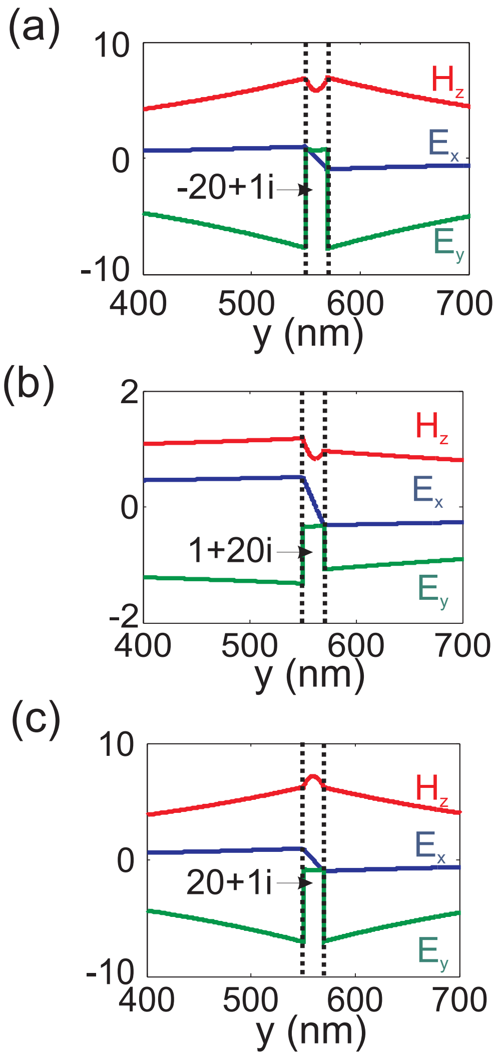

Figure 2.11: H_z, E_x and E_y field components of (a) LRSPPs in a layer with $\epsilon_2 = -20+1i$, (b) LRSPs in a layer with $\epsilon_2 = 1+20i$ and (c) of a TM_0 mode in a layer with $\epsilon_2 = 20+1i$. These layers have a thickness of 20 nm and are surrounded by air. The wavelength of the calculation is $\lambda = 600$ nm.

2.2.2 LRSPs in silver and amorphous silicon thin films

In Fig. 2.12(a) we plot the dispersion relation of a LRSPPs in silver layers with a thickness of 10 and 50 nm surrounded by air, i.e., air/Ag/air. For these calculation we use the values of the permittivity of Ref. [65]. As the thickness of the silver layer increases, the dispersion relation of LRSPPs moves away from the light line. The imaginary components of the wave vector of LRSPPs in these layers are shown in Fig. 2.12(b). As the thickness of the silver increases these components become larger and the losses increases.

We also plot the dispersion relation for LRSPs in an amorphous silicon (a-Si) layer surrounded by air in Fig. 2.12(c). The thickness of the thin film is chosen also to be 10 and 50 nm in order to compare directly the LRSPPs in metal (silver) and LRSPs in strongly absorbing materials (a-Si). The dispersion curve of LRSPs in a-Si is close to the light line. For wavelengths $\lambda > 600$ nm the absorption of a-Si is very low and the guided modes by the thin layers correspond to TM_0 modes.

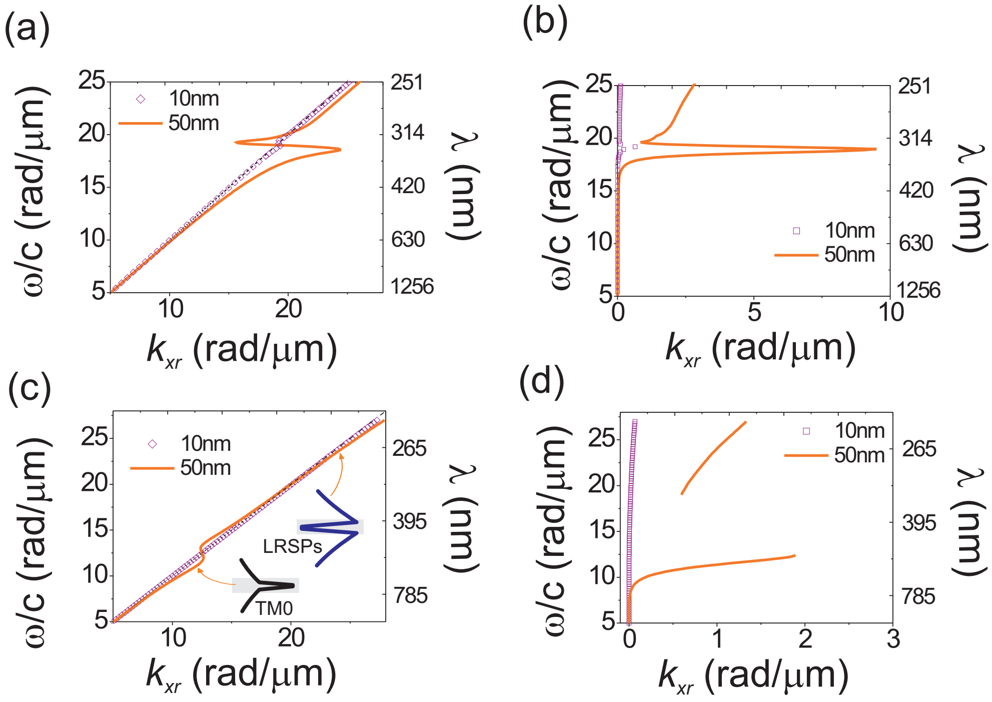

Figure 2.12: (a),(b) Dispersion of long-range Surface plasmon polaritons at the interface of a silver thin layer with air. (c),(d) Dispersion of long-range guided modes at the interface of a amorphous silicon thin layer with air. The thicknesses of the thin layer are chosen for 10 and 50 nm. The dashed line corresponds to the light line in air, $\omega/c = \sqrt{\varepsilon_1}\mathbf{k}_0$. The inset shows the magnetic field component of H_z for the case of 50 nm a-Si supporting TM_0 mode at 600 nm and LRSPs mode at 300 nm.

For the 50 nm thick layer the dispersion relation crosses the light line at ω/c =12 rad μm^{-1} becoming a leaky surface wave. At ω/c =20 rad μm^{-1}, this dispersion crosses again the light line. At higher frequencies the strong absorption of a-Si leads to the formation of LRSPs bounded to the thin layer. The calculated $\mathrm{H_z}$ field profile is given in the inset of Fig. 2.12(c) for the $\mathrm{TM_0}$ and LRSPs modes in the 50 nm of layer a-Si at the frequencies indicated by the arrows. As mentioned in the previous section, the $\mathrm{TM_0}$ mode exhibits a maximum of $\mathrm{H_z}$ inside the thin layer, whereas $\mathrm{H_z}$ has a minimum for the case of LRSPs. Fig. 2.12(d) displays the imaginary component of the wave number of LRSPs for the 10 and 50 nm layers. Note that k_{xi} is only displayed for the frequencies at which $k_{xr} > \mathbf{k}_0 n_1$.

Figure 2.13(a) shows the propagation length as a function of the wavelength and the normalized frequency for LRSPPs guided by a 10 and 50 nm thick film of silver in air. Figure 2.13(b) gives the propagation length, $\mathrm{L_x}$, of guided modes in similar films of a-Si. The propagation length is generally longer for thinner layers. As the thickness is reduced the electromagnetic field extends more into the surrounding dielectric, as illustrated in Fig. 2.14(a) and (b) for silver and a-Si layers where the decay or confinement length of the guided modes is plotted. The longer decay length in the surrounding dielectric is associated with a reduction of the electromagnetic energy density in the absorbing thin layer and the concomitant increase of the propagation length. Note that the propagation length also increases for longer wavelengths. This increase can be attributed in the case of silver to a larger value of the real component of the permittivity that leads to a smaller penetration of the field in the thin absorbing layer. In the case of a-Si, the increase of propagation length at longer wavelengths is caused by the reduction of

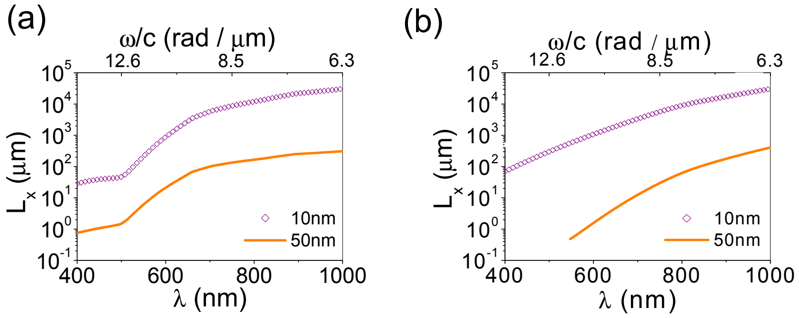

Figure 2.13: (a) Calculated propagation length of long-range Surface polaritons at the interface of a silver with air. (b) Propagation length of long-range Surface polaritons at the interface of a amorphous silicon with air.

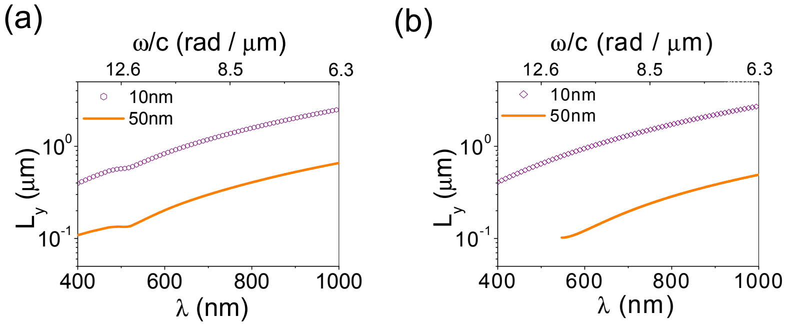

Figure 2.14: (a) Calculated decay length of long-range Surface polaritons at the interface of a lossless Drude metal with air. (b) Decay length of long-range Surface polaritons at the interface of a amorphous silicon with air.

absorption in a-Si.

2.3 Optical excitation method: attenuated total reflection

As we have seen in the previous section, the wave number of LRSPs is larger than that of radiation in free space. In other words, LRSPs are surface waves bounded to the thin films. For this reason, LRSPs can not be excited on a planar surface without an additional coupling mechanism to enable the incident light to gain in-plane momentum or wave number.

In this thesis we use the prisms coupling method, i.e., Kretschmann-Raether configuration, to optically excite LRSPs, note that this mode can only be excited by light with TM polarization. This method [9] rely on the increase of wave number as the wave propagates in a higher refractive index medium. As shown in Fig. 2.15(a), an evanescent wave generated at the prism/dielectric (ϵ_p/ϵ_1) interface by total internal reflection may excite LRSPs in the slab as long as the thickness of the dielectric (ϵ_1) is comparable to the decay length of LRSPs.

A calculation of the reflectance, transmittance and absorbance spectra at λ=375 nm for a d_2 = 10 nm film of amorphous silicon in SiO_2 is shown in Fig. 2.15(b). The prism in this calculation has a permittivity $\epsilon_p = 2.62$, while the thickness of upper SiO_2 layer d_1 is 300 nm. The critical angle for total internal reflection at the prism-SiO_2 interface is $\theta_c = 64°$. This calculation is based on

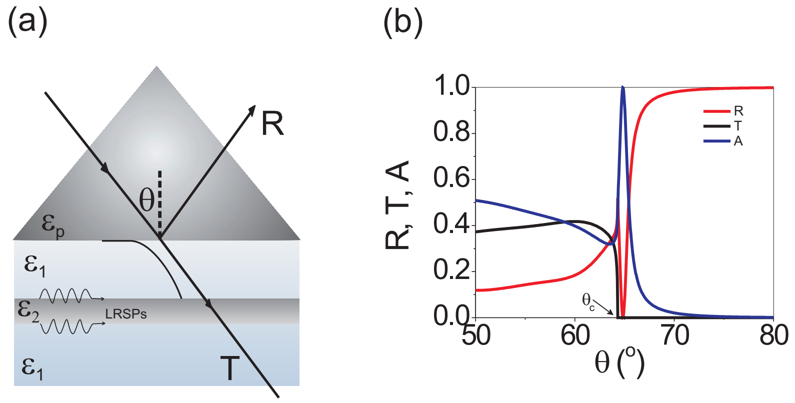

Figure 2.15: (a) The Kretschmann-Raether configuration for excitation of LRSPs. Light incident from the prism side with incident angle of θ and get reflected/transmitted at ϵ_p/ϵ_1 interface. (b) Calculated reflectance, transmittance and absorbance of an 10 nm a-Si thin film (ϵ_2) in SiO$_2$ (ϵ_1) attached with the prism. θ_c corresponds to the critical angle at ϵ_p/ϵ_1 interface.

Fresnel coefficients at the different interfaces of the structure.

$$r_{p1} = \frac{n_1^2 k_{yp} - n_p^2 k_{y1}}{n_1^2 k_{yp} + n_p^2 k_{y1}}, \tag{2.42}$$

$$r_{12} = \frac{n_2^2 k_{y1} - n_1^2 k_{y2}}{n_2^2 k_{y1} + n_1^2 k_{y2}}, \tag{2.43}$$

$$r_{21} = \frac{n_1^2 k_{y2} - n_2^2 k_{y1}}{n_1^2 k_{y2} + n_2^2 k_{y1}}, \tag{2.44}$$

and the corresponding transmission coefficients

$$t_{p1} = \frac{2n_1^2 k_{yp}}{n_1^2 k_{yp} + n_p^2 k_{y1}} \frac{n_p}{n_1}, \tag{2.45}$$

$$t_{12} = \frac{2n_2^2 k_{y1}}{n_2^2 k_{y1} + n_1^2 k_{y2}} \frac{n_1}{n_2}, \tag{2.46}$$

$$t_{21} = \frac{2n_1^2 k_{y2}}{n_1^2 k_{y2} + n_2^2 k_{y1}} \frac{n_2}{n_1}, \tag{2.47}$$

where the wave number perpendicular to each layer is defined as $k_{yj} = \sqrt{\mathbf{k}_0^2 n_j^2 - k_{xj}^2}$ with j=1,2,3,4, n_j is the refractive index of the different media, $\mathbf{k}_0$ is the wavenumber in vacuum and k_{xj} is the wave number parallel to the layer, i.e., k_{xj} =

$\mathbf{k}_0 n_j \sin(\theta)$. The Fresnel amplitude coefficients of reflection and transmission of the slab are given by

$$r_{p121} = \frac{r_{p1} + r_{123} e^{2ik_{y2}d_2}}{1 + r_{p1} r_{121} e^{2ik_{y2}d_2}}, \tag{2.48}$$

$$t_{p121} = \frac{t_{p1} t_{121} e^{ik_{y2}d_2}}{1 + t_{p1} t_{121} e^{2ik_{y2}d_2}}, \tag{2.49}$$

where

$$r_{121} = \frac{r_{12} + r_{21} e^{2ik_{y1}d_1}}{1 + r_{12} r_{21} e^{2ik_{y1}d_1}}, \tag{2.50}$$

$$t_{121} = \frac{t_{12} t_{21} e^{ik_{y1}d_1}}{1 + t_{12} t_{21} e^{2ik_{y1}d_1}}. \tag{2.51}$$

The reflectance and transmittance or the intensity coefficients are given by

$$R = |r_{p121}|^2, \tag{2.52}$$

$$T = \frac{n_1 cos\theta_t}{n_p cos\theta_i} t^2_{p121}, \tag{2.53}$$

where θ_i and θ_t are the incident and transmission angles.

The minimum in reflectance in Fig. 2.15(b) after the critical angle θ_c is the result of coupling of the transmitted evanescent amplitude to LRSPs in the thin layer [77, 78]. Due to the condition of total internal reflection for larger angles than θ_c, there will be no transmitted light through the layered structure. By energy conservation, we can define the absorbance as $A = 1 - R - T$ and we can attribute the high absorption close to 100 % at the resonance position to the efficiently coupling of the incident light into the LRSPs mode and the subsequent dissipation in the thin absorbing layers.

CHAPTER 3

LRSPS SUPPORTED BY THIN FILMS OF AMORPHOUS AND CRYSTALLINE CHALCOGENIDE GLASS

We demonstrate that a thin film of chalcogenide glass can support long-range surface polaritons (LRSPs) modes in the visible. The possibility of changing the phase of this material allows us to investigate the influence of the complex permittivity of the thin film on the dispersion relation of surface modes. The relative insensitivity of the LRSPs modes to the permittivity of the supporting thin layers is discussed.

3.1 Introduction

In this chapter, we study the excitation of surface polariton modes in thin films of strongly absorbing materials, demonstrating that these modes can be supported independently of the value of the real part of the permittivity of the thin film. Specifically, we investigate LRSPs supported by chalcogenide $Ge_{17}Sb_{76}Te_7$ (GST) thin films at visible frequencies. The phase of this material can be changed between crystalline (c-GST) and amorphous (a-GST) by varying the temperature [79]. A phase change also strongly modifies the permittivity of the thin film. This property is the reason why chalcogenide materials are commonly used in optical memory devices and electronic solid state devices [80].

Figure 3.1 displays the permittivity of the c-GST and a-GST thin films, which have been determined by ellipsometry measurements. The imaginary component (Fig. 3.1(b)) is large for the two phases and have a similar value around 600 nm. The largest difference between the two phases concerns the real part of the permittivity (Fig. 3.1(a)): whereas c-GST has a metallic character ($\epsilon_r < 0$), a-GST is an absorbing dielectric above 500 nm ($\epsilon_r > 0$). In ref. [56], it was theoretically predicted that LRSPs supported by very lossy materials are insensitive to changes in the real part of the permittivity. We take advantage of the dramatic changes in the dielectric permittivity between different phases in GST and demonstrate experimentally this prediction.

3.2 Experimental

The investigated sample is formed by a substrate of Schott F2 glass with a permittivity $\epsilon = 2.62$ at $\lambda = 600$ nm. On top of the substrate, we have deposited by electron beam sputtering a 370 nm-layer of silica and a 19 nm-layer of $Ge_{17}Sb_{76}Te_7$ material. The process of layer deposition is as follows: the substrate is placed in a vacuum chamber with the target of phase change materials, where argon gas is introduced at low pressure. A gas plasma is generated and becomes ionized by using an RF power source. The ions are accelerated towards the surface of the target, causing atoms of the phase change material to break off from the target in vapor form and condense onto the surface of the substrate.

The thickness of the silica layer has been determined from a side-view scanning electron microscope image of the cleaved sample made after the optical measurements. The thickness of the chalcogenide thin layer in its amorphous phase has been obtained by X-ray reflectometry. The roughness of the two interfaces of the GST thin film, estimated from the X-ray reflectometry, is about 4 nm. We have

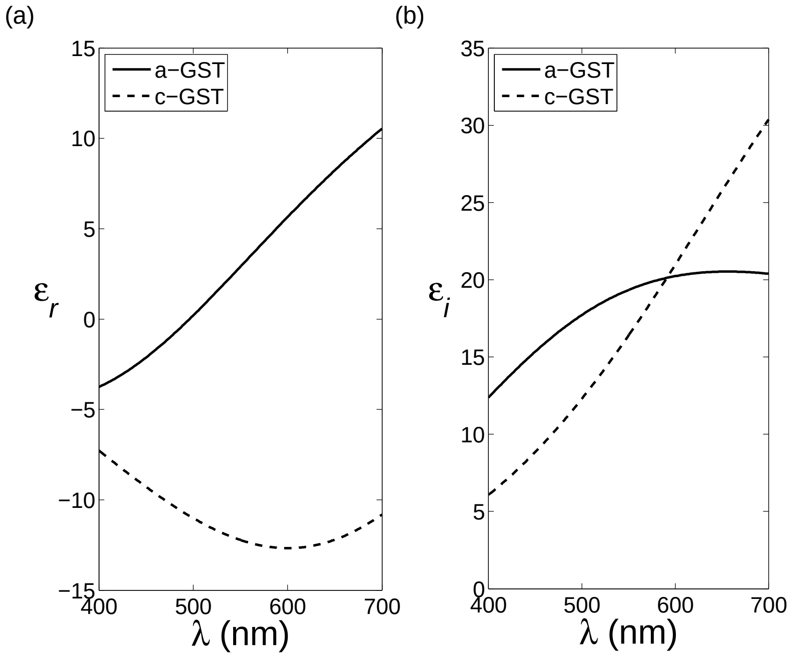

Figure 3.1: Permittivity of $Ge_{17}Sb_{76}Te_7$. The solid lines correspond to the amorphous phase and the dashed lines to the crystalline phase. Figure (a) displays the real component of the permittivity, while (b) shows the imaginary component.

used a liquid (Cargille Labs) to match the refractive index of the SiO_2 top layer in order to have a symmetric medium surrounding the thin film. Refractive indices of the matching index liquid and of the silica layer have been determined by ellipsometry measurements. The difference between these two refractive indices is less than 0.01 in the range of investigated wavelengths.

The Attenuated Total Reflection (ATR) method [9] was used to excite the surface mode (see Fig. 3.2 and section 2.3). A prism of F2 glass, which is index matched to the sample substrate, is used to illuminate the F2-SiO_2 interface at an angle larger than the critical angle for total internal reflection. The evanescent transmitted amplitude can couple to LRSPs at the resonant wavelengths and angles, leading to a reduction of the reflection. We have measured the specular reflection on the F2-SiO_2 interface by varying the angle of incidence of a beam at optical frequencies. The experiments were done with a computer controlled rotation stage set-up that allowed the simultaneous rotation of sample and

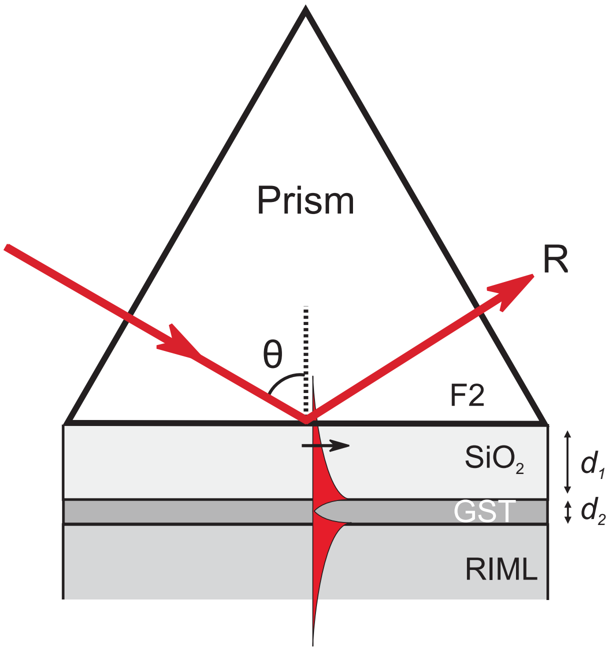

Figure 3.2: Schematic representation of the sample and the experimental method. d_1 is the thickness of the upper SiO_2 layer, d_2 is the thickness of the a-GST layer. The refractive index matching liquid (RIML) is sufficiently thick to be considered infinite. The red arrows indicate the wave vector of the incident and reflected plane wave.

detector. The light source was a collimated beam from a halogen lamp (Yokogawa AQ4303), and we used a fiber coupled spectrometer (Ocean Optics USB2000) to measure the reflection.

Firstly, we have measured the reflectance on the sample formed by the a-GST film in its amorphous phase. Then, the sample was heated up at $250°C$ during 30 minutes in order to change the GST layer in its crystalline phase. Finally, we repeated the reflection measurements on the sample having the GST thin film in its crystalline phase. The references for these measurements were obtained by measuring the reflection of s-polarized light for each phase of the GST thin films and for light incident at an angle larger than the critical angle, i.e., reflectance close to 1. Figure 3.3(a) shows the reflectance of p-polarized light measured on the a-GST sample. A reduction of the total internal reflection in the prism is clearly visible near 65°. This resonance appears after the critical angle for total internal reflection, which is around 63.7°. The minimum of reflectance is almost zero (5%),

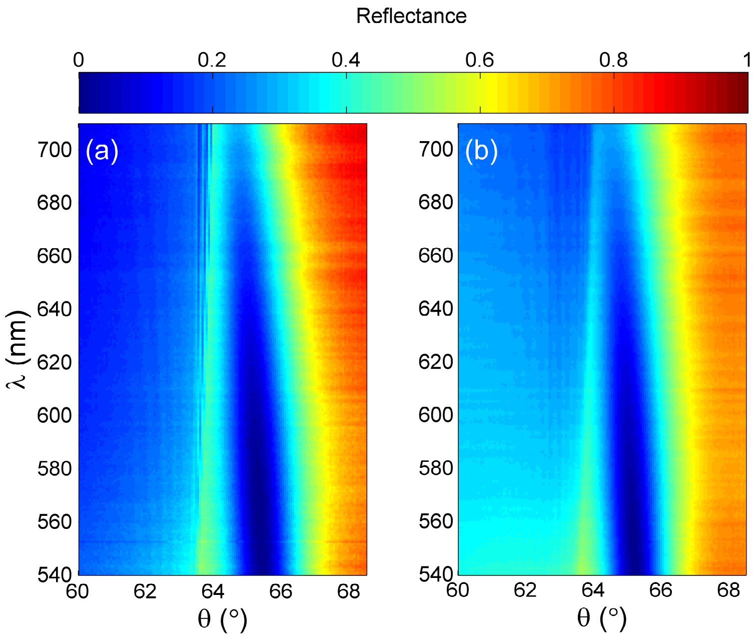

Figure 3.3: Reflectance measured in the ATR configuration as a function of the wavelength and the incident angle on amorphous-GST (a) and crystalline-GST (b) thin films.

revealing the very efficient coupling of the incident light to LRSPs. Figure 3.3(b) displays the reflectance of the c-GST sample. The resonance is similar for the two phases of GST in terms of linewidth, resonance angle and coupling efficiency. This similarity is better seen in Fig. 3.4(a) and (b), which displays the reflectance as a function of the incident angle at λ =600 nm for both phases. The linewidths of these resonances are 1.3° for c-GST and 1.7° for a-GST. The difference on the resonance angle between the two phases is 0.2°. The difference in the reflectance at smaller angles than the critical angle confirms the different permittivity between the two phases of the thin film.

The symbols in Fig. 3.4 are fits to the measurements for the two phases calculated by solving the Fresnel's equations for the multilayer structure (see section 2.3 in chapter 2). The only adjusted parameter in the fits is the thickness of the thin film. The permittivities of each layer of the sample were fixed to the values obtained from ellipsometry measurements. From the fits, we obtain an amorphous layer with a thickness of 22.5±0.5 nm and a crystalline layer of 20.5±0.5 nm. It is reasonable to think that the change of phase can slightly modify the thickness

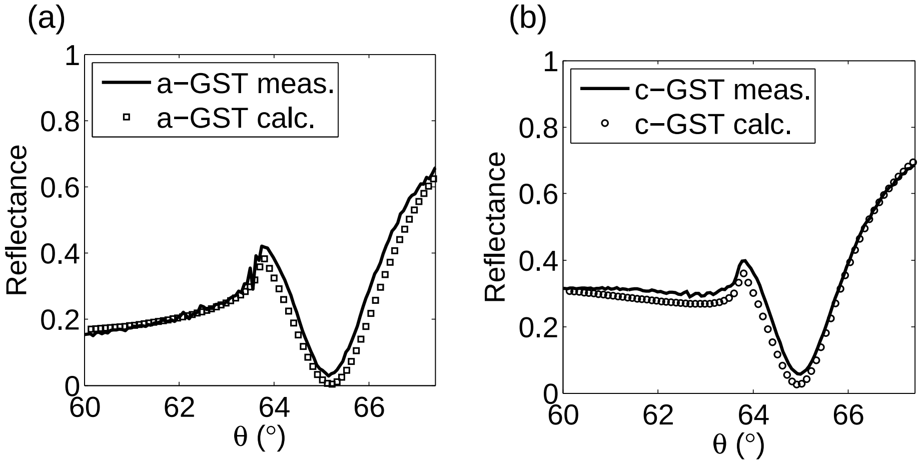

Figure 3.4: Reflectance at 600 nm as a function of the internal angle of incidence, for the amorphous (a) and crystalline (b) phases of the GST thin film. The cross and open circles are the calculated reflectances for the amorphous and crystalline thin films respectively.

of the layer, as it has been already reported for different phase change materials [81, 82]. The small shift of the resonance is thus partly due to this variation of thickness. The thickness of the amorphous GST thin film which we obtained from the fits is in reasonable agreement with the value of 19 ± 4 nm obtained by X-ray reflectometry.

Figure 3.5 shows the dispersion relation of the LRSPs, i.e., $\omega/c = 2\pi/\lambda$ versus $k_x = 2\pi n_{\mathrm{SiO_2}} \sin\theta/\lambda$, for both phases. These dispersion relations have been obtained from the measurements of Fig. 3.3, by plotting the angles and wavelengths of minimum in reflectance. The solid line is the edge of the light cone in silica. This figure reveals the similarity of the modes despite the large difference in the permittivity of the thin film.

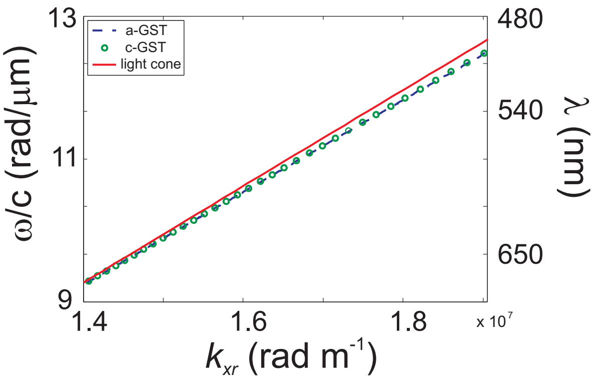

Figure 3.5: Dispersion relation of LRSPs measured for the amorphous (dashed line) and crystalline (open circles) phases of the GST thin film. The solid line is the light cone in silica.

3.3 Mode calculation

To go deeper in the analysis of guided modes supported by thin layers of chalcogenide glasses, we have calculated the mode index, i.e., $n_{\text{sp}} = k_{xr}/\mathbf{k}_0$, and propagation length in the three layer system silica / thin film / silica. Figure 3.6 represents the mode index at $\lambda = 600$ nm for a film with a thickness of 20 nm as a function of its permittivity. The x-axis defines the real component of the permittivity of the thin film ϵ_r, whereas the y-axis is the imaginary component ϵ_i. These results have been obtained in the thin film limit, by using Eq. (2.40). The propagation length is defined as $Lx = 1/2k_{xi}$ where k_{xi} is given by Eq. (2.41).

We can notice in Fig. 3.6 that almost any material can support surface waves in this configuration. Only a small range of permittivities defined by the following relation $\epsilon_r^2 + \epsilon_i^2 < \epsilon_{\text{SiO}_2}\epsilon_r$ and marked with the white area close to the origin on Fig. 3.6 do not support any surface mode [56]. The square and circle in Fig. 3.6 represent the a-GST and c-GST thin films at $\lambda = 600$ nm. For this wavelength, we find values of n_{sp} reaching 1.475 and 1.476 for a-GST and c-GST respectively. The propagation length is about 12λ and 16λ for a-GST and c-GST layers as showed in Fig 3.7. Note that in spite of the very large absorption of a-GST and c-GST layers with a bulk absorption length of about 1 μm at $\lambda = 600$ nm, LRSPs can propagate several wavelengths.

When $\epsilon_r^2 + \epsilon_i^2 \gg \epsilon_{\text{SiO}_2}^2$, the wave number of the mode $k_x = k_{xr} + i k_{xi}$ in Eqs. (2.40)

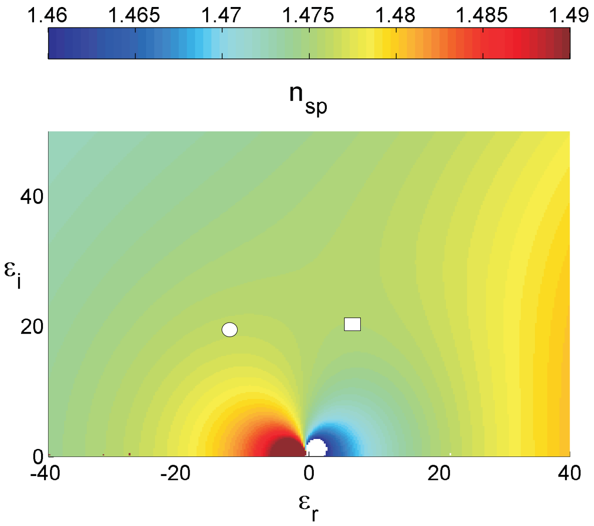

Figure 3.6: Effective index as a function of the permittivity of the thin film, calculated at λ =600 nm, for a thickness of the thin film equal to 20 nm. The symmetric surrounding medium is silica. The square and circle markers indicate the permittivity of the a-GST and c-GST respectively.

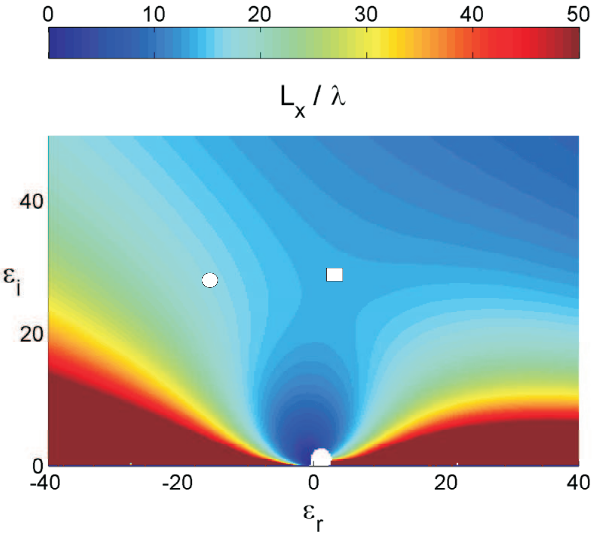

Figure 3.7: Propagation length of the modes normalized to the wavelength. The square and circle markers indicate the permittivity of the a-GST and c-GST respectively.

and (2.41) reduce to

$$k_{xr} \simeq \mathbf{k}_0 \sqrt{\epsilon_{\mathrm{SiO_2}}} \left[1 + \frac{\epsilon_{\mathrm{SiO_2}}}{2} \left(\frac{\pi d_2}{\lambda} \right)^2 \right], \tag{3.1}$$

and

$$k_{xi} \simeq \mathbf{k}_0 \epsilon_{\mathrm{SiO_2}}^{3/2} \frac{\epsilon_i}{\epsilon_r^2 + \epsilon_i^2} \left(\frac{\pi d_2}{\lambda} \right)^2, \tag{3.2}$$

where $\mathbf{k}_0$ is the vacuum wave number and d_2 is the thickness of the thin film. This expression is only valid in the thin film limit [56], i.e., when $|\frac{1}{2}\kappa_y d_2| \ll 1$, being κ_y the component of the wave number inside the thin layer normal to the surface.

According to Eq. (3.1), the mode index, n_{sp}, becomes independent of the permittivity of the thin film when this is large enough. We can clearly see this trend in the exact calculation of Fig. 3.6 for a wide range of permittivities, where the value of the mode index is around 1.477. We point out that the permittivity of the a-GST material is in the range of values for which the mode index of LRSPs is nearly unaffected by changes on this permittivity, which is in agreement with the measurements where we did not observe layer differences in the attenuated total reflection of the a-GST and C-GST films.

In the case of very lossy thin film, i.e., when $\epsilon_i^2 >> \epsilon_r^2$, k_{xi} in Eq. (3.2) reduces to

$$k_{xi} \simeq \mathbf{k}_0 \frac{\epsilon_{\mathrm{SiO_2}}^{3/2}}{\epsilon_i} \left(\frac{\pi d_2}{\lambda} \right)^2. \tag{3.3}$$

In this case, neither the real component, nor the imaginary component of the wave number of the surface polaritons depends on ϵ_r. The surprising result we also find in this limit is that the propagation length, which is proportional to the inverse of k_{xi}, increase linearly with ϵ_i, i.e., with the absorption in the thin layers. This behavior can be appreciated in Fig. 3.7, where we can see that the propagation length increases with ϵ_i if $\epsilon_r << \epsilon_i \lesssim 20$. However, between $\epsilon_i \sim 20$ and 30, the propagation length seems to be nearly constant and for $\epsilon_i > 30$, L_x decreases as ϵ_i increases. This discrepancy between the analytic expression of Eq. (3.3) and Fig. 3.7 is due to the fact that for $\epsilon_i > 20$ and $d_2 = 20$ nm, we are not in the thin-film approximation anymore. For instance, for $\epsilon = 20i$, the value of $|\frac{1}{2}\kappa_y d_2|$ is equal to 0.5. It is worth noticing that for a thickness of 20 nm, both the mode index and the propagation length of LRSPs are relatively insensitive to the permittivity of the thin film for a wide range of permittivities. We emphasize that this situation can be found at any wavelength by adjusting the thickness of the thin film.

3.4 Conclusion

We have shown that a 20 nm thin film made of chalcogenide $Ge_{17}Sb_{76}Te_7$ material can support long range surface polaritons in the visible. By changing the phase of this material, we have also investigated the dependence of surface modes supported by lossy thin films with their permittivity. We have demonstrated the relative insensitivity of the mode with the real component of the permittivity of the thin film, even if the thin-film approximation is not fulfilled.

CHAPTER 4

LRSPS SUPPORTED BY SILICON AT VISIBLE AND ULTRAVIOLET FREQUENCIES

The large imaginary component of the dielectric constant of amorphous silicon (a-Si) at visible and ultraviolet (UV) frequencies allows the excitation of long-range surface polaritons (LRSPs) modes. Propagation of these modes along considerable distances is possible because the electric field is largely excluded from the absorbing thin film. Using the attenuated total internal reflection method, we show that by decreasing the thickness of the Si layer these modes can be excited at UV frequencies.

4.1 Introduction

In this chapter, we investigate the excitation of long-range surface polaritons (LRSPs) in ultra-thin layers of amorphous Si (a-Si) at frequencies where a-Si is an strongly absorbing dielectric, i.e., frequencies at which Si has a positive real component of the permittivity and large imaginary component. These modes on films of a-Si have similar or even superior characteristics than long-range surface plasmon polaritons (LRSPPs) on gold films, with long propagation lengths and similar confinement to the thin film. Silicon is the most thoroughly investigated semiconductor and the ability to deposit with high precision atomically flat layers of this semiconductor, combined with the possibility of exciting surface modes on ultra-thin layers, could have important implications in several fields, including photovoltaics [25], near-field microscopy [13], optical data storage [64], optical lithography [21] and sensing [34].

4.2 Experimental

4.2.1 Sample fabrication

As we have discussed in section 3.3, the thickness of the thin film is a critical parameter that determines the wavelength and angles for coupling of an incident plane wave to a LRSPs in an attenuated total internal reflection configuration. In order to investigate experimentally the excitation of LRSPs at UV and visible frequencies in thin films of a-Si, we have fabricated two different samples. The first sample is an a-Si film with a thickness of 13 nm sputtered onto a SiO_2 substrate and covered by 350 nm of SiO_2. As it is shown in section 4.2.2, this sample supports LRSPs in the UV. A scanning electron microscope side view image of the sample is shown in Fig. 4.1. In the second sample we increase the thickness of a-Si thin film to 20 nm and it is covered by 500 nm of SiO_2.

An important aspect which determines the propagation length of long-range guided modes in thin films is the surface roughness. Scattering by inhomogeneities on the surface leads to coupling into radiation. These radiation losses could reduce the propagation length of guided modes. We have determined the roughness of the thin films by performing atomic force microscopy measurements (Fig. 4.2) on a similar layer of sputtered a-Si with a thickness of 12.5 nm on top of a SiO_2 substrate and compared to an Au layer sputtered on BK7 substrate. To improve the adhesion of Au to the substrate, there is a 3nm of Ti between the Au and the substrate. Fig. 4.2(a) diplays an AFM image of the SiO_2 substrate, while (b) and (c) are images of the a-Si and Au layers respectively. Cuts to Figs. 4.2(a), (b) and

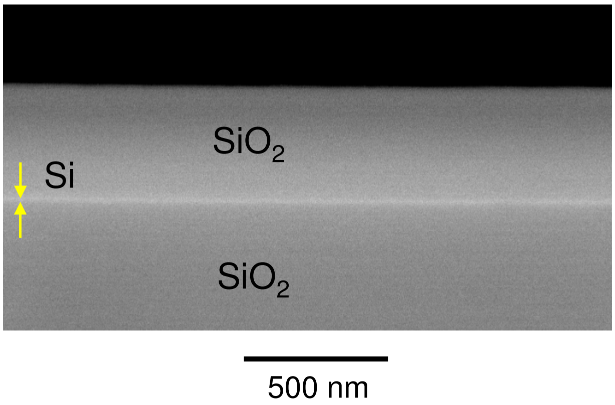

Figure 4.1: SEM micrographs of the fabricated multilayer structure, shown in cross-section. The three layer system consists of 13 nm of Si surrounded by 345 nm SiO$_2$ on top and a thick SiO$_2$ substrate on the bottom.

(c) are showed in Fig. 4.2(d)-(f) for comparison reason. The AFM measurements on a-Si film lead to a root mean square value of the surface roughness R_q of about 0.35 nm, which was determined by the roughness of the substrate. The roughness of the Au film is 2 nm. Due to the formation of Au islands during sputtering of thin layers [55], surface roughness of thin films of gold are one order of magnitude larger than the roughness of a-Si layers with a similar thickness. Consequently, ultra-thin layers of a-Si could have better characteristics than gold layers for the propagation of long-range surface polaritons. As we will see in the next section, by comparing measurements to the theory for perfectly flat thin films, we can neglect radiation losses in a-Si layers.

The dielectric permittivity of ultra thin layers may be different to that of bulk materials due to quantum confinement and interfacial strain. To verify if the effects are relevant in our samples, we have determined experimentally the permittivity by using ellipsometry measurements performed in layers of a-Si films (see Fig. 4.3). Within the experimental error, all the samples had a permittivity equal to that of bulk a-Si [84].

4.2.2 ATR configuration and reflectance measurement

The excitation of LRSPs in the films of a-Si was investigated with attenuated total reflection (ATR) measurements. As we have seen in chapter 3, it is not possible to couple free space light to LRSPs in a thin film below a critical thickness ($d \ll \lambda$) due to momentum or wave number mismatch. A prism with a higher permittiv-

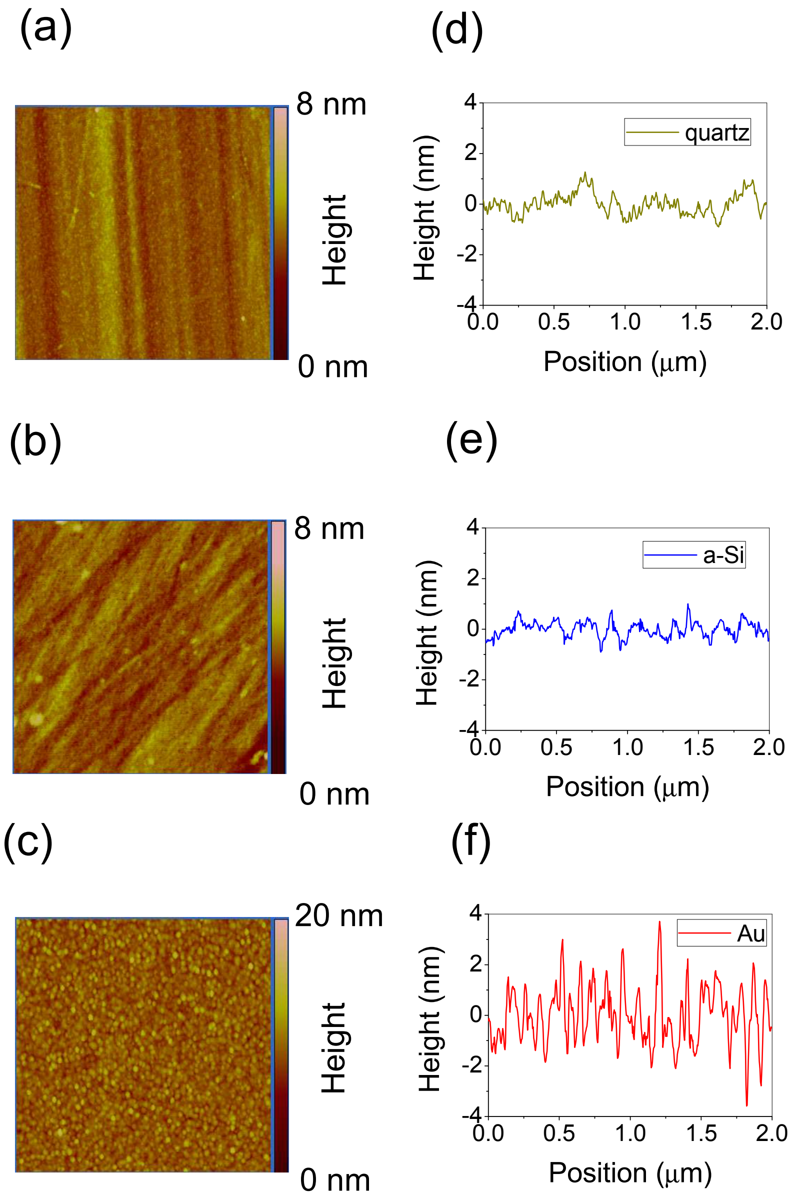

Figure 4.2: AFM images of a SiO_2 substrate (a), an amorphous silicon thin film with a thickness of 13 nm on top of a SiO_2 substrate (b), and (c), a gold layer of a thickness of 44.2 nm on top of BK7 substrate with 3 nm of Ti for adhesion purposes. The gold layer is purchased from Biacore [83] and it is a standard substrate for surface plasmon resonance sensors. (d),(e)(f) are line scans of the SiO_2, amorphous silicon and gold AFM images, which lead to R_q the measured surface roughness.

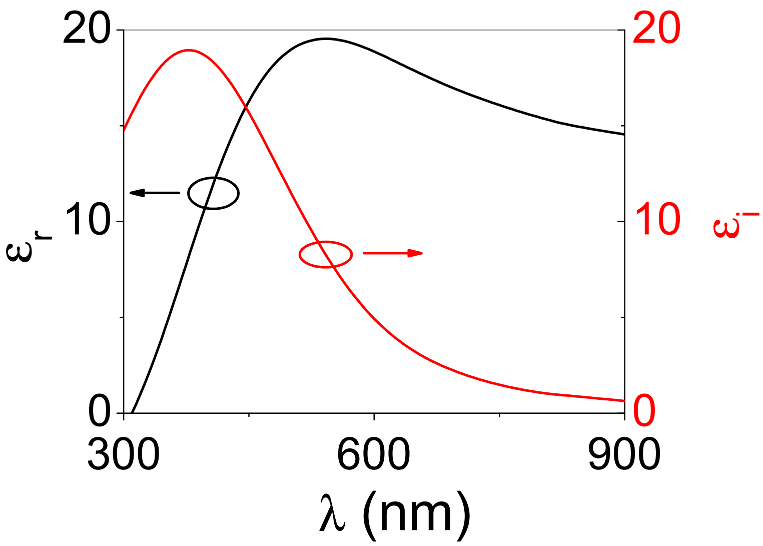

Figure 4.3: Real and imaginary components of the permittivity of an a-Si thin film with a thickness of 13 nm as a function of wavelength.

ity than the dielectric surrounding the thin film can be used to match the wave number of the incident light to the wave number of LRSPs. In our experiments, we used a prism of F2 Schott optical glass placed on top of the samples. The specular reflection at the prism-SiO_2 interface was measured for different angles of incidence and at different wavelengths (see Fig. 4.4). The incident beam is total internally reflected at angles larger than the critical angle of the prism-SiO_2 interface. However, the evanescent transmitted field can resonantly couple to LRSPs at certain angles and wavelengths. This coupling to LRSPs leads to the reduction of the reflected intensity.

The experiments were done in a computer controlled rotation stage set-up that allowed the simultaneous rotation of sample and detector. We used a laser diode (Picoquant PDL 800-B) emitting at a wavelength $\lambda = 375$ nm and a Si photodiode as detector to investigate the UV excitation of LSRPs. We also used a collimated beam from a halogen lamp (Yokogawa AQ4303) and a fiber coupled spectrometer (Ocean Optics USB2000) to perform broadband measurements at optical frequencies. The angle of incidence was varied by rotating the sample in steps of 0.05 degrees. Figure 4.5(a) displays the reflectance measurement of a p-polarized beam of the halogen lamp on the sample with the a-Si film of 20 nm. Calculations of the reflectance in the same configuration are also presented in

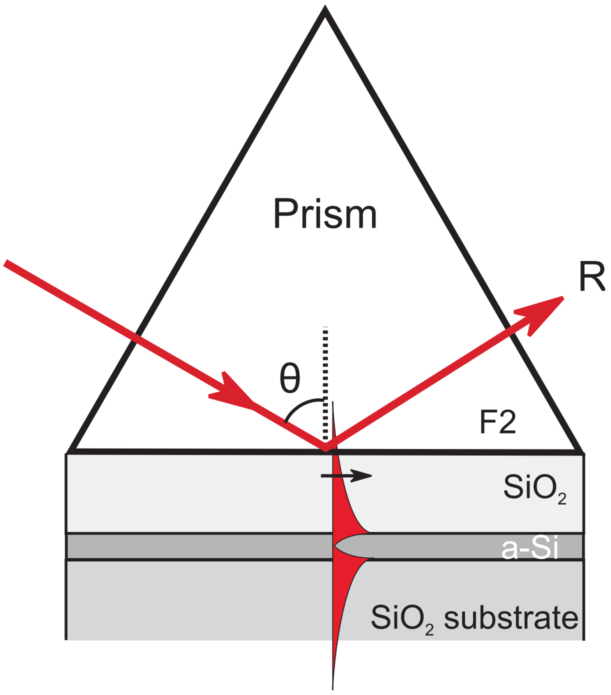

Figure 4.4: The ATR configuration used for the coupling of incident light to LRSPs in the a-Si layers.

Fig. 4.5(b). These calculations are based on solving Fresnel reflection coefficient in a four layers system as described in section 2.3.

The increase of reflectance close to $\theta = 62°$ at long wavelengths in Fig. 4.5(a) and (b) corresponds to the total internal reflection at the critical angle on the prism-SiO_2 interface. The excitation of guided modes in the a-Si is manifested by the narrow band of low reflectance around 63.5° and $\lambda \simeq 550$ nm. This band actually covers the transition between a LRSPs due to high absorption in a-Si at short wavelengths ($\varepsilon \approx 17 + 15i$ at at $\lambda = 450\,\text{nm}$) to the TM_0 [85] modes like in a weakly absorbing a-Si layer at long wavelengths ($\varepsilon \approx 16 + 2.4i$ at $\lambda = 700\,\text{nm}$). As previously pointed by Yang *et al.* in Ref. [56] and as can be appreciated in Fig. 4.5, there is not a drastic transition between LRSPs and the TM_0 mode as the absorption in the thin film increases.

The resonant wavelength of excitation of LRSPs can be tuned by varying the coupling between surface polaritons at the opposite interfaces of the absorbing film. This tuning can be achieved by changing the thickness of the film and the

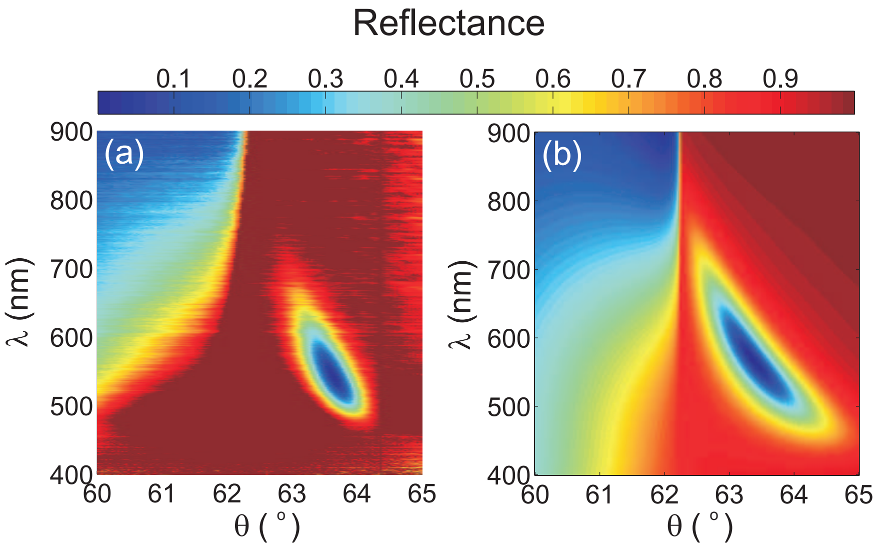

Figure 4.5: (a) Measurements and (b) calculations of the reflectance of p-polarized light incident at an angle θ on the system formed by F2 glass, a SiO_2 layer with a thickness of 500 nm, a 20 nm layer of a-Si and a SiO_2 substrate.

SiO_2 layer on top. A detailed analysis of the modification of the characteristic lengths of guided modes in thin a-Si layers of different thickness is presented in chapter 5. Here, we present measurements at $\lambda = 375$ nm (circles) and calculations (curves) of the reflection of the a-Si layer with a thickness of 13 nm covered by a SiO_2 layer of 350 nm (see Fig. 4.6). The theoretical curves were obtained by using the thickness of the SiO_2 and a-Si layers as free parameters to fit the measurements. The permittivities of a-Si and SiO_2, determined by ellipsometry measurements,were kept fixed in the fits. The values of the thickness of the a-Si layer and of the SiO_2 layer obtained from the fits are $13\pm\, 0.1$ nm and $345\pm\, 5$ nm respectively. These values are in agreement with the SEM image of Fig. 4.1.

The measurement (circles) and calculation (solid line) of the p-polarized reflectance in Fig. 4.6 have a sharp dip at an angle $\theta = 63.6°$, larger than the critical angle of total internal reflection ($\theta_c \simeq 62°$). At $\theta = 63.6°$ the wave number of the evanescent transmitted beam through prism-SiO_2 interface matches the wave number of the LRSP and coupling is possible, giving rise to the reduction of the reflection. For $\lambda = 375$ nm the absorption in a-Si is very strong ($\varepsilon = 10.8 + 19.9i$) and this minimum in the reflection can be attributed to coupling to LRSPs. No particular features are found in the reflectance of s-polarized light (triangles and

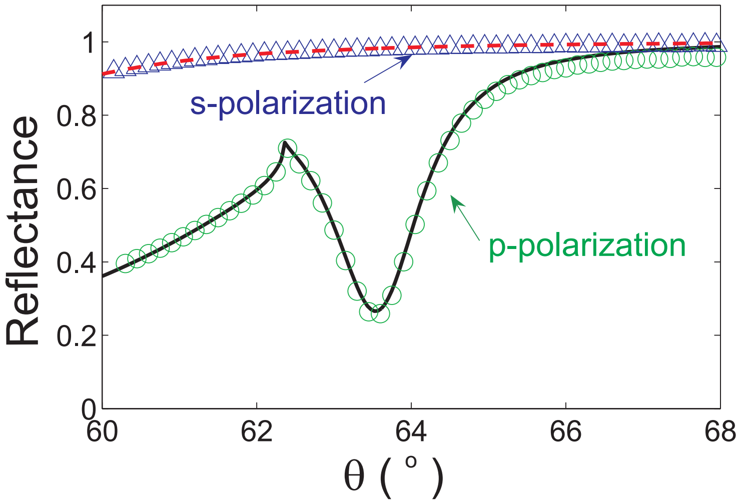

Figure 4.6: Experimental (open circles and triangles) and theoretical (curves) reflectivity at $\lambda_0 = 375$ nm of the system formed by F2 glass, a SiO_2 layer with a thickness of 345 nm, an a-Si layer with a thickness of 13 nm and a SiO_2 substrate. The green circles and solid black curve correspond to p-polarized light, while the blue triangles and red dashed curve correspond to s-polarized light.

dashed line in Fig. 4.6). For this polarization and configuration it is not possible to excite LRSPs.

4.2.3 Near-field calculation

Figure 4.7(a) displays a calculation of the magnetic field amplitude by using Eq. (2.36) for a p-polarized light incident at 63.6°. The configuration chosen for this calculations is similar to the experiments of Fig. 4.6. Only the incident field is present in the prism (upper part of the plot), as can be appreciated by the absence of interference that would point to specular reflection at the prism-SiO_2 interface. This vanishing reflection arises from the perfect coupling of the evanescent field transmitted into the SiO_2 layer to LRSPs in the thin a-Si layer. The maximum field amplitude of the LRSP in Fig. 4.7(a) is at the surface of the a-Si film and decays evanescently from this layer into the surrounding dielectric. For clarity, we display on Fig. 4.7(b) with a red solid curve a vertical cut of the upper contour plot of Fig. 4.7(a). To make the a-Si layer visible, we have scaled its thickness in this figure. The oscillatory amplitude on the upper part of the figure corresponds to the incident field in the prism. We can see a small dip in the magnetic field amplitude in the center of the a-Si thin film and the exponential amplitude decay in the surrounding SiO_2 characteristic of a surface wave. The electric field amplitude component along the x-direction at $x = 0$ is also represented in Fig. 4.7(b) with a black dashed line. This field amplitude is asymmetric with respect to the middle plane of the thin film, as it is expected for long-range surface polaritons [56].

4.3 Discussion

To illustrate the idea of LRSPs waveguides at the UV frequencies, it is important to calculate the characteristic lengths of these modes, i.e., propagation length and

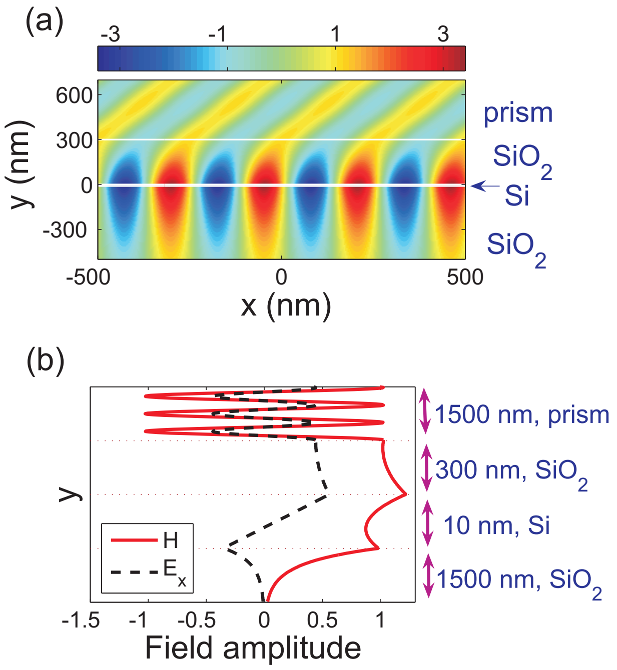

Figure 4.7: The calculation is at $\lambda = 375$ nm of a sample formed by a prism ($n_{\text{prism}} = 1.67$) on top of a SiO_2 layer with a thickness of 300 nm, an a-Si layer with a thickness of 10 nm and a SiO_2 substrate ($n = 1.48$). The dielectric constant of a-Si at $\lambda = 375$ nm is $\epsilon = 10.8 + 19.9i$. (a) Calculation of the magnetic field amplitude for a p-polarized beam ($\lambda = 375$ nm) incident at 62.9° onto the sample. Magnetic field amplitude (full curve) and x-component of the electric field (dashed curve) at $x = 0$ are shown in (b). Note that, for clarity, the SiO_2 layer and the silicon film are scaled.

confinement. As it was discussed in chapter 2, the propagation length L_x is related to the imaginary component of the wave number k_{xi} along the propagation direction by $L_x = 1/2k_{xi}$. Recalled from Eq. (2.17), the confinement length L_y is the decay length from the thin layers to the surrounding dielectric and is given by $L_y = 1/\left[2Re\sqrt{k_x^2 - \mathbf{k}_0^2 n_d^2}\right]$, where k_{xr} is the real component of the wave number of the mode, $\mathbf{k}_0$ is the wavenumber in vacuum and n_d is the refractive index of surrounding dielectric. The complex wave number of the surface mode along the propagation direction $k_x = k_{xr} + ik_{xi}$ can be obtained from Eq. (2.40) and (2.41). Note that in these calculations we consider the thin film surrounded by infinite thick media. We do not take into account the effect of the prism onto the propagation and confinement lengths.

The propagation length L_x at $\lambda = 318$ nm of LRSPs calculated for a-Si films surrounded by a dielectric with $n_d = 1.45$ is displayed in Fig. 4.8(a) as a function of the thickness of the film (blue solid curve). For comparison we have also plotted in Fig. 4.8(a) the propagation length of LRSPs in similar thin films of gold (red solid curve) at $\lambda = 318$ nm, and for a-Si and gold at $\lambda = 650$ nm (blue and red dashed curves respectively). In general, L_x decreases as the thickness of the film increases, approaching the values of surface polaritons at single interfaces. A remarkable behavior is found by comparing the propagation lengths of LRSPs in Au and a-Si layers: L_x in the case of a-Si films is close to or in general longer than the propagation length in Au in spite to be commonly accepted that metals are superior for the propagation of long-range polaritons. This behavior can be also seen in the inset of Fig. 4.8(a). The values of the permittivity of Au and a-Si are displayed in table 4.1 for λ =318, 450 and 650 nm, together with the values of L_x for a film of thickness $d = 5$ nm. It should be pointed out that the guided mode in a-Si at $\lambda = 650$ nm, with a remarkable long propagation length, corresponds to the TM_0 mode in the weakly absorbing layer at this wavelength.

Table 4.1: Characteristic length of long-range guided modes in a film with a thickness of 5 nm of amorphous Si and gold surrounded by a dielectric with refractive index $n_d = 1.45$. Calculated values of propagation length L_x and decay length L_y into the dielectric at three different wavelengths $\lambda = 318$, 450 and 650 nm. The permittivities of the materials at these wavelengths are also listed.

	a-Si			Au		
λ_0 (nm)	ε	$L_x(\mu m)$	$L_y(nm)$	ε	$L_x(\mu m)$	$L_y(nm)$
318	$0+18.5i$	26	216	$-0.2+7.0i$	10	194
450	$17.6+13.5i$	157	485	$-1.26+5.7i$	24	356
650	$17.3+3.0i$	1323	1112	$-9.7+1.0i$	1045	825

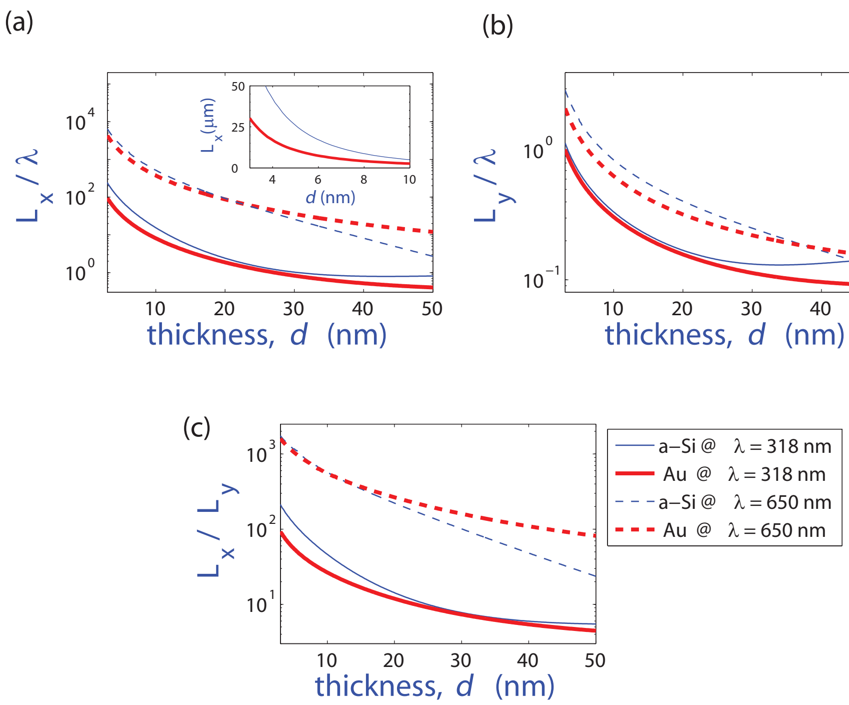

Figure 4.8: (a) LRSP propagation length L_x normalized by λ_0 in a film of thickness d of gold (thick red curves) and silicon (thin blue curves) surrounded by a dielectric with refractive index $n_d = 1.45$. The solid curves correspond to $\lambda = 318$ nm, while the dashed curves are the calculations for $\lambda = 650$ nm. The inset represents a close view of L_x at $\lambda = 318$ nm for small values of d. (b) decay length of the field intensity L_y (normalized by λ) in the dielectric for the same materials and wavelength as in (a). (c) Figure of merit of thin-film guiding structures defined as L_x/L_y for the same materials and wavelengths as in (a).

The decay lengths of these modes in the surrounding dielectric L_y are displayed in Fig. 4.8(b) as a function of the thickness of the thin layer and in table 4.1 for $d = 5$ nm. These decay lengths illustrate the mode confinement to the film. Again, very similar values of L_y are found for Au and a-Si in the UV and in the visible. As the thickness of the thin layer is reduced, the mode is excluded from this layer decaying a longer distance into the dielectric.

The figure of merit (FOM) describing the quality of waveguiding structures can be defined as the ratio between the propagation length and the decay length into the surrounding dielectric L_x/L_y [29, 50]. Large values of this FOM indicate the preferable situation of a long propagation length and strong field confinement. The FOM is displayed in Fig. 4.8(c) for silicon (thin blue curves) and gold (thick red curves) at λ = 318 nm (full curves) and at λ = 650 nm (dashed curves). In general, due to the strong increase of L_x for small values of d, the FOM increases in spite of the also larger values of L_y. At λ = 318 nm the performance of a-Si thin films is better than that of gold. At λ = 650 nm similar FOMs are obtained only for the thinnest layers. The FOM represented in Fig. 4.8(c) correspond to calculations considering thin films without roughness. Surface roughness, inherent to real systems, will reduce L_x. However, as we have seen in section 4.2, it is possible to sputter very thin layers of a-Si (~ 10 nm) with high precision and with a roughness in the sub-nanometer range.

4.4 Conclusion

We have demonstrated the excitation of long-range surface polaritons LRSPs in ultra-thin films of amorphous silicon at visible and UV frequencies. These modes have similar characteristics to long-range surface plasmon polaritons and TM_0 modes with the important difference that LRSPs are sustained by thin layers of strongly absorbing media while surface plasmon polaritons and TM_0 are supported by thin layers of metals and non-absorbing dielectrics respectively. Excitation of long-range surface modes in absorbing Si opens the possibility to surface polariton optics compatible with standard Si processing technology.

CHAPTER 5

CONTROLLING THE DISPERSION OF GUIDED MODES IN THIN LAYERS OF AMORPHOUS SILICON

By varying the thickness of a thin layer supporting long-range guided modes it is possible to tune the dispersion of these modes. We present a systematic investigation of the dispersion of guided modes in nanometric layers of amorphous silicon (a-Si) of different thickness and derive from the experiment the most relevant characteristics of these modes, namely the propagation length, confinement length and group velocity.

5.1 Introduction

We have seen in the previous chapter that by changing the thickness of a thin layer of a-Si surrounded by SiO_2 it is possible to shift the resonant condition for coupling to guided modes in the thin layer over the visible spectrum. We have shown theoretically that a change in thickness leads to a modification of the propagation length and confinement of the field to the layer.

In this chapter, we extend the investigation of the influence of the thickness of thin layers on the characteristics of surface modes by measuring the dispersion of these modes. The measurements have been done in several layers of a-Si, with a thickness in the range 6 to 36 nm, surrounded by SiO_2 (see Fig. 4.4). We have derived the dispersion relation of the surface modes from attenuated total internal reflectance (ATR) measurements. The resonance frequencies span over the whole visible and near IR spectrum. Therefore, the surface modes can be associated to TM_0 modes guided by weakly absorbing Si in the IR and to long-range surface polaritons (LRSPs) at higher frequencies, i.e., in the blue/green regions of the visible spectrum where a-Si absorbs light very efficiently. A detailed analysis of the dispersion measurements allows us to investigate the characteristic lengths of the modes. We have derived the propagation length and the decay length of the field from the layers as a function of their thickness. Thinner layers lead to longer propagation lengths and weaker confinement of the field, i.e., longer decay lengths.

5.2 Experimental

Five samples were prepared as follows: a-Si thin films with different thicknesses were sputtered onto Schott SiO_2 glass substrates. Additional SiO_2 layers were subsequently deposited with a fixed thickness of 550 nm covering the a-Si layers samples. The thicknesses of the a-Si layers is the only varied parameter between the different samples. This thickness was controlled by the sputtering time of a-Si and have values of 6, 10, 13, 23 and 36 nm. Figure 5.1 displays the linear relation between the thickness of the sputtered a-Si layers and the sputtering time (dashed line). The open circles in this figure represents the actual samples in which the thickness has been determined from ellipsometry measurements.

Similar to the samples discussed in the previous chapter, a F2 prism with a refractive index of n =1.62 higher than the index of SiO_2 was attached to the sample with refractive index matching liquid (see Fig. 4.4). The attenuated total reflection spectra were obtained by illuminating the sample from the F2 prism side with a collimated beam of the white light from a halogen lamp. The incident plane wave was chosen to be p-polarized, i.e., with a transverse magnetic field (TM) with respect to the plane of incidence. By changing the angle of incidence onto the prism-SiO_2 interface, the resonant conditions for coupling to guided modes in the thin a-Si layer can be met, i.e., frequency and wave number matching between the incident and guided waves, leading to a strong reduction of the specular reflection. The reference measurement to determine the absolute reflectance of the samples were the measurements of the reflection of the same samples but with s-polarized incident light. The reflection of this polarization is close to 100% for angles of incidence larger that the critical angle for total internal reflection.

Fig. 5.2 shows the measured reflectance spectra as a function of the angle of incidence for five different a-Si samples of thickness (a) 6 nm, (b) 10 nm, (c) 13 nm, (d) 23 nm and (e) 36 nm. A resonance is resolved at larger angles that the critical angle for total internal reflection at the F2-SiO_2 interface, i.e., $\theta \simeq 64°$. A minimum of reflectance with typical values lower than 5% is observed for all the samples at the resonance. As the thickness of a-Si is increased, the resonance shifts from $\simeq$ 450 nm to $\simeq$ 700 nm. The angular width of the resonances also increases from about 0.2° to 4° of FWHM.

Calculations of the reflectance using the Fresnel coefficients for multilayers, as it was explained in section 2.3), are shown in Fig. 5.2(f)-(j). For these calculations we have used the layer thickness and the permittivities of a-Si obtained from ellipsometry measurements. Note that for the calculations we assume perfectly flat

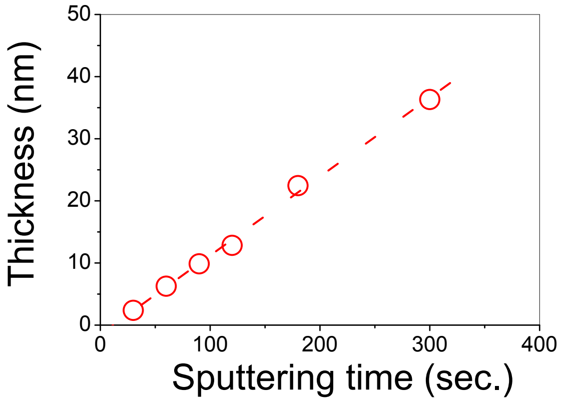

Figure 5.1: Nominal thickness of amorphous silicon layers as a function of the sputtering time (dashed line). The open circles correspond to samples in which the thickness is measured with ellipsometry.

layers of a-Si. Therefore, from the excellent agreement with the measurements, we can conclude that surface roughness is not relevant for the excitation of surface guided modes in a-Si.

The permittivity of a-Si presents an strong dispersion in the wavelength range

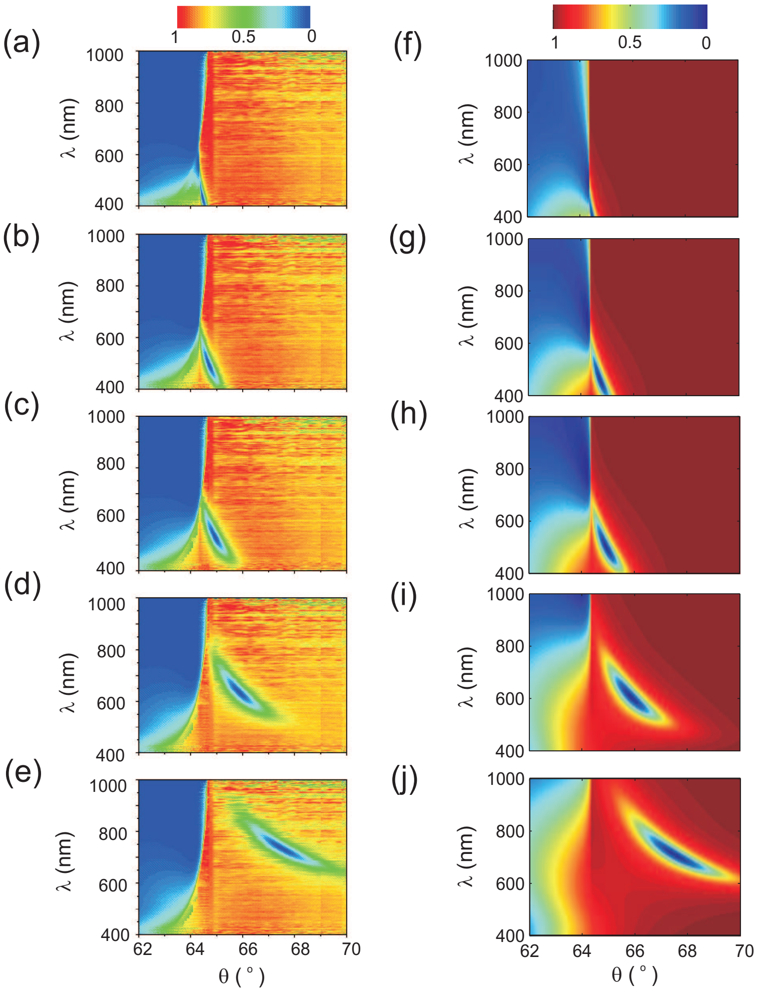

Figure 5.2: Reflectance measurements as a function of wavelength and angle of incidence of the multilayers formed by a F2 prism, a layer of silica with a thickness of 550 nm, a layer of a-Si with thickness of (a) 6, (b) 10, (c) 13 (d) 23 (e) 36 nm and a silica substrate. The calculated reflectance as a function of wavelength and angle of incidence for the corresponding multilayers samples with thickness of a-Si being (f) 6, (g) 10, (h) 13 (i) 23 (j) 36 nm.

of our experiments (see Fig. 4.3). For wavelengths longer than 600 nm the imaginary component of the permittivity is low. Absorption in a-Si increases as the the wavelength approaches the direct bandgap energy, i.e., $\lambda \simeq 350\,\text{nm}$, which leads to an increase of the value of the imaginary component of the permittivity. Therefore, the measurements of Fig. 5.2 illustrate the transition between TM_0 modes guided by layers of non- or weakly absorbing dielectrics to LRSPs guided by thin layers of strongly absorbing materials. There is a smooth transition between both regimes as we can appreciate in our measurements (see Fig. 5.2(a)-(e)) and as it was pointed out by Yang et al. theoretically in Ref. [56].

Figs. 5.3(a)-(e) display the measured reflectance spectra plotted as a function of the normalized frequency ,ω/c, and the real component of the wave number along the a-Si surface, k_{xr}, where $k_{xr} = \mathbf{k}_0 n_{\text{SiO}_2} \sin(\theta)$. For clarity, the reflectance is plotted using different scales for the different measurements. The white lines in these figures correspond to the light line in SiO_2 and the sharp bands of low reflectance correspond to the excitation of guided modes in the a-Si layers. In Figs. 5.3(f)-(j), we plot the calculations of the reflectance as a function of the normalized frequency and wave number k_{xr}.

The minima in reflection of Fig. 5.3 define the dispersion relation of the surface modes. Figure 5.4 displays these minima for the different layer thicknesses (see figure legend). The dispersion of guided modes on a-Si varies when the thickness of the thin film increases: The thicker the a-Si film, the larger becomes the difference between the wave number of the light line and guided more at each frequency. As it is shown in the next section, we can derive from the dispersion measurements the confinement of the electromagnetic field to the thin layer, the propagation length of the modes and their group velocity.

5.3 Surface modes characteristics

We have derived two characteristic lengths of the guided modes on a-Si layers. The first is the propagation length along the surface L_x and it is displayed in Fig. 5.5 as a function of wavelength. These values are obtained with the expression $L_x = 1/2\Delta k_{xr}$, where Δk_{xr} is the full width at half maximum of the measured resonances in reflectance. The value of L_x reaches a value of $10\,\mu\text{m}$ for the thinnest a-Si film at $\lambda = 500\,\text{nm}$ and decreases down to $2.5\,\mu\text{m}$ as the thicknesses of the a-Si film increases to 36 nm at $\lambda = 700\,\text{nm}$. In general, L_x is longer for thinner layers due to the exclusion of the electromagnetic field from the thin absorbing layer. The exclusion is associated with a longer decay of the field intensity into the surrounding dielectric. This confinement of the field to the thin layer determines the second

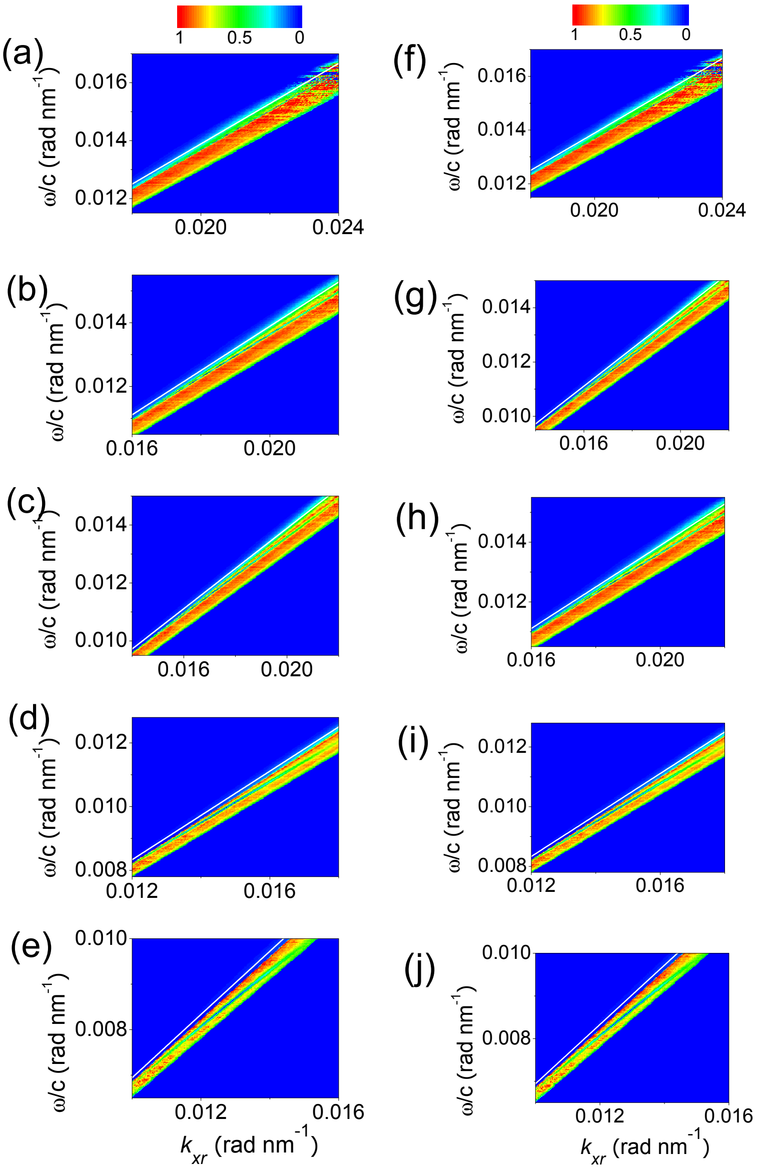

Figure 5.3: Reflectance measurements as a function of the frequency and the wave number k_{xr} parallel to the a-Si layers with thickness of (a) 6, (b) 10, (c) 13 (d) 23 (e) 36 nm. The calculated reflectances are plotted in (f) for 6 nm, (g) for 10 nm, (h) for 13 nm, (i) for 23 nm and (j) for 36 nm. The white line represents the light line in SiO_2.

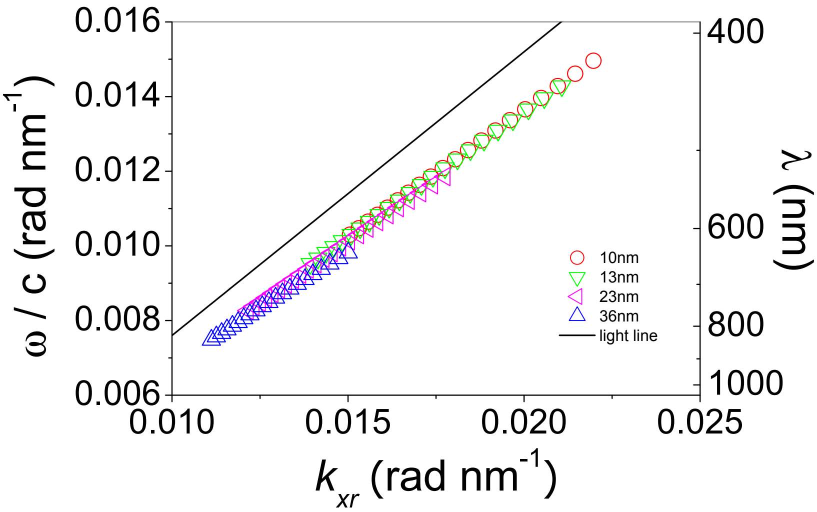

Figure 5.4: Experimentally determined dispersion relation of guided modes on a-Si layers with different thicknesses surrounded by SiO_2. The light line in SiO_2 is plotted by the black solid line.

characteristic length, L_y, which is defined as the $1/e$ intensity decay length of the electromagnetic field into the surrounding dielectric

$$L_y = \frac{1}{2Re\left(\sqrt{k_x^2 - \mathbf{k}_0^2 n_d}\right)}, \tag{5.1}$$

where $k_x = k_{xr} + ik_{xi}$ is the complex wave vector along the surfaces. The real component k_{xr} is obtained from the dispersion measurements of Fig. 5.4 and the imaginary component is given by $k_{xi} = 1/2L_x$. As can be appreciated by comparing Figs. 5.5 and 5.6, the decay length of the field intensity from the thin a-Si layer is correlated to the propagation length of the surface mode: The longer the propagation length is, the weaker becomes the field confinement in the normal y-direction, i.e., the longer L_y is. We note that the values of L_x determined from the experiments are significantly lower than the calculated values given in Table 4.1 in the previous chapter. The origin of this discrepancy can be found on the radiative losses into the prism inherent to the coupling technique used for the experiments. The calculations in the aforementioned table were done considering a thin a-Si slab surrounded by an infinitely thick dielectric into which no radiative losses take place.

From the dispersion measurements of Fig. 5.4 we can derive the group velocity

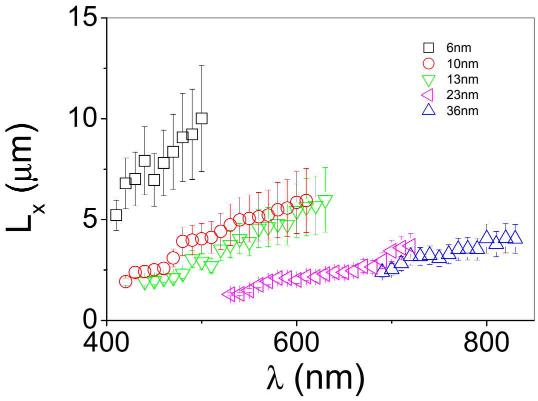

Figure 5.5: Propagation length L_x as a function of the wavelength for a-Si layers surrounded by SiO_2. The thickness of a-Si is 6 nm (squares), 10 nm (circles), 13 nm (down triangles), 23 nm (titled triangles) and 36 nm (up triangles).

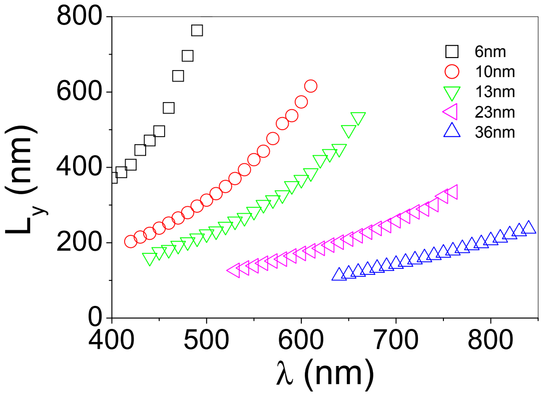

Figure 5.6: Decay length L_y plotted as a function of wavelength for a-Si layers surrounded by SiO_2. The thickness of a-Si is 6 nm (squares), 10 nm (circles), 13 nm (down triangles), 23 nm (titled triangles) and 36 nm (up triangles).

of the guided modes. This velocity is defined as

$$v_g = \partial\omega / \partial k_{xr} \; . \tag{5.2}$$

Figure 5.7 displays the group velocity normalized to the speed of light in vacuum as a function of the wavelength and the wave number k_{xr}. For the thinnest sample, the field is mainly distributed in SiO_2, leading a value of v_g close to that in this dielectric. For thicker samples the field penetrates more into the a-Si layer, which leads to a reduction of the v_g.

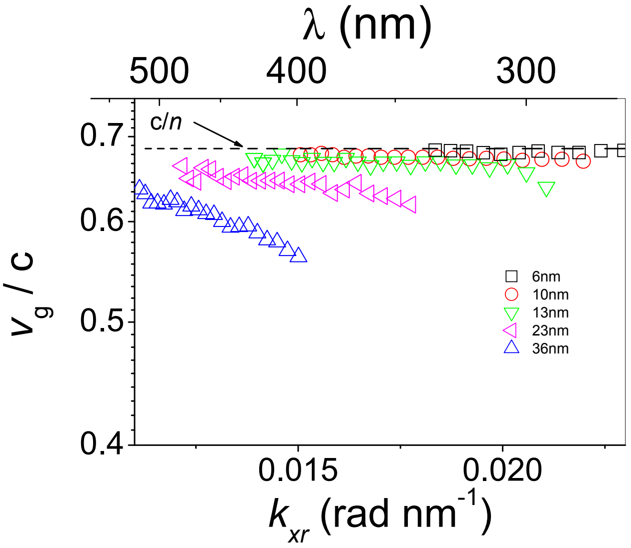

Figure 5.7: Group velocity normalized to the speed of light in vacuum as a function of the wave number k_{xr} and wavelength. The horizontal line is the normalized speed of light in silica.

5.4 Discussion

In section 3.3, we stated that long-range guided modes could be supported by thin layers of almost any material. These modes are named long-range surface exciton polariton when $\epsilon_r = 0$, $\epsilon_i \gg 0$, TM$_0$ when $\epsilon_r > 0$, $\epsilon_i = 0$, and long-range surface plasmon polaritons when $\epsilon_r < 0$, $\epsilon_i = 0$. More generally, long-range surface polaritons and TM$_0$ modes include modes supported by thin films of weakly absorbing materials. We also refer to long-range surface polaritons to modes in thin layer of strongly absorbing materials, i.e., materials with a significant imaginary component of the permittivity.

As it was indicated before [86–90], there is a smooth transition between TM$_0$ modes and LRSPs as the absorption in the thin layer is increased. This smooth transition can be appreciated in Figs. 5.2(a)-(e), where the resonance measured in reflection evolves between LRSPs and TM$_0$ mode as it moves from 400 nm to 700 nm.

In order to describe this evolution better, we have calculated the transverse and longitudinal electric E$_x$, E$_y$ and magnetic H$_z$ field components as a function of the cross section of the multilayer structures. Figs. 5.8(a)-(e) represent the three field components for the five guided modes supported by the different layers of

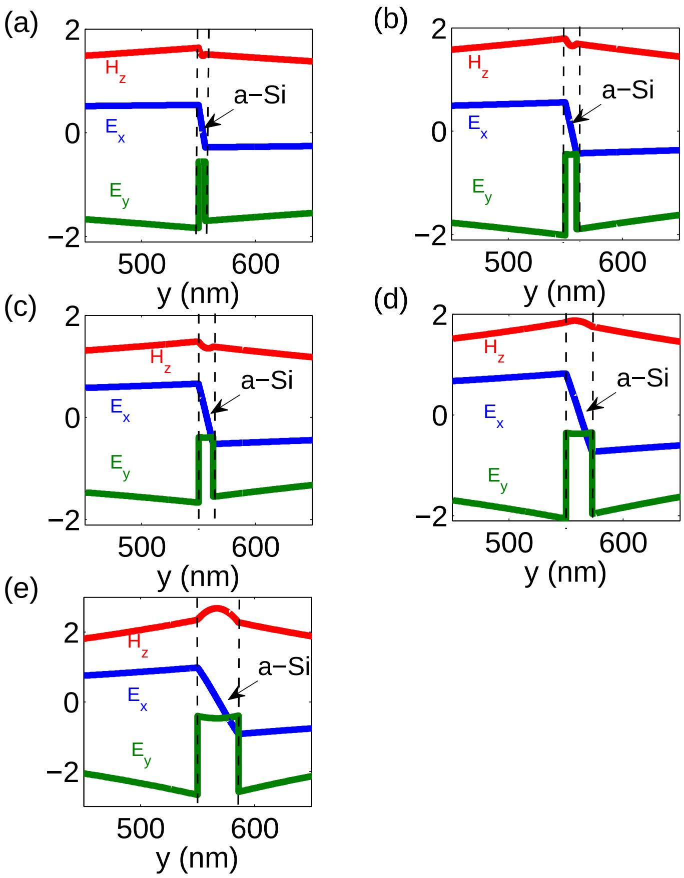

Figure 5.8: Transverse and longitudinal components of the electric and magnetic field of guided modes on thin layer of a-Si with a thickness of (a) 6nm, (b) 10nm, (c) 13nm, (d) 23nm, and (e) 36nm surrounded by SiO_2.

a-Si with different thicknesses. The calculations are done at $\lambda = 410\,\text{nm}$ for the a-Si layer of 6 nm, $\lambda = 450\,\text{nm}$ for the layer of 10 nm, $\lambda = 500\,\text{nm}$ for the layer of 13 nm, $\lambda = 600\,\text{nm}$ for the layer of 23 nm and $\lambda = 700\,\text{nm}$ for layer of 36 nm. The E_x components vanish inside the a-Si layer for all the wavelengths. The E_y components are symmetric with respect to the a-Si layers. The main difference between TM_0 modes in the thickest a-Si layers and the LRSPs in the thinnest layers can be found in the H_z component. A relative minimum of H_z inside the a-Si layer is found for the layer thickness of 6, 10 and 13 nm. This minimum is characteristic to long-range surface polaritons resulting from the coupling of surface polaritons in the opposite sides of the thin layer. On the other hand, a relative maximum of

H_z inside the a-Si layer is found for the modes on the 23 and 36 nm layers. This is a characteristic of TM_0 modes in weakly absorbing layers.

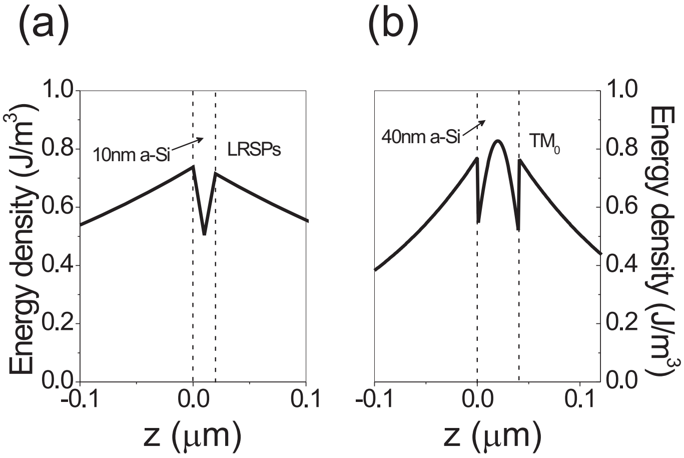

Figure 5.9: Electromagnetic energy density profiles plotted as a function of the cross section of a-Si waveguides embedded in silica, (a) corresponds to a layer thickness of 10 nm and $\lambda = 500$ nm, while (b) to a layer thickness of 40 nm and $\lambda = 700$ nm.

We have also calculated the electromagnetic energy density as a function of the cross section of the slab waveguide in the y direction

$$u_j = \frac{1}{2}(\epsilon_j \mathbf{E}^2 + \mathbf{H}^2), j = 1,2 \tag{5.3}$$

where ϵ_j is the permittivity in medium j, **E** and **H** are the total electric and magnetic fields. For the calculations we choose a thickness of the a-Si layer of 10 nm (Figure 5.9(a)) and 40 nm (Figure 5.9(b)), similar to the previous experiments. For the 10 nm layer, the calculation is done at $\lambda = 500$ nm, thus it corresponds to the case of LRSPs, while for the 40 nm layer the calculation is at $\lambda = 700$ nm, thus for a TM_0 mode. As it can be approximated in Figure 5.9(a), the energy density of the LRSPs mode is the highest at the interfaces. This energy density exhibits a minimum at the middle of the slab. Outside the slab, the energy density decays evanescently away from the interfaces. On the other hand, from Figure 5.9(b) we see that the energy density of the TM_0 mode exhibits a maximum at the center of the slab, which is the characteristic of a guided mode in dielectric slabs.

5.5 Conclusion

We have determined the dispersion of long-range guided modes in thin layers of a-Si by attenuated total internal reflectance measurements in layers with different thickness. The dispersion relation of LRSPs modes in the extreme thin film case ($d \approx 10\,\text{nm}$) are almost parallel to the light line. On the other hand, for ($\text{d} > 10\,\text{nm}$), the dispersion relation separates from the light line. Controlling the thickness of the thin absorbing layer allows to tailor the propagation length, the confinement of the field to the thin layer and the group velocity.

CHAPTER 6

LRSPS SENSORS BASED ON NANOMETRIC LAYERS OF STRONGLY ABSORBING MATERIALS

We demonstrate that strong optical absorption in layers with a thickness of only a few nanometers can be an advantage for increasing the sensitivity of surface polariton resonance SPR sensors. In particular, we demonstrate high sensitivity of a chalcogenide glass sensors to minute changes of the refractive index.

6.1 Introduction

Optical sensing based on surface plasmon polaritons is nowadays a broadly used technique for detecting small changes in the refractive index induced by analytes close to surfaces. These techniques have a high sensitivity associated to a strongly confined electromagnetic field close to the interface separating a metal from a non-absorbing dielectric. The field confinement allows for subwavelength optical detection [23, 91, 92]. A widely accepted characteristic of surface plasmon resonance sensors is that losses in the metal must be as low as possible to improve their sensitivity. Therefore, there is a small number of metals that is used for plasmonic sensing [93]. A recent development in SPR sensing is the use of ultrathin metallic layers (thinner than 50 nm) embedded in a homogeneous medium. These layers support long-range surface plasmon polaritons [14]. These surface modes suffer low loss due to the symmetry of the field distribution with respect to the nanometric film, which reduces the electromagnetic energy stored in the lossy metal [26, 43, 46]. Since the spectral width of surface plasmon resonances is proportional to the losses, a much sharper resonance associated to long-range SPPs, compared to SPPs resonances, is observed in attenuated total internal reflection measurements [44]. These sharp resonances can improve the performance of optical sensors by increasing the detection resolution and the intrinsic sensitivity [31, 45, 94]. Long-range SPPs have a longer decay length into the surrounding dielectric than SPPs, which arises from the coupling between the SPPs on opposite sides of the thin layer. Moreover, the coupling strength can be tuned by varying the thickness of the metallic film, providing an easy tool to optimize the spatial overlap between the evanescent surface mode and the analyte under investigation. This optimization can increase significantly the sensitivity of surface plasmon resonance sensors [93, 95]. As we have shown in the previous chapters, it is possible to excite long-range surface modes in ultra-thin layers of strongly absorbing materials, which are similar to long-range SPPs. Therefore, there is not a fundamental nor a practical reason to limit long-range surface polariton sensing to metals.

In this chapter, we investigate LRSPs modes supported by thin layers of chalcogenide glasses, in particular amorphous $Ge_{17}Sb_{76}Te_7$ (a-GST), and demonstrate their high intrinsic sensitivity to small changes in the refractive index of the surrounding media. Chalcogenide glasses have two phases, a metallic (crystalline) and a dielectric (amorphous) phase. They are inexpensive, present a strong optical absorption in the visible [96], are chemically stable and can be deposited in layers with nanometer accuracy [79]. These characteristics makes chalcogenide glasses an excellent alternative to noble metals in sensing applications.

6.2 Experimental

The investigated sample is a multilayer structure (see inset of Fig. 6.1(a)) formed by a Schott F2 glass substrate with a refractive index of 1.62 in the visible, a layer of nanoporous silica (NPS) [97] with a thickness of 430 nm and a refractive index of 1.35 ± 0.01 between 300 and 700 nm, and a film of a-GST with a thickness of 20 nm. The multilayer sample was prepared as follows: First a nanoporous SiOC:H (NPS) layer was spin coated onto a Schott F2 glass substrate. The NPS film was subsequently baked on a hotplate at 200°C for 10 minutes. This process was repeated three times to reach a total thickness of 430 nm. The NPS film was additionally baked at 400°C for 30 minutes to increase its porosity and thereby decrease its refractive index to about 1.35. An a-GST thin film with a thickness of 20 nm was sputtered onto the NPS layer. The permittivity of NPS and GST layers were determined from ellipsometry measurements. For a-GST and c-GST layer, these values are similar to Fig. 3.1. The absorption coefficient α of a-GST is plotted against wavelength in Fig. 6.1(a). This coefficient is larger than $10^5\,\mathrm{cm}^{-1}$ for the whole visible spectrum.

The sample was attached to a cell to allow the flow of water to the a-GST thin-film assembly. The excitation of LRSPs was achieved by using the attenuated total internal reflection method in the Kretschmann-Raether configuration. A schematic representation of this technique is displayed in Fig. 6.1(b) and described in detail in section 2.3. LRSPs arise from the coupling between surface polaritons at the opposite sides of the thin film. This coupling is only possible when the energy and wavenumber of the surface polaritons are similar, i.e., when the dielectric media close to the thin film on both interfaces have similar refractive index. In order to obtain this symmetric environment, the porosity of the NPS layer was tuned to match its refractive index to that of water. Figure 6.2 shows the dielectric permittivity of NPS layer. These values have been determined by ellipsometry measurements. The F2 glass substrate was optically matched to the prism with refractive index matching liquid (Cargille, Ltd.). A collimated optical beam was incident onto the F2 glass prism and refracted to the interface between the sample substrate and the NPS layer at an angle larger than the total internal reflection angle. The evanescently transmitted amplitude into the NPS layer can couple to LRSPs in the a-GST film at the resonant angles and frequencies at which the energy and wavenumber parallel to the thin film are conserved. The coupling to LRSPs is measured by detecting a reduction of the specular reflectance at the F2 glass-NPS interface. The reference measurement was obtained by measuring the total internal reflection of s-polarized light. This reflection is close to 1 at larger angles than the critical angle. The experiments were done with a computer

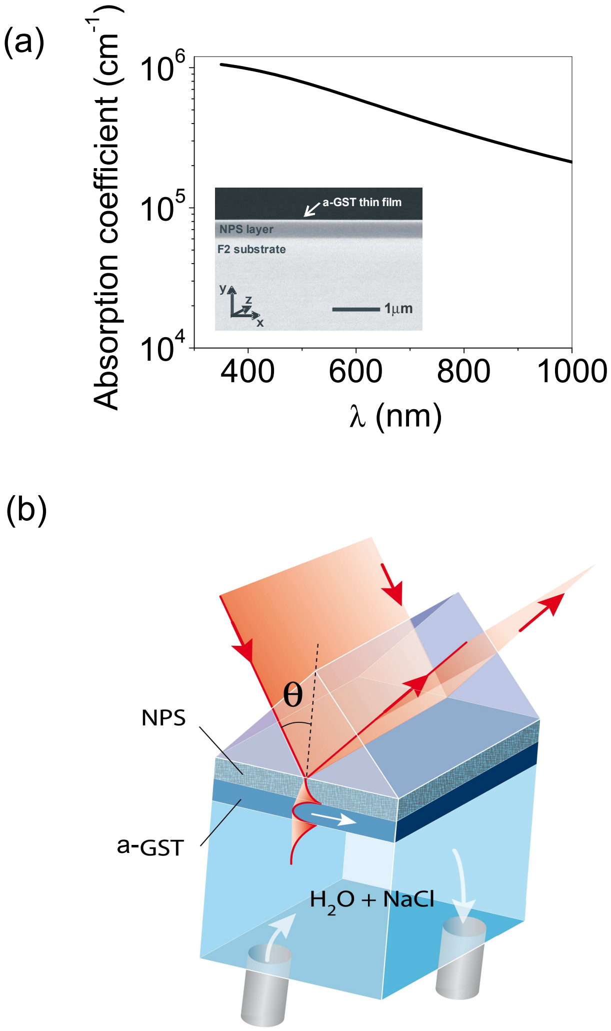

Figure 6.1: (a), Absorption coefficient of a-GST as a function of the wavelength. The inset is a scanning electron microscope side view image of a sample: A multilayer structure consisting of an a-GST thin film, a nanoporous silica NPS layer, and a F2 glass substrate. (b), Schematic representation of a long-range surface polariton sensor. The incident plane wave in the prism is totally internally reflected at the prism-NPS interface. The evanescent transmitted field can couple to LRSPs. At the resonance angle and frequency the coupling is apparent by a strong reduction of the total internal reflection.

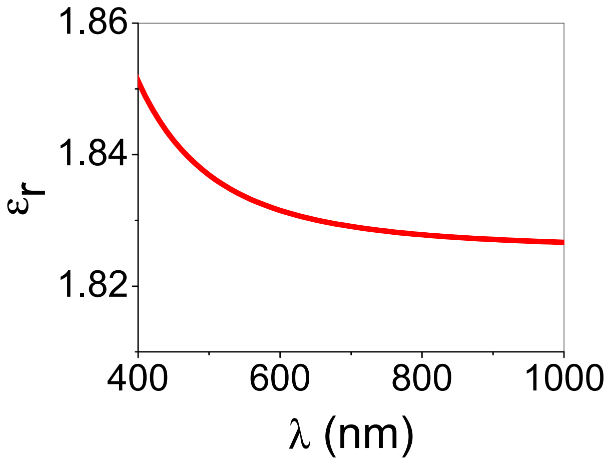

Figure 6.2: Real component of permittivity of NPS (the imaginary component is negligible).

controlled rotation stage set-up that allowed the simultaneous rotation of sample and detector. The angular resolution of the setup is 0.04°, which is determined by the divergence of the optical beam. We have used a diode laser emitting at a wavelength $\lambda = 530\,\text{nm}$ as light source, a Si-photodiode as detector and lock-in detection to measure the specular reflection.

Surface polaritons can be excited only with p-polarized light, therefore, the polarization of the incident beam was accordingly set with a polarizer. Figure 6.3a illustrates the coupling of incident light to LRSPs. This figure displays a calculation of the magnetic field amplitude (see section 2.2) in a sample with the parameters described above and water at the exposed side of the a-GST film. A p-polarized plane wave is incident at an angle 56.6°. This angle corresponds to the angle for resonant coupling to LRSPs. The maximum field amplitude is at the surface of the a-GST film, i.e., at $z = 0$ and $z = -20\,\text{nm}$, and the field decays exponentially from these layers into the surrounding dielectrics (NPS and water). This exponential decay is also illustrated in Fig. 6.3(b), where the square of the magnetic field amplitude of the LRSPs at $x = 0\,\text{nm}$ is plotted against the distance to the a-GST thin film.

To determine the sensitivity of LRSPs to small changes of the refractive index in the surrounding medium, we have performed attenuated total reflectance measurements at $\lambda = 530\,\text{nm}$ by filling the flow cell with a solution of purified water and NaCl [98]. Figure 6.4 shows the reflectance as a function of the incident angle

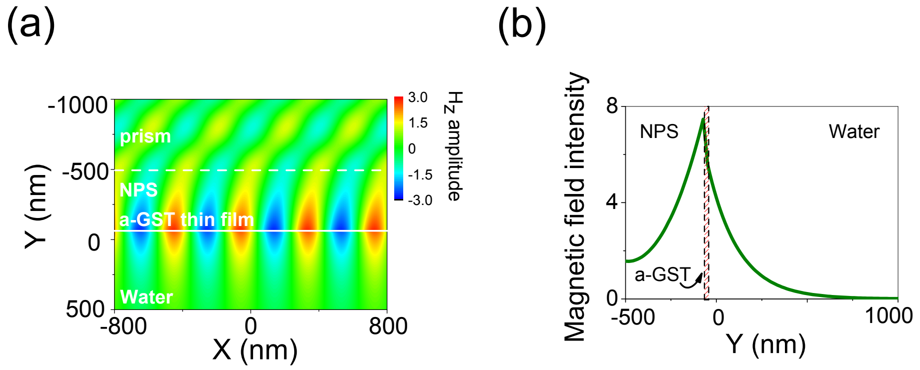

Figure 6.3: (a), Calculation of the magnetic field amplitude for p-polarized light (λ = 530 nm) incident at an angle of 56.6° with respect to the sample normal onto the multilayer shown in the inset of Fig 6.1a. The a-GST film is exposed to water. The incident wave couples to LRSPs on the a-GST layer at this wavelength and angle. The maximum field amplitude is at the interfaces of the a-GST film.(b), displays a cut at $x = 0$ of the magnetic field intensity of the LRSP in the multilayer structure. The field intensity decays exponentially from the a-GST interface into the surrounding media.

for p-polarized light. The reduction of the total internal reflectance corresponds to the excitation of LRSPs modes in the a-GST thin film. The LRSPs resonance shifts to larger angles and broadens when the concentration of NaCl increases. The measurements were fitted with exact calculations of the reflectance based on Fresnel's equations for the multilayer structure (see section 2.2). These fits are shown in Fig. 6.5(a)-(d). The fitting parameters of the attenuated total reflection measurements are the thickness of the a-GST layer, which was kept constant for all the fits, and the refractive index of the solution. All other parameters, i.e., index of refraction of the different materials and thickness of the NPS layer, are known from ellipsometry measurements and scanning electron microscope images. The thickness of the a-GST film obtained from the fits is 19.5 ± 0.5 nm. This value, within the resolution of the SEM images, is in agreement with the electron microscopy results.

The resonance angle θ, defined as the angle of the minimum of reflectance, and resonance width $\Delta\theta$, defined as the width of the resonance at a reflectance of 50%, are plotted as a function of the refractive index of the surrounding solutions in Fig. 6.6 with open blue circles and triangles respectively. The solid lines in this figure correspond to exact calculations for the multilayer structure. The resonance shifts to larger angles as the refractive index in the aqueous solution increases due

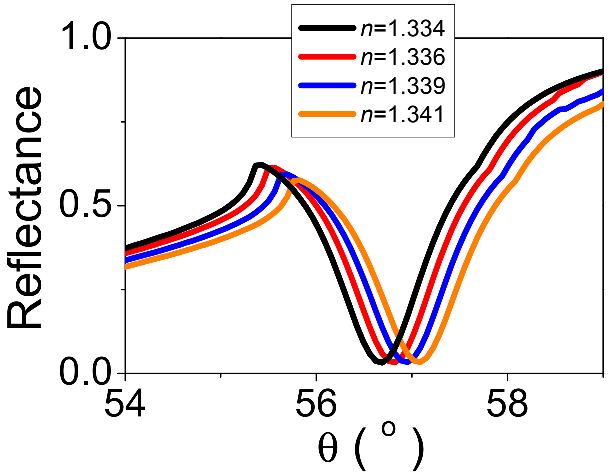

Figure 6.4: Attenuated total reflectance measurements at $\lambda = 530\,\mathrm{nm}$ of the multilayer shown in the inset of Fig. 6.1a, exposed to various solutions with different refractive indices.

to the modification of the phase matching condition and of the coupling between the incident plane wave and the LRSPs. The increase in resonance width is a consequence of the difference in refractive index between the NPS layer and the water solution. This difference weakens the coupling between surface polaritons at the opposite interfaces of the a-GST film, leading to an increase of the penetration of the electromagnetic field into the absorbing a-GST layer and, consequently, to a stronger absorption. The measured sensing figure of merit [99–102]

$$FOM = \frac{\delta\theta}{\delta n_{water}} \frac{1}{\Delta\theta}\,, \tag{6.1}$$

for this particular sample and at $\lambda = 530$ nm is 50. In this expression, n_{water} is the refractive index of the sensed medium, i.e., water and $\delta\theta$ is the shift of the resonance angle due to a change in refractive index δn_{water}. It is worth to mention that this FOM is almost four times higher than the FOM of previously reported SPR sensors operating at $\lambda = 632$ nm [19], which highlights the relevance of nanometric layers supporting LRSPs for optical sensing.

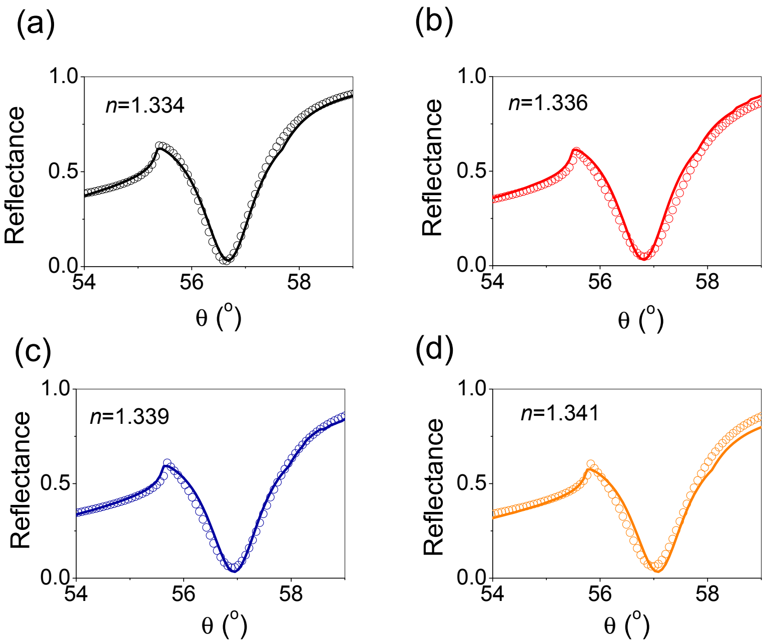

Figure 6.5: Fits (open circles) to the measurements (solid lines) of the attenuated total reflection of an a-GST layer exposed to solutions of NaCl in water with refractive indices of (a), n=1.334 (b), n=1.336 (c), n=1.339 (d), n=1.341.

6.3 Mode calculation

To compare the intrinsic properties of different surface modes for sensing, we have calculated the modification of their complex wave number, $k_x = k_{xr} + ik_{xi}$ (see section 2.2), due to changes in the refractive index of the surrounding medium. In contrast to the FOM given above, the effect of the method used to couple the incident light to surface polaritons is not considered in these calculations, facilitating a general comparison of surface modes for sensing. Two parameters should be taken into account in order to characterize the performance of the optical sensors: the intrinsic sensitivity IS, and the decay length $\mathrm{L_y}$ [93] of the evanescent field in the surrounding medium. The intrinsic sensitivity is defined as the derivative of the real part of the wave vector with respect to the refractive index of the surrounding medium normalized by the imaginary part of the wave vector,

$$IS = \frac{\delta k_{xr}}{\delta n_{water}} \frac{1}{k_{xi}} . \tag{6.2}$$

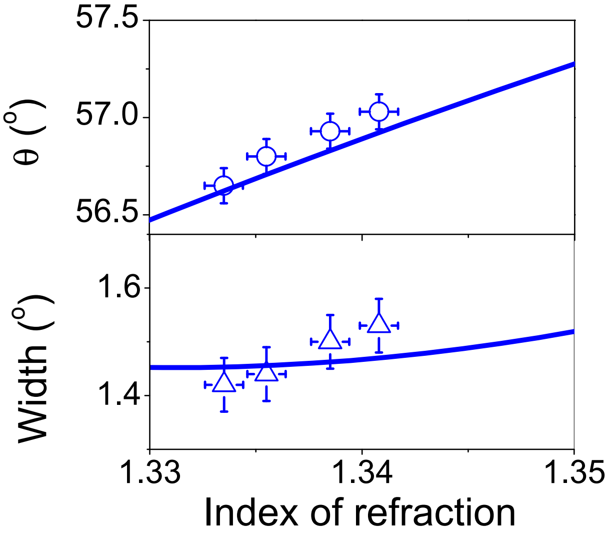

Figure 6.6: Measured (blue symbols) and calculated (blue lines) resonance angles and widths as a function of the refractive index of the solution.

The decay length $\mathrm{L_y}$ defines the dimensions of the surrounding medium in contact with the thin film that influence the LRSPs resonance. This length is given by

$$\mathrm{L_y} = \frac{1}{2Re\left(\sqrt{k_x^2 - \mathbf{k}_0^2 n_{water}^2}\right)}, \tag{6.3}$$

where $\mathbf{k}_0$ is the vacuum wave number. The propagation constant can be obtained from the modal calculation as we discussed previously in section 2.2.

The IS and $\mathrm{L_y}$ of LRSPs supported by a thin film of a material with complex permittivity $\epsilon = \epsilon_\mathrm{r} + i\epsilon_\mathrm{i}$ surrounded by a dielectric with a refractive index of 1.33 are plotted as a function of ϵ_r and ϵ_i in Figs. 6.7(a) and (b) respectively. For these calculations we consider a ratio of $d = 0.038\lambda$. To obtain a good contrast on the figures, we have fixed the maximum of the color scale of Fig. 6.7(a) at 500, and of Fig. 6.7(b) at 0.6. The symbols display the values of IS and $\mathrm{L_y}$ for a thin film of gold (blue squares), a-GST (red circles) and crystalline c-GST (cyan triangles) for wavelengths varying from 400 nm to 650 nm in steps of 19 nm. These values of IS and $\mathrm{L_y}$ at different wavelengths correspond to layers with a thickness $d = 0.038\lambda$, i.e., the same d/λ value used for the mode calculations. For these calculations, we use the permittivity of Au given in Ref. [65] and the measured permittivities for phase change materials. Note that although we have performed measurements of a-GST, it is possible to change the phase of the material to crystalline by heating it (as we did in chapter 3). [79] Therefore, LRSPs sensors of c-GST are feasible.

It is interesting to discuss the different regions in Fig. 6.7. The white areas close to the origin correspond to values of the permittivity for which thin films can not support guided modes. On the right-bottom part of the graphs we have layers of weakly absorbing dielectrics ($\epsilon_r > 0, \epsilon_i \ll \epsilon_r$) that support modes that are guided by total internal reflection. The fundamental mode provides a large IS due to a very narrow resonance that results from the weak absorption in the layer. However, the evanescent field decays a long distance in the surrounding medium, i.e., large $\mathrm{L_y}$, which limits the applicability of thin layers of non-absorbing dielectrics for the detection of small molecules bounded to the surface. On the left-bottom part of Figs. 6.7a and b there is the region of low loss metals that support long-range surface plasmon polaritons, i.e., $\epsilon_r < 0, \epsilon_i \ll |\epsilon_r|$. Note that long-range surface plasmon polaritons combine a large IS and a very good confinement ($L_{\mathrm{y}}/\lambda \ll 1$). However, there is a very limited choice of materials with a permittivity that fullfills these characteristics [91, 103]. In the case of Au (blue squares), the IS is high at long wavelengths, but it decreases rapidly below $\lambda = 550\,\mathrm{nm}$. Besides the limits of weakly absorbing dielectrics and low loss metals, there is the wide region of permittivities that characterize LRSPs, i.e., $\epsilon_i \gtrsim |\epsilon_r|$.

We can notice in Fig. 6.7(a) that chalcogenide thin films have a better IS than gold at shorter wavelengths than $\lambda = 550\,\mathrm{nm}$. In the case of a dielectric ($\epsilon_r > 0$), L_y is first reduced as ϵ_i increases, but increases for large ϵ_i. For metals ($\epsilon_r < 0$), $\mathrm{L_y}$ increases as ϵ_i increases. The coupling strength between surface polaritons at the opposite sides of the thin layer depends on its thickness. Therefore, a change in this thickness will have an impact on the IS and $\mathrm{L_y}$. The dependency of these parameters on the thickness of the layer from 5 to 40 nm and at $\lambda = 500\,\mathrm{nm}$ are illustrated in Figs. 6.8(a) and (b) for Au (blue-dotted curve), a-GST (red-solid curve) and c-GST (green-dashed line). The thinnest layer of 5 nm for these calculations is motivated by the possibility of depositing homogeneous films of chalcogenide glasses with this thickness [79]. However, we have to point out that metal films with this thickness are challenging to fabricate due to the formation of discontinuous islands below a critical thickness [43]. This characteristic constitutes an important advantage of chalcogenide glasses over metals for long-range surface polariton sensing. The IS is improved and $\mathrm{L_y}$ increases as the thickness of the thin layer decreases. This behavior is due to the stronger coupling of surface polaritons at opposite interfaces, which leads to a reduction of the mode intensity in the thin layer of lossy material and longer extension of this intensity in the surrounding medium. In Fig. 6.8(c) and (d) we have plotted the IS and $\mathrm{L_y}$ of a-GST and c-GST normalized by the respective values of Au as a function of the thin film thickness

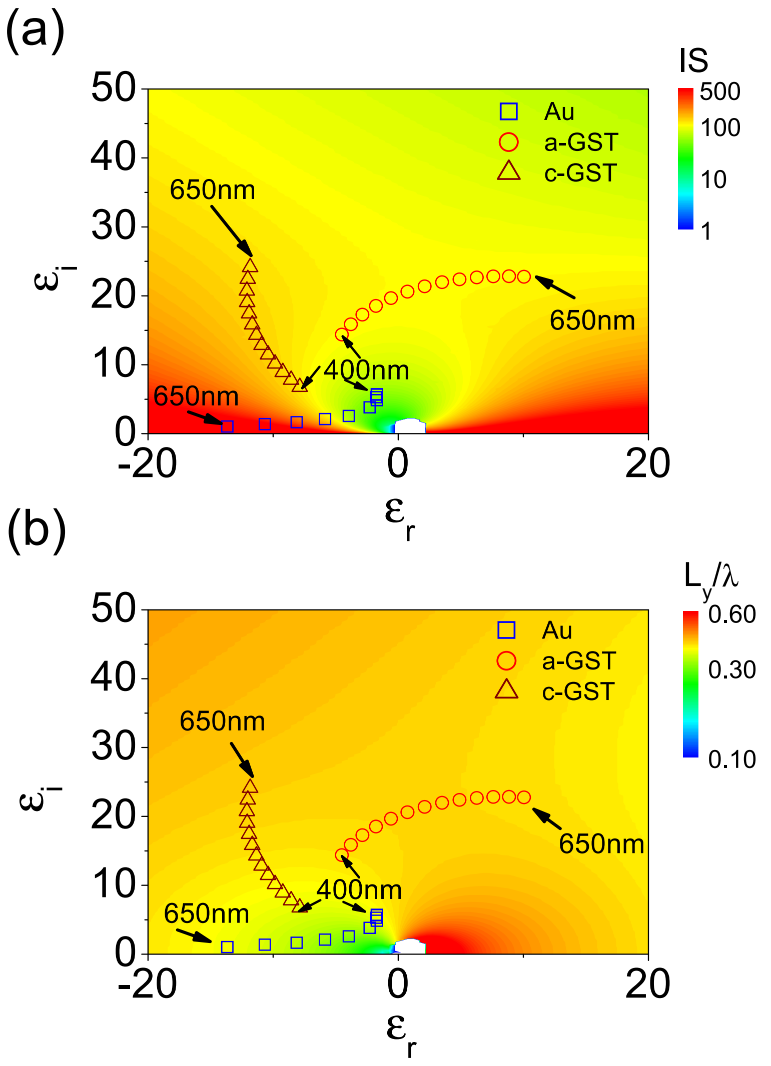

Figure 6.7: (a), Calculated intrinsic sensitivity and (b), decay length normalized to the wavelength of LRSPs in a thin film of thickness d = 20 nm and at λ = 530 nm, plotted as a function of the real and imaginary components of the permittivity of the thin film. The surrounding medium has a refractive index of 1.33. The open symbols indicate the permittivity of Au (squares), a-GST (circles) and c-GST (triangles) at different wavelengths between 400 and 650 nm. The IS and L_y/λ values indicated by the symbols correspond to layers with a thickness-to-wavelength ratio equal to the ratio in the calculations displayed by the contour plots, i.e., $d/\lambda = 0.038$.

for $\lambda = 500\,\text{nm}$. This is the wavelength at which the improvement of the IS by GST films compared to Au is maximum. A four-fold improvement of the IS can be achieved by using GST films with a thickness below 10 nm, while maintaining similar confinement of the field to the layer. We stress that the fabrication of films of Au with a thickness of 10 nm or thinner is very challenging. Therefore, the maximum IS attainable with GST films may be more than one order of magnitude larger than the maximun IS attainable with thin metal films. Furthermore, the decay length can be adjusted by the thickness of the film. This tuneability of $\mathrm{L_y}$ will allow the optimization of the sensitivity to analytes with different size by improving the spatial overlap of the electromagnetic field with the analyte.

In order to compare these characteristic parameters of Au, a-GST and c-GST at different wavelengths in the visible, we plot in Fig. 6.9(a) the intrinsic sensitivities of a-GST (red solid curve), c-GST (green dashed curve) and gold (blue dotted curve). Figure 6.9(b) displays $\mathrm{L_y}$ of a-GST (red solid curve) and c-GST (green dashed curve) and Au (blue dotted curve) as a function of λ in the range 400 to 630 nm. The intrinsic sensitivities and decay lengths of a-GST and c-GST normalized by that of Au are displayed in Fig. 6.9(c),(d) with a solid and dashed curve respectively . These curves have been obtained for layers with a thickness of 20 nm, i.e., the thickness of the layer used in the experiments. The upper wavelength limit used in the calculations represents the wavelength typically used in Au surface plasmon resonance systems. At this wavelength, Au sensors combine a high intrinsic sensitivity and a good field confinement. The IS of chalcogenide layers with a thickness of 20 nm is ~ 5.5 times lower than for gold at 630 nm. However, this IS ratio between chalcogenide layers and Au increases significantly as the wavelength is reduced. At 500 nm, the IS of a-GST is 2.4 times better than that of Au and for c-GST is 3.2 times better. As the wavelength is reduced also L_y decreases from 270 nm in the case of Au at $\lambda = 630\,\text{nm}$ to about 190 nm for the chalcogenide glasses at $\lambda = 500\,\text{nm}$. This reduction of L_y is relevant for the detection of small molecules bounded to the surface of the thin layer.

It is worth to mention that in the limit of very thin film [55], i.e., when the thickness is much smaller than the penetration of the field in the film, the IS increases linearly with ϵ_i. This behavior can be appreciated in Fig. 6.7(a), where for a layer with a thickness of 20 nm and as long as $\epsilon_i < 30$, the IS is improved when ϵ_i increases, i.e., when the optical loss in the thin film increases. This may be seen as a surprising result, which was discussed in chapter 3 and can be understood as follows: the electric field in the thin film is reduced when the optical loss increases due to the coupling and interference of surface polaritons at the opposite side of the layer [55]. This reduction of the field minimizes the losses of LRSPs, narrowing the resonance and improving the IS.

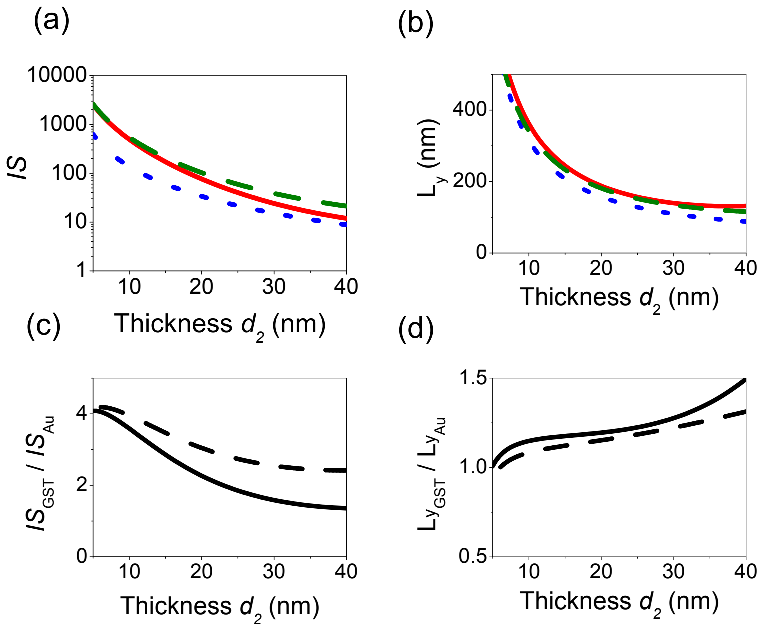

Figure 6.8: (a), Calculated intrinsic sensitivity and (b), decay length of LRSPs at λ =500 nm for a film of Au (dotted curve), c-GST (dashed curve) and a-GST (solid line) as a function of the thickness of the film. (c), Intrinsic sensitivity and (d), decay length ratio at λ =500 nm between a film of a-GST (c-GST) and Au, solid (dashed) curves, as a function of the thickness of the film. The thin film is surrounded by a medium with a refractive index of 1.33.

The complex wave vector of LRSPs in an asymmetric dielectric medium in the thin film limit can be approximated to [56]

$$k_{xr} \simeq \mathbf{k}_0\sqrt{\epsilon_{\mathrm{NPS}}}\left[1+\frac{(\epsilon_r^2+\epsilon_i^2-\epsilon_{\mathrm{NPS}}\epsilon_r)^2(A-B)^2-\epsilon_{\mathrm{NPS}}^2\epsilon_i^2(A+B)^2}{2\epsilon_{\mathrm{NPS}}\epsilon_{\mathrm{water}}^4(\epsilon_r^2+\epsilon_i^2)^2\left[(\epsilon_{\mathrm{NPS}}-\epsilon_r)^2+\epsilon_i^2\right]^2}\left(\frac{\pi d_2}{\lambda}\right)^2\right] \tag{6.4}$$

and

$$k_{xi} \simeq \mathbf{k}_0\sqrt{\epsilon_{\mathrm{NPS}}}\frac{\epsilon_i(\epsilon_r^2+\epsilon_i^2-\epsilon_{\mathrm{NPS}}\epsilon_r)(A^2-B^2)}{\epsilon_{\mathrm{water}}^4(\epsilon_r^2+\epsilon_i^2)^2\left[(\epsilon_{\mathrm{NPS}}-\epsilon_r)^2+\epsilon_i^2\right]^2}\left(\frac{\pi d_2}{\lambda}\right)^2, \tag{6.5}$$

where

$$A = \epsilon_{\mathrm{NPS}}\epsilon_{\mathrm{water}}^2\left[(\epsilon_{\mathrm{NPS}}-\epsilon_r)^2+\epsilon_i^2\right], \tag{6.6}$$

$$B = \frac{\epsilon_{\mathrm{NPS}}(\epsilon_{\mathrm{NPS}}-\epsilon_{\mathrm{water}})(\epsilon_r^2+\epsilon_i^2)}{4\left(\frac{\pi d_2}{\lambda}\right)^2}, \tag{6.7}$$

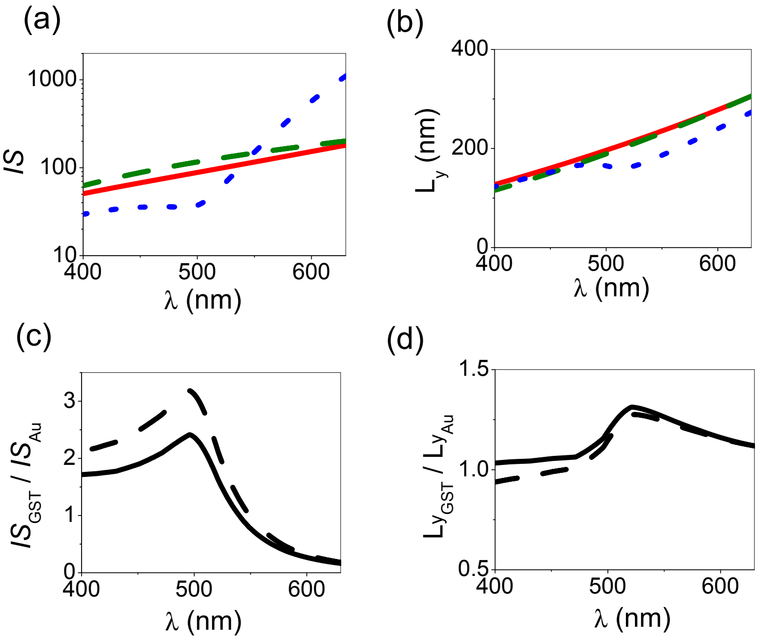

Figure 6.9: (a), Calculated intrinsic sensitivity and (b), decay length of LRSPs for a film with a thickness *d* of 20 nm of Au (dotted curve), c-GST (dashed curve) and a-GST (solid line) as a function of the wavelength. Intrinsic sensitivity (c), and decay length (d), ratio between a film of a-GST (c-GST) and Au, solid (dashed) curves, as a function of the wavlength. For all the calculations, the thin film is surrounded by a medium with a refractive index of 1.33.

where $\epsilon_{\text{NPS}} and \epsilon_{\text{water}}$ are the permittivities of nanoporous silica and water respectively. The derivative of k_{xr} has a rather simple expression, if we assume the same permittivities for NPS and water,

$$\left[\frac{\delta k_{xr}}{\delta n_{\text{water}}}\right]_{\epsilon_{NPS}=\epsilon_{\text{water}}} \simeq \frac{\mathbf{k}_0}{2}, \tag{6.8}$$

and the IS is given by

$$IS = \left[\frac{\delta k_{xr}}{\delta n_{\text{water}}}\frac{1}{k_{xi}}\right]_{\epsilon_{NPS}=\epsilon_{\text{water}}} \simeq \frac{1}{2n_{\text{water}}^5}\left(\frac{\lambda}{\pi d_2}\right)^2 \frac{(\epsilon_r^2+\epsilon_i^2)^2}{\epsilon_i(\epsilon_i^2+\epsilon_r(\epsilon_r-n_{\text{water}}^2))}. \tag{6.9}$$

In this limit and when $\epsilon_i \gg |\epsilon_r|$, the IS can be approximated by

$$IS \simeq \frac{\epsilon_i}{2n_{\text{water}}^5}\left(\frac{\lambda}{\pi d_2}\right)^2. \tag{6.10}$$

6.4 Conclusion

In conclusion, We have demonstrated that strong optical absorption in materials can be beneficial to improve the sensitivity of surface polariton sensors. In particular, we have shown that long-range surface polaritons supported by nanometric films of strongly absorbing chalcogenide glasses can be used as sensitive probes to changes in the refractive index of the surrounding medium. Our results open a new range of possibilities for optical sensing using other substrates than noble metals that are CMOS compatible.

CHAPTER 7

COUPLED LRSPS IN A MULTILAYER OF AMORPHOUS SILICON

We demonstrate the excitation of coupled long-range surface polaritons (LRSPs) in multiple layers of amorphous silicon (a-Si). This excitation is achieved by momentum matching of the incident plane wave to the surface modes through total internal reflection. Calculations of the electric field amplitude around the thin silicon layers reveal that this field has local maxima at the a-Si interfaces, decreasing rapidly inside the a-Si layers. This condition is required to achieve the long-range guiding character of these modes. The different symmetry of the field between the two thin Si layers for the different resonances reveal the mutual coupling LRSPs in the multilayered structure.

7.1 Introduction

As we have discussed in the previous chapters, a film of almost any material embedded in a dielectric environment can guide electromagnetic radiation if it is sufficiently thin [56]. The most common waveguide consists of a dielectric layer with a higher index of refraction than the surrounding. Thin layers of metal support long-range surface plasmon polaritons [43], which are guided modes arising from the coupling of surface plasmon polaritons at the opposite sides of the thin film. These modes have smaller propagation length than the guided modes in lossless dielectric waveguides, but exhibit a larger confinement of the electromagnetic field to the waveguide. At first sight, very lossy dielectrics seem incompatible with guiding radiation over distances of many wavelengths. However, guided modes can be supported in thin layers of strongly absorbing materials [30, 55, 57, 64]. These waves are called long-range surface exciton polaritons if the real part of the permittivity of the material forming the waveguide is zero [55]. More generally, they are called long-range surface polaritons (LRSPs) if the real part of the permittivity does not vanishes [30]. LRSPs supported by ultra-thin films of absorbing materials can have a propagation length of several tens to hundreds of wavelengths and a subwavelength confinement of the electromagnetic field to the surface [30]. The electromagnetic field distribution of these modes is similar to long-range surface plasmon polaritons in metals, with a maximum field at the interfaces of the thin film that decays exponentially away from these interfaces. The field is mainly concentrated in the lossless dielectric surrounding the absorbing layer, which explains the long propagation lengths of long-range surface modes.

In this chapter, we present the first demonstration of guided long-range surface polaritons on multiple layers of absorbing materials. In particular, we have measured the excitation of these modes in the visible in a multilayer structure composed of two thin films of amorphous silicon (a-Si) embedded in silica. This system presents two distinct resonances that can be associated to the coupled LRSPs in the two adjacent a-Si layers. As it was discussed in chapter 5, adjusting the thicknesses of the different layers allows the control of the dispersion of the resonances [30]. We have chosen the parameters that result in an efficient excitation of multiple LRSPs at the same wavelength. It is worth to mention that similar multilayer structures formed by metallic thin films supporting multiple long-range surface plasmon polariton have been proposed and vertical couplers have been demonstrated [104–108]. In contrast to these previous works, we demonstrate here the vertical coupling of LRSPs supported by multilayers of a-Si.

7.2 Experimental

7.2.1 Setup

A schematic representation of the experimental setup is depicted in Fig. 7.1(a). The sample is formed by the following multilayer structure: Silica (215 nm) / a-Si (25.5 nm) / silica (485 nm) / a-Si (21.5 nm) / silica substrate. The sample was prepared by sputtering a-Si on a silica substrate at a rate of 1.5 nm/s, followed by sputtering 485 nm of silica in the same machine at a rate of 5 nm/s. The upper a-Si layer of 25.5 nm and silica layer of 215 nm were sputtered in a similar way as the previous ones. A scanning electron microscope image of the cross section of the sample is given in Fig. 7.1(b). The multilayer is hold on one side of a F2 glass prism by the capillary forces exerted by a liquid (not shown in Fig. 7.1(b)) matching the refractive index of the prism, i.e., n=1.61. A collimated white light beam from an halogen lamp was incident onto the prism-silica interface. The high refractive index of the prism allows for momentum matching of the evanescently transmitted amplitude through the prism-silica interface for angles of incidence larger than the total internal reflection angle to the LRSPs on the multilayer structure.

7.2.2 Measurements

We have measured the reflectance spectrum at the F2-silica interface with a fiber-coupled spectrometer (Ocean Optics USB2000) by scanning the angle of incidence and the detection fiber of the spectrometer with a set of motorized rotation stages. Figure 7.2(a) displays the measured reflectance as a function of the angle of incidence onto the prism-silica interface and the wavelength. The incident beam was set to be p-polarized. The critical angle for total internal reflection at the prism-

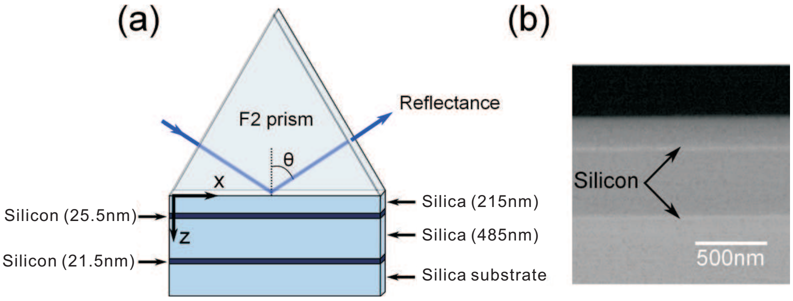

Figure 7.1: (a) Schematic representation of the setup used for the attenuated total reflection measurements. (b) Scanning electron microscope side view image of an a-Si multilayer.

silica interface of this sample is $\simeq 64°$. For larger angles of incidence than the critical angle the transmitted wave into the silica layer has a evanescent character and can couple to LRSPs on the a-Si films. Two dips of reflectance corresponding to the excitation of LRSPs are visible for wavelengths around 520 nm and angles 65.4° and 67.4°. The reflectance is less than 5% for both resonances revealing the excellent coupling of the incident plane wave with the two LRSPs. Note that $\lambda = 520$ nm corresponds to radiation with a larger energy than the band-gap of a-Si. For this wavelength the optical response of the bulk material is dominated by strong absorption, which is characterized by a complex permittivity with a large imaginary component, namely $\epsilon = 18.7 + i8.0$, and a high absorption coefficient $\alpha = 2.2 \times 10^7 \mathrm{m}^{-1}$. As it is shown below, the electric field is excluded from the thin absorbing layers as a result of the coupling of surface polaritons at their opposite sides. This is a common characteristic of long-range surface modes and explains the long propagation length and the concomitant narrow resonances in spite of the absorption.

7.3 Calculations and discussion

Figure 7.2(b) displays a calculation based on the transfer matrix formalism of the reflectance corresponding to the experiment [67]. We have used the refractive indices of silica and a-Si that were obtained from ellipsometry measurements. The thicknesses of the a-Si layers have been used as fitting parameters to the experiments. The values that we obtain for these thicknesses are 25 ± 0.5 nm for the upper a-Si layer and 21 ± 0.5 nm for the lower a-Si layer. These values of the thickness are in agreement with the nominal values set for growth and, within the image resolution, with the SEM photograph of Fig. 7.1(b).

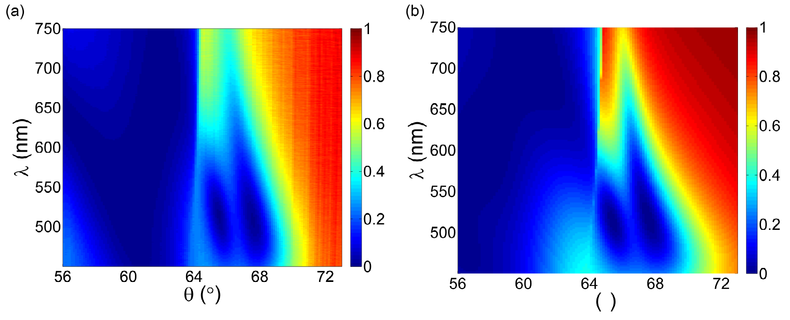

Figure 7.2: Measured (a) and calculated (b) reflectance of the a-Si multilayer structure of Fig. 7.1.

To better understand the origin of the two resonances observed in reflection, we have also calculated the electric field component along the a-Si layers, E_x, as a function of the vertical distance. The calculation has been done at a wavelength of 520 nm and for two angles of incidence corresponding to the two resonances observed in reflection. These angles are $\theta = 65.38°$ (Fig.7.3(a)) and $\theta = 67.42°$ (Fig.7.3(b)). We note that for both resonances E_x is antisymmetric with respect to the middle plane of the a-Si layers, vanishing inside the thin layers. This characteristic, which is common to long-range surface polaritons, leads to a reduction of the electromagnetic energy density in the absorbing thin layer and the concomitant long propagation distance of these modes [30].

We also observe in Figs. 7.3(a) and (b) a different symmetry of E_x with respect to the middle plane of the silica layer separating the two thin layers of a-Si. This difference in field symmetry can be also appreciated in Figs. 7.4, where E_x in the multilayer structure is represented in a color scale as a function of position in the x-z plane. While for the resonance at $\theta = 65.4°$ E_x is symmetric with respect to the middle plane of the silica layer, i.e., the field is in phase at the interfaces of the two a-Si layers in contact with the silica layer, for the resonance at $\theta = 67.4°$ the field is antisymmetric with respect to this plane , i.e., the field is π-dephased at these interfaces. This behavior is characteristic of hybridized modes that, as a result of their mutual coupling, lift their degeneracy and lead to a bonding and an antibonding state with opposite field symmetries [105].

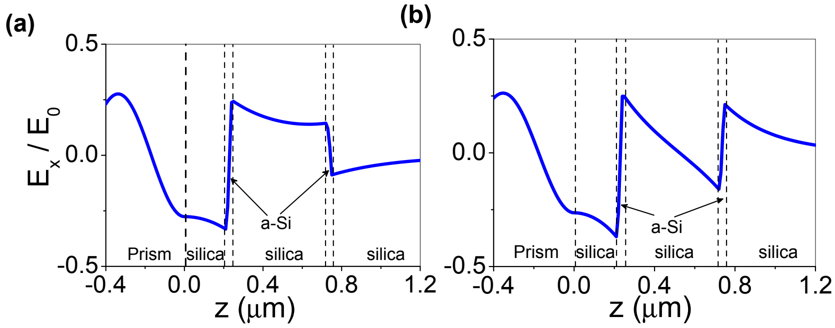

Figure 7.3: Electric field component along the x-direction as a function of the vertical direction of the a-Si multilayer displayed in Fig. 7.1 calculated for $\lambda = 520$ nm and an angle of incidence of (a) $\theta = 65.4°$ and (b) $\theta = 67.4°$.

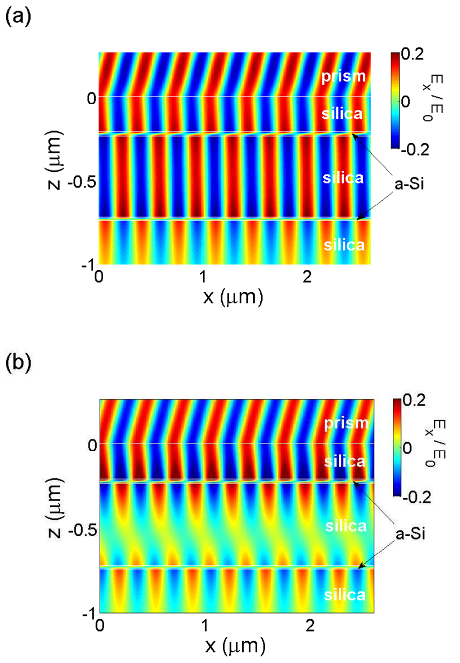

Figure 7.4: Color plot of the electric field component along the x-direction in the x-z plane direction of the a-Si multilayer displayed in Fig. 7.1 calculated for $\lambda = 520$ nm and an angle of incidence of (a) $\theta = 65.4°$ and (b) $\theta = 67.4°$.

7.4 Conclusions

In conclusion, we have demonstrated the excitation of coupled long -range surface polariton modes in multilayers of a-Si at visible frequencies. In spite of the strong absorption of a-Si at these frequencies, these surface polaritons exhibit narrow resonances that result from the exclusion of the electric field from the thin absorbing layers. Calculations of the field symmetries of the different resonances in the multilayer structure reveal the hybridization of the long-range surface polaritons. Multilayers of strongly absorbing dielectrics may find application as surface polariton resonance sensors operating at short wavelengths or to enhance light absorption in ultra-thin layers of semiconductors.

REFERENCES

[1] A. Einstein, *Nobel Prize presentation*, `http://nobelprize.org/nobel_prizes/physics/laureates/1921/`, 1921.

[2] C. F. Klingshirn, *Semiconductor Optics*, Springer, Advanced Text in Physics, 2005.

[3] J. Zenneck, *Über die Fortpflanzung ebener elektromagnetischer Wellen Mngs einer ebenen Leiterflache und ihre Beziehung zur drahtlosen Telegraphie*, Ann. der Physik **23**, 846 (1907).

[4] A. Sommerfeld, *Über die Ausbreitlung der Wellen in der drahtlosen Telegraphie*, Ann. der Physik **28**, 665 (1909).

[5] U. Fano, *Über die Ausbreitlung der Wellen in der drahtlosen Telegraphie*, J. Opt. Soc. Am. A **31**, 213 (1941).

[6] E. Economou, *Surface plasmons in thin films*, Phys. Rev. **182**, 539 (1969).

[7] D. L. Mills and E. Burstein, *Polaritons: the electromagnetic modes of media*, Rep. Prog. Phys. , 817 (1973).

[8] V. M. Agranovich and D. L. Mills, *Surface Polaritons*, North-Holland Publishing Company, Amsterdam New York Oxford, 1982.

[9] H. Raether, *Surface plasmons on smooth and rough surfaces and on gratings*, Springer-Verlag, Berlin Heidelberg, 1988.

[10] A. D. Boardman, *Electromagnetic Surface Modes*, Wiley, 1982.

[11] J. Le Gall, M. Olivier, and J.-J. Greffet, *Experimental and theoretical study of reflection and coherent thermal emissionby a SiC grating supporting a surface-phonon polariton*, Phys. Rev. B **55**, 10105 (1997).

[12] A. Huber, N. Ocelic, D. Kazantsev, and R. Hillenbrand, *Near-field imaging of mid-infrared surface phonon polariton propagation,* Appl. Phys. Lett. **87**, 081103 (2005).

[13] J. Huber, A. Ziegler, T. Kock, and R. Hillenbrand, *Infrared nanoscopy of strained semiconductors,* Nat Nano **4**, 153 (2009).

[14] D. Sarid, *Long-range surface-plasma waves on very thin metal films,* Phys. Rev. Lett. **47**, 1927 (1981).

[15] W. L. Barnes, W. Preist, S. C. Kitson, and J. R. Sambles, *Physical origin of photonic energy gaps in the propagation of surface plasmons on gratings,* Phys. Rev. B **54**, 6227 (1996).

[16] S. Bozhevolnyi, J. Erland, L. K., P. Skovgaard, and J. Hvam, *Waveguiding in surface plasmon polariton band gap structures,* Phys. Rev. Lett. **86**, 3008 (2001).

[17] W. L. Barnes, A. Dereux, and T. W. Ebbesen, *Surface plasmon subwavelength optics,* Nature **424**, 824 (2003).

[18] J. A. Dionne, L. A. Sweatlock, and H. A. Atwater, *Planar metal plasmon waveguides: frequency-dependent dispersion, propagation, localization, and loss beyond the free electron model,* Phys. Rev. B **72**, 075405 (2005).

[19] J. Homola, I. Koudela, and S. Yeea, *Surface plasmon resonance sensors: review,* Sen. Act. B **54**, 16 (1999).

[20] A. Zayats, I. Smolyaninov, and A. Maradudin, *Nano-optics of surface plasmon polaritons,* Phys. Rep. **408**, 131 (2005).

[21] E. Ozbay, *Plasmonics: Merging photonics and electronics at nanoscale dimensions,* Science **311**, 189 (2006).

[22] L. Novotny and B. Hecht, *Principles of nano-optics,* Cambridge University Press, Cambridge, 2006.

[23] S. Lal, S. Link, and N. J. Halas, *Nano-optics from sensing to waveguiding,* Nature Photon. **1**, 641 (2007).

[24] T. W. Ebbesen, C. Genet, and S. I. Bozhevolnyi, *Surface plasmon circuitry,* Phys. Today **61**, 44 (2008).

[25] A. Polman, *Plasmonics applied,* Science **322**, 868 (2008).

[26] A. Boltasseva, T. Nikolajsen, K. Leosson, K. Kjaer, M. S. Larsen, and I. Bozhevolnyi, S., *Integrated optical components utilizing long-range surface plasmon polaritons,* J. Lightwave Technol. **23**, 413 (2005).

[27] R. Charbonneau, N. Lahoud, G. Mattiussi, and P. Berini, *Demonstration of integrated optics elements based on long-ranging surface plasmon polaritons,* Opt. Express **13**, 977 (2005).

[28] V. N. Konopsky and E. V. Alieva, *Long-Range Propagation of Plasmon Polaritons in a Thin Metal Film on a One-Dimensional Photonic Crystal Surface,* Phys. Rev. Lett. **97**, 253904 (2006).

[29] P. Berini, *Figures of merit for 2D surface plasmon waveguides and application to metal stripes,* Opt. Express , 12174 (2007).

[30] V. Giannini, Y. Zhang, M. Forcales, and J. Rivas, *Long-range surface polaritons in ultra-thin films of silicon,* Opt. Express , 19674 (2008).

[31] G. Nenningera, P. TobisÏkab, J. Homolaa, and S. Yeea, *Long-range surface plasmons for high-resolution surface plasmon resonance sensors,* Sen. Act. B **74**, 145 (2001).

[32] K. A. Willets and R. P. Van Duyne, *Localized surface plasmon resonance spectroscopy and sensing,* Annu. Rev. Phys. Chem. **58**, 267 (2007).

[33] M. E. Stewart, C. R. Anderton, L. B. Thompson, J. Maria, S. K. Gray, J. A. Rogers, and R. G. Nuzzo, *Nanostructured plasmonic sensors,* Chem. Rev. **108**, 494 (2008).

[34] Y. Zhang, C. Arnold, and J. Rivas, *Long-range surface polaritons sensors based on nanmetric layers of strongly absorbing materials,* Submitted (2011).

[35] L. Tang, S. E. Kocabas, S. Latif, A. K. Okyay, D.-S. Ly-Gagnon, K. C. Saraswat, and D. A. B. Miller, *Nanometre-scale germanium photodetector enhanced by a near-infrared dipole antenna,* Nature Photon. **2**, 226 (2008).

[36] V. E. Ferry, L. A. Sweatlock, D. Pacifici, and H. A. Atwater, *Plasmonic nanostructure design for efficient light coupling into solar cells,* Nano Lett. **8**, 4391 (2008).

[37] I. De Leon and P. Berini, *Theory of surface plasmon-polariton amplification in planar structures incorporating dipolar gain media,* Phys. Rev. B **78**, 161401 (2008).

[38] I. De Leon and P. Berini, *Amplification of long-range surface plasmons by a dipolar gain medium,* Nat. Photon. **4**, 382 (2010).

[39] M. C. Gather, K. Meerholz, N. Danz, and K. Leosson, *Net optical gain in a plasmonic waveguide embedded in a fluorescent polymer,* Nat. Photon. **4**, 457 (2010).

[40] D. Leon and P. Berini, *Spontaneous emission in long-range surface plasmon-polariton amplifiers,* Phys. Rev. B **83**, 081414 (2011).

[41] R. Charbonneau, P. Berini, E. Berolo, and E. Lisicka-Shrzek, *Experimental observation of plasmon-polariton waves supported by a thin metal film of finite width,* Opt. Lett. **25**, 844 (2000).

[42] K. Leosson, T. Nikolajsen, A. Boltasseva, and S. Bozhevolnyi, *Long-range surface plasmon polariton nanowire waveguides for device applications,* Opt. Express **14**, 314 (2006).

[43] P. Berini, *Long-range surface plasmon polaritons,* Adv. Opt. Photon. **1**, 484 (2009).

[44] K. Matsubara, S. Kawata, and S. Minami, *Multilayer system for a high-precision surface plasmon resonance sensor,* Opt. Lett. **15**, 75 (1990).

[45] J. Dostálek, A. Kasry, and W. Knoll, *Long Range Surface Plasmons for Observation of Biomolecular Binding Events at Metallic Surfaces,* Plasmonics **2**, 97 (2007).

[46] P. Berini, *Plasmon-polariton waves guided by thin lossy metal films of finite width: Bound modes of symmetric structures,* Phys. Rev. B **61**, 10484 (2000).

[47] S. Bozhevolnyi, V. Volkov, E. Devaux, and T. Ebbesen, *Channel plasmon-polariton guiding by subwavelength metal grooves,* Phys. Rev. Lett. **95**, 046802 (2005).

[48] J. Burke, G. Stegeman, and T. Tamir, *Surface-polariton-like waves guided by thin, lossy metal films,* Phys. Rev. B **33**, 5186 (1986).

[49] R. Zia, M. D. Selker, and M. L. Brongersma, *Leaky and bound modes of surface plasmon waveguides,* Phys. Rev. B **71**, 165431 (2005).

[50] P. Berini, *Figures of merit for surface plasmon waveguides,* Opt. Express , 13030 (2006).

[51] R. Zia, M. D. Selker, P. B. Catrysse, and M. L. Brongersma, *Geometries and materials for subwavelength surface plasmon modes,* J. Opt. Soc. Am. A **21**, 2442 (2004).

[52] P. R. West, S. Ishii, G. V. Naik, N. K. Emani, V. M. Shalaev, and A. Boltasseva, *Searching for better plasmonic materials,* Laser and Photon. Rev. , 1 (2010).

[53] J. Lagois and B. Fischer, *Dispersion theory of surface-exciton polaritons,* Phys. Rev. B **17**, 3814 (1978).

[54] J. C. Quail, J. G. Rako, and H. J. Simon, *Long-range surface-plasmon modes in silver and aluminum films,* Opt. Lett. **8**, 377 (1983).

[55] F. Yang, , S. J. R., and G. W. Bradberry, *Long-Range Coupled Surface Exciton Polaritons,* Phys. Rev. Lett. **64**, 559 (1990).

[56] F. Yang, , S. J. R., and G. W. Bradberry, *Long range surface modessupported by thin film,* Phys. Rev. B **44**, 5855 (1991).

[57] G. J. Kovacs, *Surface polariton in the ATR angular spectra of a thin iron film bounded by dielectric layers,* J. Opt. Soc. Am **68**, 1325 (1978).

[58] F. Yang, G. W. Bradberry, and S. J. R., *Experimental observation of surface excitation-polaritons on vanadium using infrared radiation,* J. Mod. Phys. **37**, 1545 (1990).

[59] R. Crook, F. Yang, and J. R. Sambles, *Long-range optical modes supported by a strongly absorbing thin organic film,* J. Opt. Soc. Am. B **10**, 237 (1993).

[60] E. Wood, J. Sambles, F. Pudonin, and V. Yakovlev, *Degenerate long range surface modes, supported on thin nickel films,* Opt. Commun. **132**, 212 (1996).

[61] F. Yang, , G. W. Bradberry, and S. J. R., *Long range surface modes supported by very thin silver films,* Phys. Rev. Lett. **66**, 2030 (1991).

[62] M. Takabayashi, M. Haraguchi, and M. Fukui, *Propagation length of guided waves in lossy Si film sandwiched by identical dielectrics,* J. Opt. Soc. Am. B **12**, 2406 (1995).

[63] M. W. Chu, C. H. Chen, F. J. García de Abajo, J. P. Deng, and C. Y. Mou, *Surface exciton polaritons in individual Au nanoparticles in the far-ultraviolet spectral regime,* Phys. Rev. B **77**, 245402 (2008).

[64] C. Arnold, Y. Zhang, and J. Rivas, *Long-range surface polaritons supported by lossy thin films,* Appl. Phys. Lett. **96**, 113108 (2010).

[65] P. B. Johnson and R. W. Christy, *Optical constants of the noble metals,* Phys. Rev. B **6**, 4370 (1972).

[66] J. Dionne, *Flatland photonics: Circumventing diffraction with planar plasmonic architectures,* PhD thesis, California institute of technology, 2009.

[67] P. Yeh, *Optical waves in layered media,* John Wiley and Sons, New York, Chichester, Brisbane, Toronto, Singapore, 1988.

[68] R. Zia, A. Chandran, and M. L. Brongersma, *Dielectric waveguide model for guided surface polaritons,* Opt. Lett. **30**, 1473 (2005).

[69] R. D. Kekatpure, A. C. Hryciw, E. S. Barnard, and M. L. Brongersma, *Solving dielectric and plasmonic waveguide dispersion relations on a pocket calculator,* Opt. Express **17**, 24112 (2009).

[70] R. Syms and J. Cozens, *Optical guided waves and devices,* McGraw-Hill, 1992.

[71] K. Okamoto, *Foundamentals of optical waveguides,* Katsunari Okamoto, 2006.

[72] V. V. Shevchenko, *Continuous transitions in open waveguides,* Golem Press, Boulder, Colorado, 1971.

[73] Q. Bao, H. Zhang, B. Wang, Z. Ni, C. Lim, Y. Wang, D. Tang, and K. Loh, *Broadband graphene polarizer,* Nat. Photon. **5**, 411 (2011).

[74] W. L. Barnes, *Surface plasmon-polariton length scales: a route to sub-wavelength optics,* J. Opt. A: Pure Appl. Opt. **8**, S87 (2006).

[75] L. Smith, M. C. Taylor, I. R. Hooper, and W. L. Barnes, *Field profiles of coupled surface plasmon-polaritons,* J. Mod. Opt. **55**, 2929 (2008).

[76] S. Bozhevolnyi and S. T., *General properties of slow-plasmon resonant nanostructures: nano-antennas and resonators,* Opt. Express **15**, 10869 (2007).

[77] S. Herminghaus, M. Klopfleisch, and H. J. Schmidtand, *Attenuated total reflectance as a quantum interference phenomenon,* Opt. Lett. **19**, 4 (1994).

[78] Y. D. Chong, L. Ge, H. Cao, and A. D. Stone, *Coherent Perfect Absorbers Time-Reversed Lasers*, Phys. Rev. Lett. **105**, 053901 (2010).

[79] S. Raous and M. Wuttig, *Phase change materials, science and applications*, Springer, Berlin Heidelberg, 2008.

[80] A. Pirovano, A. Lacaita, F. Pellizzer, S. Kostylev, A. Benvenuti, and R. Bez, *Low-Field Amorphous State Resistance and Threshold Voltage Drift in Chalcogenide Materials*, IEEE Trans. Electron Devices **51**, 714 (2004).

[81] H. K. Pulker, *Coatings on glass*, Elsevier, Amsterdam, 1984.

[82] K. Shportko, S. Kremers, M. Woda, D. Lencer, J. Robertson, and M. Wuttig, *Resonant bonding in crystalline phase change materials*, Nature Mater. **7**, 653 (2008).

[83] G. healthcare, *Label free plasmonic sensors*, `http://www.biacore.com/lifesciences/index.html`, 2011.

[84] E. Palik, editor, *Handbook of optical constants of solids*, Academic Press, Inc., New York, New York, 1985.

[85] B. E. Saleh and M. Teich, *Foudamentals of Photonics*, Wiley, Hoboken, NJ, 2007.

[86] A. Reisinger, *Characteristics of optical guided modes in lossy waveguides*, Appl. Opt. **12**, 1015 (1973).

[87] S. J. Albader and M. Imtaar, *TM polarized surface plasma modes on metal coated dielectric cylinders*, IEEE J. Quantum Electronics **28**, 865 (1992).

[88] S. J. Albader and M. Imtaar, *Azimuthally uniform suface plasma modes in thin metallic cylindrical shells*, IEEE J. Quantum Electronics **28**, 525 (1992).

[89] S. J. Albader and M. Imtaar, *Optical fiber hybrid-surface plasmon polaritons*, J. Opt. Soc. Am. B **10**, 83 (1993).

[90] J. A. Dionne, L. A. Sweatlock, H. A. Atwater, and A. Polman, *Plasmon slot waveguides: Towards chip-scale propagation with subwavelength-scale localization*, Phys. Rev. B **73**, 035407 (2006).

[91] J. Homola, *Surface plasmons resonanse based sensors*, Springer, Berlin Heidelberg, 2006.

[92] J. Anker, W. Paige Hall, O. Lyandres, N. Shah, J. Zhao, and V. Van Duyne, *Biosensing with plasmonic nanosensors,* Nature Mater. **7**, 442 (2008).

[93] X. Fan, I. M. White, S. I. Shopova, H. Zhu, J. D. Suter, and Y. Sun, *Sensitive optical biosensors for unlabeled targets: A review,* Anal. Chim. Acta , 620 (2008).

[94] A. Kasry and W. Knoll, *Long range surface plasmon fluorescence spectroscopy,* Appl. Phys. Lett. **89**, 101106 (2006).

[95] A. G. Brolo, R. Gordon, B. Leathem, and K. L. Kavanagh, *Surface plasmon sensor based on the enhanced light transmission through arrays of nanoholes in gold films,* Langmuir **20**, 4813 (2004).

[96] J. Hu, V. Tarasov, A. Agarwal, L. Kimerling, N. Carlie, L. Petit, and K. Richardson, *Fabrication and testing of planar chalcogenide waveguide integrated microfluidic sensor,* Opt. Express , 2307 (2007).

[97] K. Maex, M. Baklanov, D. Shamiryan, F. Iacopi, S. Brongersma, and Z. Yanovitskaya, *Low dielectric constant materials for microelectronics,* J. Appl. Phys. **93**, 8793 (2003).

[98] A. Kruis, *Die Äquivalentdisperision von starken Elektrolyten in Lösung,* Z. Phys. Chem. B **34**, 13 (1936).

[99] J. Gent, P. V. Lambeck, H. J. M. Kreuwel, G. J. Gerritsma, E. J. R. Sudholter, D. N. Reinhoudt, and T. J. A. Popma, *Optimization of a chemooptical surface plasmon resonance based sensor,* Appl. Opt. **29**, 2843 (1990).

[100] L. J. Sherry, S.-H. Chang, G. C. Schatz, and R. P. Van Duyne, *Localized Surface Plasmon Resonance Spectroscopy of Single Silver Nanocubes,* Nano Lett. **5**, 2034 (2005).

[101] R. Jha and A. Sharma, *High-performance sensor based on surface plasmon resonance with chalcogenide prism and aluminum for detection in infrared,* Opt. Lett. **34**, 6 (2009).

[102] M. Svedendahl, S. Chen, A. Dmitriev, and M. Käll, *Refractometric sensing using propagating versus localized surface plasmons: a direct comparison,* Nano Lett. **9**, 4428 (2009).

[103] S. Ahl, P. J. Cameron, J. Liu, W. Knoll, J. Erlebacher, and F. Yu, *A Comparative Plasmonic Study of Nanoporous and Evaporated Gold Films,* Plasmonics **3**, 13 (2008).

[104] G. STEGEMAN and J. BURKE, *Long-range surface plasmons in electrode structures,* Appl. Phys. Lett. **43**, 221 (1983).

[105] H. Won, K. Kim, S. Song, C. Oh, P. Kim, S. Park, and S. Kim, *Vertical coupling of long-range surface plasmon polaritons,* Appl. Phys. Lett. **88** (2006).

[106] D. Woolf, M. Loncar, and F. Capasso, *The forces from coupled surface plasmon polaritons in planar waveguides,* Opt. Express , 19996 (2009).

[107] T. Srivastava and A. Kumar, *Comparative study of directional couplers utilizing long-range surface plasmon polaritons,* Appl. Opt. **49**, 2397 (2010).

[108] F. Liu, Y. Li, R. Wan, Y. Huang, X. Feng, and W. Zhang, *Hybrid coupling between long-range surface plasmon polariton mode and dielectric waveguide mode,* J. Lightwave Technol. **29**, 1265 (2011).

SUMMARY

Long-range surface polaritons in thin layers of absorbing materials

Long-range surface polaritons (LRSPs) are electromagnetic surface modes confined at the interfaces of an thin film surrounded by a homogeneous dielectric. These modes are generally characterized by the subwavelength confinement and the long propagation length. In case of a metallic thin film, the mode is named long-range surface plasmon polaritons (LRSPPs). Because of the special optical properties mentioned above, LRSPPs have appeared in a large number of studies both fundamental and applied, including modal studies, prism experiments, field enhancement, biosensors etc.. However, much less attention has been devoted to LRSPs on strongly absorbing dielectrics.

In this thesis, we present a fundamental study of the optical properties of LRSPs supported by thin layers of strongly absorbing materials. First, a detailed theoretical formulation of surface modes in arbitrary thin layers is given in chapter 2. The differences between LRSPPs, LRSPs and TM_0 mode are discussed further in terms of dispersion relations and electromagnetic field profiles for the case of arbitrary thin layers and in real materials, i.e., silver and amorphous silicon. Depending on the permittivities of the thin layers, guided modes can be supported either on metal or absorbing dielectrics. The rare existing condition of LRSPs is $|\epsilon_{2r}| \lesssim \epsilon_{2i}$ (independent of the sign of ϵ_{2r}) and $\epsilon_{2i} \gg 1$. We also discuss the dispersion relation of LRSPs in the thin film approximation in which we use this expression in chapter 3 and chapter 6.

To investigate the dependence of surface modes supported by lossy thin films to their permittivity, we show in chapter 3 that a 20 nm thin film made of chalcogenide $\mathrm{Ge}_{17}\mathrm{Sb}_{76}\mathrm{Te}_7$ glass can support LRSPs in the visible. This chalcogenide glass

has two phases based on the different heating temperature, i.e., an amorphous and a crystalline phase. By changing the phase of this material, the real components of permittivity change the sign while the imaginary components remains large. From the dispersion relation of LRSPs on both crystalline and amorphous layers obtained from the experiment and mode calculation, we demonstrate the relative insensitivity of LRSPs to the real component of the permittivity of the thin films.

In chapter 4, we illustrate the excitation of long-range surface polaritons LRSPs in ultra-thin films of amorphous silicon (a-Si) at visible and UV frequencies. As a comparison, we calculate the propagation length and confinement length of LRSPPs and LRSPs. The figure of merit of waveguides in UV and visible is given, we conclude that the LRSPs have similar characteristics to LRSPPs on gold although LRSPs are guided by thin layers of strongly absorbing materials. Excitation of long-range surface modes in absorbing Si opens the possibility to surface polariton optics compatible with standard Si processing technology.

In chapter 5, we determine the dispersion of long-range guided modes in thin layers of a-Si by attenuated total internal reflectance measurements in layers with different thickness. The dispersion relation of guided modes on a-Si move away from the light cone when the thickness of the a-Si layer increases ($d > 10$ nm). The corresponding propagation length and confinement length are also modified by controlling the dispersion relation. An evolution between LRSPs and TM_0 mode is also found when a-Si layer thickness increase from 13 to 23 nm.

In chapter 6, we show that strong optical absorption in materials can be beneficial to improve the sensitivity of surface polariton sensors. In particular, we experimentally prove that LRSPs supported by nanometric films of strongly absorbing chalcogenide glasses can be used as sensitive probes to changes in the refractive index of the surrounding medium. We also calculate the sensing figure of merit for different types of long-range surface modes on different materials. In the thin film approximation, an analytical expression of sensing figure of merit is given for LRSPs. This result provide alternative solutions for optical sensing that are CMOS compatible rather than noble metals as the sensing substrate.

In Chapter 7, we demonstrate experimentally the excitation of coupled long-range surface polariton modes in multilayers of a-Si at visible frequencies. These different surface polaritons exhibit narrow resonances that result from the exclusion of the electric field from the thin absorbing layers. We model this reflectance measurement and the corresponding electric filed profile by using the transfer matrix method. Calculations of the electromagnetic field symmetries of the different resonances in the multilayer structure reveal the coupling between different LRSPs. Multilayers of strongly absorbing dielectrics may find application as surface polariton resonance sensors operating at short wavelengths or to enhance light absorption in ultra-thin layers of semiconductors.

SAMENVATTING

Lange-afstand oppervlakte polaritonen (LRSPs) zijn elektromagnetische oppervlakte modi geconcentreerd op de grensvlakken van een dunne film, omringd door een homogeen diëlektricum. Deze modi worden over het algemeen gekenmerkt door een opsluiting kleiner dan de golflengte en een grote voortplantings lengte. In het geval van een metalen dunne film worden de modi lange afstand oppervlakte plasmon polaritonen (LRSPPs) genoemd. Door de speciale optische eigenschappen hierboven vermeld zijn LRSPPs verschenen in een groot aantal studies, zowel fundamenteel als toegepast waaronder studies naar de modi, prisma experimenten, veldversterking, biosensoren etc.. Er is echter veel minder aandacht besteed aan LRSPs op sterk absorberende diëlektrica.

In dit proefschrift presenteren we een fundamentele studie naar de optische eigenschappen van LRSPs ondersteund door dunne lagen van sterk absorberende materialen. Er wordt een gedetailleerde theoretische formulering van oppervlakte modi in algemene dunne lagen gegeven in hoofdstuk 2. De verschillen tussen LRSPPs, LRSPs en TM_0 worden verder besproken in termen van dispersie relaties en de profielen van het elektromagnetische veld, voor algemene dunne lagen en in echte materialen zoals zilver en amorf silicium. Afhankelijk van de permittiviteit van de dunne laag kunnen geleide modi worden ondersteund, hetzij op metaal of absorberende diëlektrica. De speciale voorwaarde voor LRSPs is $|\epsilon_{2r}| \lesssim \epsilon_{2i}$ (onafhankelijk van het teken van ϵ_{2r}) en $\epsilon_{2i} \gg 1$. Ook bespreken we de dispersie relatie van LRSPs in de dunne film benadering, die we gebruiken in hoofdstuk 3 en hoofdstuk 6.

De afhankelijkheid van de permittiviteit van oppervlakte modi ondersteund door absorberende dunne films onderzoeken we in hoofdstuk 3. We laten zien dat een 20 nm dunne film gemaakt van chalcogenide $\mathrm{Ge}_{17}\mathrm{Sb}_{76}\mathrm{Te}_7$ materiaal LRSPs kan ondersteunen in het zichtbare spectrum. Dit chalcogenide glas bestaat uit twee fasen, een amorfe en een kristallijne, afhankelijk van de verhittingstemperatuur. Door de fasen van dit materiaal te veranderen verandert de reële component van de permittiviteit van teken, terwijl de imaginaire component groot blijft. Met behulp van de dispersie relatie van LRSPs op zowel kristallijne als amorfe lagen verkregen uit het experiment en de modus berekening tonen we de relatieve ongevoeligheid van LRSPs aan voor de reële component van de permittiviteit van de dunne film.

In hoofdstuk 4 illustreren we de excitatie van de lange afstand oppervlakte polaritonen LRSPs in ultra-dunne films van amorf silicium (a-Si) voor zichtbare en UV frequenties. Ter vergelijking berekenen we de voortplantings lengte en duur van de opsluiting LRSPPs en LRSPs. Het prestatiegetal van de golfgeleiders in UV en zichtbaar wordt gegeven. We concluderen dat de LRSPs vergelijkbare kenmerken als de LRSPPs op goud hebben, hoewel LRSPs worden geleid door dunne lagen van sterk absorberende materialen. Excitatie van lange afstands oppervlakte modi in absorberend Si opent de mogelijkheid voor oppervlakte polariton optica die verenigbaar is met standaard Si processing technologie.

In hoofdstuk 5 bepalen we de dispersie van de lange afstand geleide modi in dunne lagen van a-Si door verzwakte totale interne reflectie metingen in lagen met verschillende dikte. De dispersie relatie van geleide modi op de a-Si wijkt af van de lichtkegel wanneer de dikte van de a-Si laag toeneemt ($d > 10\,\text{nm}$). De bijbehorende voortplanting en opsluitings lengte zijn ook afhankelijk van de dispersie relatie. Een overgang tussen LRSPs en TM_0 modi is ook gevonden wanneer de a-Si laagdikte toeneemt van 13 tot 23 nm.

In hoofdstuk 6 laten we zien dat een sterke optische absorptie in materialen gunstig kan zijn om de gevoeligheid van de oppervlakte polariton sensoren te verbeteren. In het bijzonder hebben we experimenteel aangetoond dat lange-afstand oppervlakte polaritonen ondersteund door nanometrische films van sterk absorberend chalcogenide glas kunnen worden gebruikt als probe die gevoelig is voor veranderingen in de brekingsindex van het omringende medium. Ook hebben we het sensing prestatiegetal berekend voor verschillende types van lange-afstands oppervlakte modi in verschillende materialen. In de dunne film benadering is een analytische uitdrukking voor het sensing prestatiegetal gegeven voor lange afstand oppervlakte polaritonen. Deze resultaten bieden alternatieve oplossingen voor optische detectie die CMOS-verenigbaar zijn in plaats van edelmetalen voor het sensing substraat.

In hoofdstuk 7 tonen we experimenteel de excitatie aan van gekoppelde lange-afstands oppervlakte polariton modi in meerlagige a-Si bij zichtbare frequenties. Deze verschillende oppervlakte-polaritonen vertonen smalle resonanties die voortvloeien uit de uitsluiting van het elektrische veld in de dunne absorberende lagen. We modelleren deze reflectie meting en het profiel van het bijbehorende elektrische veld met de transfer matrix methode. Berekeningen van de elektromagnetische veld symmetrieën van de verschillende resonanties in de meerlagige structuur onthullen de koppeling tussen verschillende lange afstands oppervlakte polaritonen. Multilagen van sterk absorberende diektrica kunnen toepassing vinden als oppervlakte polariton resonantie sensors werkend bij korte golflengtes, of om de absorptie van licht in ultra-dunne lagen van halfgeleiders te verbeteren.

NOTATION

A, C	incident amplitude
A	absorbance
B, D	reflected amplitude
c_j	speed of light in medium j
c_0	speed of light in vacuum
d	thin film thickness of slab waveguide
$\mathbf{E}$	electric field
F	transmitted amplitude
FOM	figure of merit of waveguide
FOM	figure of merit of surface polariton sensors
$FWHM$	half of the maximum of resonance
$\mathbf{H}$	magnetic field
IS	intrinsic sensitivity
$\mathbf{k}_0$	wavenumber in vacuum
k	wavenumber
k_r	real component of wavenumber
k_i	imaginary component of wavenumber
κ	ik
$\mathrm{L_x}$	propagation length
$\mathrm{L_y}$	confinement length or decay length
n_j	refractive index in medium j
n_d	refractive index in the surrounding medium
R	reflectance
$\mathbf{R}$	reflection
r	reflection coefficient for p-polarization

$\mathrm{R_q}$	surface roughness
T	transmittance
t	time
t	transmission coefficient for p-polarization
u	electromagnetic energy density inside of slab waveguide
v_g	group velocity
α	absorption coefficient
$\Delta\theta$	half of the maximum of resonance or resonance width
δn	refractive index difference
δk_r	wavenumber difference
$\delta\theta$	resonance shift
ϵ_0	permittivity in vacuum
ϵ_j	permittivity in medium j
ϵ_jr	real component of permittivity in medium j
ϵ_ji	imaginary component of permittivity in medium j
λ	wavelength in vacuum
θ	angle of incidence
θ_c	critical angle
ω	angular frequency

ACKNOWLEDGMENTS

In about finishing this thesis, although it takes some time but I know I am not working alone. There are many people whom I enjoyed working with during the last four years. Hereby, I would like to give my faithful thanks to them.

First I want to thank my promotor, Jaime, who provide me the opportunity to work on this topic, long-range surface polaritons, in his group. Jaime, thanks a lot! I appreciate all your contributions of time, ideas, your hospitality when I arrived in the Netherlands, the motivation during the hard time, the critical view on my experiment data and presentations. You taught me, in consciously and unconsciously, how good optical experiment is done. It was great working together with you and sharing an office for the last two years. I appreciate your honest and I am very grateful for all the "hard" discussions we had.

I would like also to thank all the members of the Surface Photonics group. Manuel, your knowledge on guided modes and absorbing materials helped me a lot when we start this project on LRSPs. It was nice that working with you on confocal microscope, I have learned a lot from you. Silke, it was nice time sharing an office with you. You are always helpful when there is a question, thanks for that. Gabriele, thanks for all the useful discussions. I have learned a lot from you on handling optical equipments. Vincenzo, it was a pleasure to work together with you on LRSPs. You were always open for discussing theoretical questions. Christophe, thank you for all the nice discussions, motivations and advises in the lab. It was short but really nice time to work with you on the same topic. Martijn, as you are the only Dutch member in our group, thanks a lot for helping me to correct my summary in Dutch. Grzegorz, thanks a lot for all the fun in the lab and ideas of my cover. Giuseppe, it is good to know that you will continue to work on guided modes on thin films. Thank you for all the nice discussions and good luck with your research. Gabriel, thanks for reading and correcting this thesis. I also like to thank all the members of the Surface Photonics group from AMOLF.

Otto, Bram, Audrey, Ruud, Said, Rogelio, Olaf and Shunsuke thank you all for the lunches, coffee breaks, beers, and football matches we had together.

This work was performed at Philips Research. I like to thank all the members of the Photonic Materials and Devices group. Within this group, especially members of the cluster. Ruud, Marc, Genia, Eduard, Dick, Coen, thank you all for sharing information about your Philips projects and for the discussions during the cluster meetings. Coen, your knowledge on phase change materials inspire us to study optical guided modes on this material. Marc, thanks a lot for your input of materials background and also all the helps in the clean room. Yongfeng, thanks for your advises in career searching. Patrick, thank a lot for lending us your spectrometer. Hans, thanks a lot for sharing the information of phosphors with us. Ties, your spinning machine saves a lot of time for us, thank you and good luck for your career. Gert't, thanks for all the nice discussions on sensors and reading my thesis carefully. Eugene, thanks a lot for allowing us using your lab and helping us to improve safety in the labs. Shu, thanks a lot for helping me with the notations. Most of my samples were fabricated at MiPlaza, philips research. Thanks to all the MiPlaza employees for nano fabrications and lab support. Jan, Eddy, thanks for the accurate thin film deposition of silicon and phase change materials. Hetty, Monique, thanks for all SEM images. Jeroen, thanks a lot for the deposition of SiO_2 and SiOH. Toon, thank you for all the guidance on ellipsometry. Albert, thank you for all the Labview programming. Ad, thanks for all the well coordinating with Leica support.

Our group is part of center for nanophotonics at AMOLF. Many thanks go to all past and present members of the Center for Nanophotonics. I enjoyed the poster sessions and colloquias. I learned a lot from all these training to be able to treat science critically. Alert and Kobus, thanks a lot for all the advises during my presentations. Ramy, EJ, it was a pleasure sharing an office together with you. Also, EJ, it was nice time when you measured PL and lifetime at philips. Martin, thanks for helping me with cathodoluminescence measurements. Rob, thanks for showing me your confocal microscope at AMOLF. During the preparation for defending this thesis, I appreciate many helps from the PSN group. Margriet, thanks a lot for helping me with all the forms and necessary informations. Rob, thanks for reading my thesis and all the suggestions.

Thanks.
Yichen

CURRICULUM VITAE

Yichen Zhang was born on August 17, 1982 in Beijing, P.R. China. He studied materials physics at Beijing union university. Before he obtained his bachelor degree in 2004, he performed a small research project on x-ray diffraction spectroscopy on assembled metallic particles. He went to Sweden to continue his study of physics and he finished his Master's degree in 2006 with a project entitled optical properties of plasmonic metal-dielectric nano-sandwiches, which is performed in the chemical physics group/Bio-photonic group at Chalmers University of Technology, Sweden supervised by prof. Bengt Kasemo. In March 2007 he started his PhD research in the group of Nanowire Photonics/Surface Photonics under supervision of prof. Jaime Gómez Rivas. The group is based on an industrial partnership program between AMOLF and Philips. The results of that work are described in this thesis. In his free time, he likes trekking in the mountain area.

LIST OF PUBLICATIONS

This thesis is based on the following publications:

- *Long-range surface polaritons in ultra-thin films of silicon*, V. Giannini, Y. Zhang, M. Forcales, and Jaime Gómez Rivas, Opt. Express **16**, 19674 (2008). **(Chapter 4)**
- *Long Range Surface Polaritons supported by lossy thin films*, C. Arnold, Y. Zhang, and Jaime Gómez Rivas, Appl. Phys. Lett. **96**, 2925 (2010). **(Chapter 3)**
- *Surface polariton sensors based on nanometric layers of strongly absorbing materials*, Y. Zhang, C. Arnold, P. Offermans and Jaime Gómez Rivas, Submitted. **(Chapter 6)**
- *Controlling the dispersion relation of guided modes in thin layers of amorphous silicon*, Y. Zhang, C. Arnold and Jaime Gómez Rivas, in preparation. **(Chapter 5)**
- *Coupled long-range surface polaritons in multilayers of silicon*, C. Arnold, Y. Zhang and Jaime Gómez Rivas, Submitted. **(Chapter 7)**

Other publications by the author:

- *Spontaneous emission of long-range surface polaritons supported by highly lossy thin films*, C. Arnold, Y. Zhang, and Jaime Gómez Rivas, in preparation.
- *Long-range surface plasmon polaritons at THz frequencies in thin semiconductor layers*, Y. Zhang, Audrey Berrier and Jaime Gómez Rivas, Submitted.

- *Universal Scaling of the Figure of Merit of Plasmonic Sensors*, Peter Offermans, Martijn C. Schaafsma, Said R. K. Rodriguez, Yichen Zhang, Mercedes Crego-Calama, Sywert H. Brongersma, and Jaime Gómez Rivas, ACS nano(2011).